

JMM



ÉCOLE POLYTECHNIQUE
FÉDÉRALE DE LAUSANNE

Diploma Thesis

Adriano Manini

Localisation of ECH Power Deposition through the Dynamic Response of the Plasma of TCV

This diploma work was carried out at

**Centre de Recherches en Physique des Plasmas
Association Euratom - Confédération Suisse
Ecole Polytechnique Fédérale de Lausanne
CH-1015 Lausanne, Switzerland**

Lausanne, 5. May - 5. September 1997

Supervisors

Prof. J. Lang

**Prof M.Q. Tran
Dr. J.M. Moret**

Ecole Polytechnique Fédérale
Centre de Recherches en Physique des Plasmas
CH-1015 Lausanne, Switzerland
1997

Acknowledgements

First and foremost, I would like to thank Jean-Marc Moret, whose constant help was invaluable in carrying out this diploma work: thank you very much, Jean-Marc, for your patience and for the time you spent answering my numerous questions. The work was a great source of interest for me and the help you gave me constantly supported my efforts.

Furthermore, I would like to thank Prof. J. Lang, Prof. M.Q. Tran and Prof. F. Troyon for having given me the opportunity to finish my studies in a subject which has always been of big interest to me.

Particular thanks go to Dr. J. Lister, whose great help, not only in the writing of this report, but also in making my first months here in Lausanne a lot easier.

Another big thank you goes to S. Alberti, who constantly demonstrated much interest in the work I was carrying out and for the many productive discussions we had.

Finally, a big thank you to all the people of the TCV team, who, once in a while, had to have a lot of patience for the questions I asked them.

E dopo i riconoscimenti di rito, tengo molto a ringraziare alcune persone che mi sono sempre state vicine, nei momenti dove tutto procedeva bene come pure nei momenti di difficoltà.

Primissimi nella lista, naturalmente, i miei genitori. Grazie "Mami" e "Pappi" per tutto quello che avete fatto per me in questi anni! Lo so che é stata dura anche per voi, soprattutto durante i miei esami e durante questi ultimi quattro mesi (per non parlare della pazienza che avete dovuto trovare per sopportarmi in certi momenti), e una buona fetta del lavoro che ho svolto é sicuramente merito vostro!!!

Un grossissimo grazie di tutto cuore anche a te, Ramona! Durante questo mio ultimo anno di studi, sei riuscita a darmi quel qualcosa in piú che unicamente una persona veramente speciale é in grado di trasmettere, e non c'è sicuramente bisogno che ti dica qui quanto speciale tu sia, vero? Ramona ... pio-grazie!!!

Un immenso ringraziamento non può non andare pure a te, Marco! Tentare di ricordare quanto passato insieme in questi cinque anni sarebbe impresa folle, impresa per la quale non mi sento all'altezza, ma tu sai, ed é unicamente questa la cosa importante!

Un altro grandissimo grazie a te, Michèle, non solo per le correzioni della primissima versione di questo rapporto, ma soprattutto per la tua pura e semplice, vera, amicizia.

Infine, ma non per questo meno importanti, un grazie a tutti i miei amici che, anche vedendomi molto poco a causa dei miei impegni fuori cantone, sono sempre stati pronti ad accogliermi a braccia aperte quando tornavo a casa.

Per tutte le persone che non ho citato direttamente o che ho dimenticato, vi chiedo scusa sin da ora, non era mia intenzione tralasciare nessuno, ma voi sapete la testa che ho ogni tanto!

Grazie a tutti!!!

Abstract

The aim of the research that was carried out is to determine the localization of the ECH (Electron Cyclotron Heating) power deposition profile through the dynamic response of the plasma of the tokamak TCV (Tokamak à Configuration Variable). The experimental determination of the ECH power deposition profile constitutes an essential task for the study of the properties of the heated plasma. Particularly, it allows the use of power modulation techniques to extract heat diffusivity and heat convection coefficients from the analysis of the perturbed temperature profiles.

The dynamic response of the plasma parameters has already been used in other devices. This approach has the advantage of being able to separate, with a good approximation, the heating mechanisms themselves from the reaction of the plasma. Many different formalisms, as well as the corresponding numerical methods already exist, each of them with its strong and weak points. Particular importance will be given to the study of the limits of applicability of each of the methods chosen in order to quantify the quality of the results that each of them will extract.

*ce n'est pas un abstract mais une
traduction du sujet. Abstract = motivation
+ découvertes et résultats importants*

Outline

The report is organized as follows.

Chapter I gives a general introduction to nuclear fusion via magnetic confinement, in particular the tokamak approach.

Chapter II presents an overview of the experimental facilities available at the CRPP.

Chapter III presents a preliminary study of the problem and, in particular, the solving of the transport equation which provides a useful tool for the temperature profile determination starting from a chosen set of parameters containing the deposition coordinates, the injected power and diffusion and convection parameters.

Chapter IV provides a formalization of the problem studied, giving a useful tool (the J2 matrix) for the comprehension of the results that will follow. In particular, it is the J2 matrix itself that will show the independence of the set of parameters chosen for the further treatment of the problem. *don*

Chapter V presents a deeper analysis of the treated temperature profiles. Particularly important is the result of different sets of parameters leading (within resolution capabilities) to the same stationary temperature profile. As a consequence of this fact, there is an increase of importance of the early stages of the temperature profile evolution for the purpose of power deposition localization. The independence of the variations of the profiles with respect to the chosen deposition coordinates and with respect to different ratios between the parameters of diffusion and convection is then explicitly shown. *not defined*

Chapter VI treats the transport problem in the presence of a modulated source, and it particularly investigates the quality of the parameters separation with respect to the chosen modulation. The investigation shows that it is possible to find an optimized modulation which leads to a better separation of the profiles, leading then to a better localization. *se refere a des ratios "impliquées" pour une autre ?*

Chapter VII introduces the reconstruction procedure for the parameters studied and demonstrates, for the actual inverse problem, the results of chapter VI.

Chapter VIII treats the localization of a real experiment, TCV shot # 12508, confronting the reality of considering plasma instabilities. In a perspective view, planning of future modulated experiments for the purposes of power deposition localization will have to deal with both the following information: the information extrapolated from the study carried out in the previous chapters and the importance of the large scale instabilities of the plasma. *don*

Chapter IX summarizes the work and the results and suggests ideas for future experiments that could improve our knowledge concerning the power deposition.

Chapter X lists the bibliography and, finally, the appendix presents a series of algorithms and plots that were used during these past four months.

Ce n'est pas une introduction mais une
présentation de
résumé plus ou moins résumé du rapport.

L'introduction devrait être comprise:

contenue: localisation du dépôt ECRH pour

- réalisation des ECRH

- étude exp. du plasma chauffée
(transport, ajustement profils
Te et comant, ...)

problèmes: transport mal connu \Rightarrow

corrects difficulté de séparer transport
et chauffage

outil: méthodes numériques (en général)

acquis: bel recueil des travaux déjà
publiés dans ce domaine

~~sujet traité :~~

motivation: Les résultats ^{obts} ainsi déduits
sont-ils fiables?

outil: étude de la ^{sensibilité} robustesse des
résultats à une variation du
modèle

résultats: - quantification de la
nouveau qualité des résultats

en erreur - indépendance par rapport
au modèle de transport

- optimisation des paramètres
exp.

Index

Acknowledgements	i
Abstract	iii
Outline	iv
I. Introduction	1
I.1 Nuclear fusion	1
I.2 Fusion and tokamaks	2
I.3 The problem of transport in plasma	3
II. The experimental facilities	5
II.1 The tokamak TCV	5
II.2 Electron Cyclotron Resonance Heating (ECRH)	6
II.3 Soft X-ray tomography system	7
III. Study of the problem	9
III.1 Stationary transport equation	9
III.1.1 The simplest case	9
III.1.2 Extension of the equation	11
III.2 Non-stationary transport equation	13
III.2.1 Fourier analysis of the problem	13
III.2.1.1 Amplitude variations	14
III.2.1.2 Phase variations	16
III.2.1.3 General remarks	17
III.2.2 Complete time evolution	18
IV. Formalization of the problem	21
IV.1 Idea and development: the J2 matrix	21
IV.2 Application of J2	23
IV.3 Quantification of the variations	24
V. Analysis of temperature profiles	26
V.1 Stationary temperature profiles	26
V.2 Temporal evolution	28

V.4 Investigation of J2	32
V.4.1 Heating in the center	32
V.4.2 Heating half way to the edge	33
V.4.3 Heating far from the center	34
V.4.4 Remark on the calculated matrices	34
VI. Modulation of the source	37
VI.1 The non modulated case	37
VI.2 Sinusoidal modulation	39
VI.3 Modulation with random binary signal	41
VI.4 Modulation with a square signal	43
VI.4.1 Regularly spaced signal	43
VI.4.2 Optimized square signal	46
VI.5 Summarizing and remarks	48
VII. Reconstruction of the parameters	49
VII.1 Reconstruction	49
VII.1.1 No modulation	49
VII.1.2 Regularly spaced modulation	50
VII.1.3 Optimized modulation	50
VII.1 Results and discussion	51
VIII. Analysis of TCV shot # 12508	53
VIII.1 TCV shot # 12508	53
VIII.2 Tomography data processing	54
VIII.3 Parameters reconstruction	56
IX. Conclusions	61
X. Bibliography	63
Appendix	64
A. List of the algorithms	64
B. Plots of stationary T profiles	71
C. Plots of temporal evolution of T profiles	74
D. Normalization of J2	75
E. List of calculated D and V matrices	77
F. Plots of T profiles with modulated sources	81
G. Scope survey of TCV shot #12508	83
H. Experimenta vs. reconstructed profiles	85

Ai miei genitori

I. Introduction

I.1 Nuclear fusion

In today's commercial nuclear power plants the energy is produced using the principle of nuclear fission: the nucleus of a heavy atom (usually uranium 235) is fissioned by a neutron into two smaller fragments. The total mass of the two fragments is smaller than that of the initial atom of uranium, and the energy difference is freed in the form of heat. *not directly, rather kinetic energy of the products*

The idea of a power plant based on the principle of nuclear fusion is definitely more ambitious, since it aims to reproduce the reactions that take place in the center of the sun. There are many different ways to make fusion (see Table I.1), and the reaction chosen is the D-T reaction.

(²H - ³H)

Reaction	Released energy [MeV]
${}^2_1\text{H} + {}^3_1\text{H} \rightarrow {}^4_2\text{He} + {}^1_0\text{n}$	17.61
${}^2_1\text{H} + {}^2_1\text{H} \rightarrow {}^3_2\text{He} + {}^1_0\text{n}$	3.27
${}^2_1\text{H} + {}^2_1\text{H} \rightarrow {}^3_1\text{H} + {}^1_1\text{p}$	4.03
${}^2_1\text{H} + {}^3_2\text{He} \rightarrow {}^4_2\text{He} + {}^1_1\text{p}$	18.35

Table I.1: list of possible fusion reactions.

When a nucleus of deuterium *D* fuses with a nucleus of tritium *T*, an α -particle *⁴He* is produced and a neutron *n* is emitted. The energy released is 17.6 MeV per reaction (14 MeV for the neutron and 3.6 for the α -particle). In order to induce the fusion of nuclei of deuterium and tritium, it is necessary to overcome the Coulomb repulsion due to the two positive charges of the hydrogen ions. The most promising method of supplying the energy is to heat the deuterium-tritium fuel to a sufficiently high temperature that the thermal velocities of the nuclei are high enough to produce the required reaction. Fusion brought about in this way is called thermonuclear fusion. *only the impact*
The necessary temperature lies around 10 keV. *(? °C)*

At such temperatures the fuel is fully ionised and the resulting gas is called plasma. Since such high temperatures preclude confinement by material walls, another method has to be found for this purpose. Two main approaches are studied nowadays: magnetic and inertial confinement. The method studied at the CRPP is the method of magnetic confinement in a toroidal configuration, the Tokamak.

I.2 Fusion and tokamaks

In a tokamak the plasma particles are confined into a toroidal volume by a magnetic field, being held in small gyrating orbits. In a reactor the energy must be retained for sufficiently long time that the losses (Bremsstrahlung plus conduction and convection) are equal to the heating of the plasma by the energetic α -particle released by the fusion reactions themselves. The Lawson criterion gives the relationship between the density and the confinement time needed for the ignition to take place: at the required ion density of around 10^{20} m^{-3} , this time is of the order of a second.

The main field in a tokamak is the toroidal magnetic field. However, this field alone does not allow confinement of the plasma. In order to have an equilibrium in which the plasma pressure is balanced by magnetic forces, it is also necessary to have a poloidal magnetic field. In a tokamak this field is mainly produced by currents in the plasma itself. The following figure shows a scheme of a tokamak.

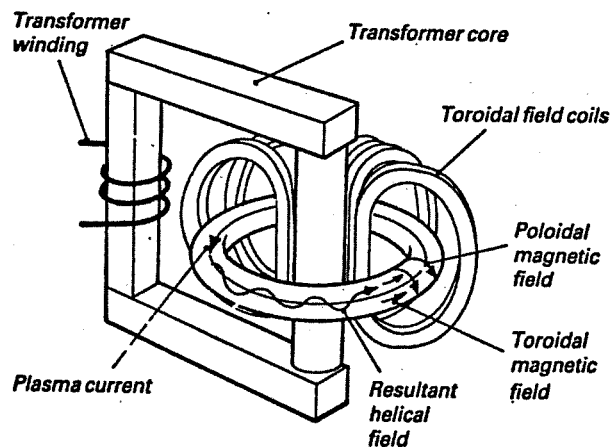


Figure I.1: scheme of a tokamak.

The resulting motion of the particles of the plasma can then be derived from the equation of motion of a charged particle in a magnetic field. The equation is

$$m_j \cdot \frac{d\vec{v}}{dt} = e_j \cdot \vec{v} \times \vec{B}$$

where j stands for electron and ion respectively.

If the magnetic field is uniform the components of this equation are

$$\frac{dv_x}{dt} = \omega_{cj} \cdot v_y, \quad \frac{dv_y}{dt} = \omega_{cj} \cdot v_x, \quad \frac{dv_z}{dt} = 0,$$

where

$$\omega_{cj} = \frac{e_j B}{m_j}$$

is the cyclotron frequency and the z axis has been chosen to be along the toroidal field. The solutions of these equations may be written as

$$x = -\rho_j \cdot \cos \omega_{cj}t, \quad y = \rho_j \cdot \sin \omega_{cj}t,$$

where

$$\rho_j = \frac{v_{\perp}}{\omega_{cj}} = \frac{m_j v_{\perp}}{e_j B}$$

is the Larmor radius. Thus, the particle has a helical orbit composed of a circular motion around the field lines and a constant velocity in the direction of the magnetic field. Table I.2 gives some typical values of the cyclotron frequency and Table I.3 some values of the Larmor radii for electrons and protons.

Frequency	Magnetic field		
	1 Tesla	3 Tesla	5 Tesla
$ \omega_{ce} $ (s ⁻¹)	$1.76 \cdot 10^{11}$	$5.28 \cdot 10^{11}$	$8.79 \cdot 10^{11}$
ω_{cp} (s ⁻¹)	$9.58 \cdot 10^7$	$2.87 \cdot 10^8$	$4.79 \cdot 10^8$
f_{ce}	28 GHz	84 GHz	140 GHz
f_{cp}	15 MHz	46 MHz	76 MHz

Table I.2

B	Larmor radius	Temperature		
		100 eV	1 keV	10 keV
3 T	ρ_e	0.011 mm	0.035 mm	0.11 mm
	ρ_p	0.48 mm	1.5 mm	4.4 mm
5 T	ρ_e	0.007 mm	0.021 mm	0.067 mm
	ρ_p	0.29 mm	0.91 mm	2.9 mm

Table I.3

Next, it is important to say a few words about one of the biggest problems that the research in fusion through magnetic confinement is currently facing: the problem of transport in a plasma.

I.3 The problem of transport in plasma

There are many good reasons to study the transport in thermonuclear plasma. The first one is that there are many aspects that are not understood. Reference [1] gives an overview of the above-mentioned problems. The second reason is the fact that the development of nuclear fusion reactors badly needs an understanding of transport. One aim is a reduction of the thermal transport, with the objective of decreasing the required size of the reactor. Even more important is the possibility of

running a burning plasma at a reduced heat flux, the energy exhaust being currently one of the most challenging of the technological problems.

Considering the conservation laws, the equation that governs the transport of energy is expressed as

$$\frac{3}{2} \frac{\partial}{\partial t} (nT) = -\bar{\nabla} \cdot \bar{q} + Q \quad (I-1)$$

where n , \bar{q} and Q represent density, heat flux and source of thermal energy (in our case Q will represent the external heat source of ECRH, see later). The question now becomes: how is the flux related to the thermodynamical forces? The most widely used model is the diffusive model, which links the heat flux to the temperature gradient through two phenomenological coefficients, the coefficients of diffusion and convection. The flux then has the following form

$$\bar{q} = -n\chi\bar{\nabla}T + \frac{3}{2}n\bar{v}T \quad (I-2)$$

where χ and \bar{v} represent the diffusion and convection coefficients respectively.

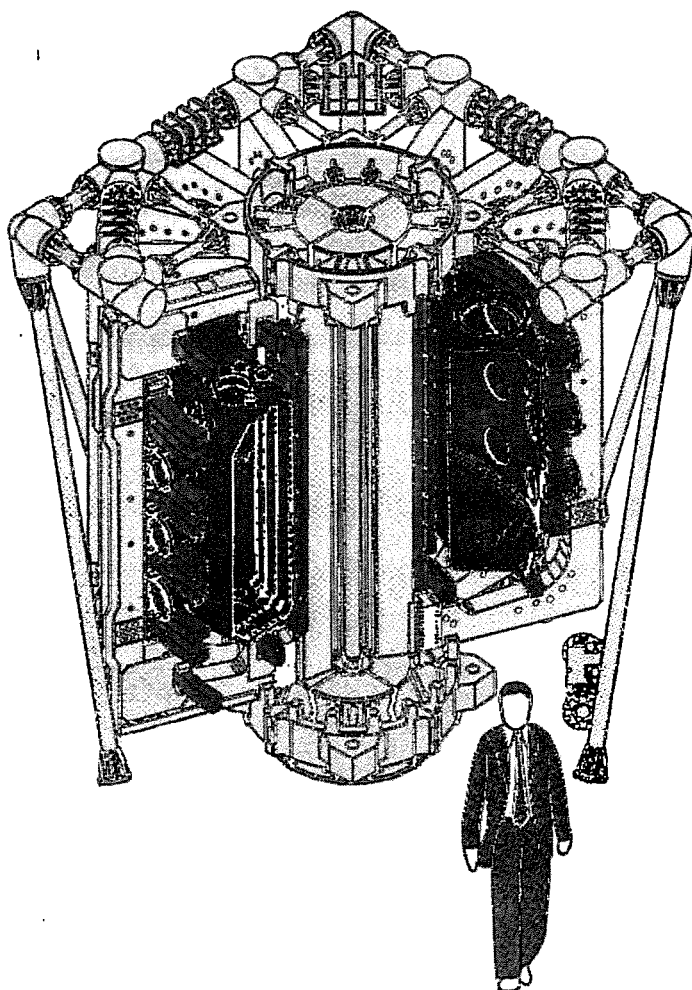
The problem of transport in the plasma deals with the fact that the coefficients of diffusion and convection are not known a priori and are not directly experimentally measurable.

Le problème de la séparation ∇T et q pourrait être introduit ici

II. Experimental facilities

II.1 The tokamak TCV

The Tokamak à Configuration Variable (TCV, see figure II.1) is unique in the world, due to the possibility of widely varying the plasma shape. It was conceived to study the impact of high elongation and strong shaping. This is motivated by the scaling of the energy confinement, which shows that high elongation should lead to a significantly improved confinement time.



Green: vacuum vessel.
Red: support structure.
Cyan: toroidal magnetic field coils.
Blue: poloidal magnetic field coils for the modeling of the plasma shape.

Figure II.1

A list of the main parameters of TCV is shown below.

Maximum plasma current	1.2 MA
Achieved plasma current	1.0 MA
Major radius	0.89 m
Minor radius	0.24 m
Plasma half height	0.72 m
Maximum elongation	3
Achieved elongation	2.58
Toroidal magnetic field	1.45 T
Plasma pulse length	2 s

To reach ignition for the fusion reactions, high temperatures are needed (ion temperature around 10 keV), and ohmic heating is limited by the characteristic that the plasma conductivity increases rapidly with the temperature ($\sigma \propto T_e^{3/2}$, where T_e is the electron temperature), therefore additional heating systems are required. High power gyrotrons for Electron Cyclotron Resonance Heating (ECRH, see section II.2) have been chosen for the required additional power supply.

Diagnostics on TCV are numerous and include a 200 channel X-ray tomography system, a 64 channel multibolometer, a 35 channel Thomson scattering system, a multichannel FIR interferometer, 72 tile-embedded Langmuir probes, an infrared camera for power deposition measurements and a neutral particle analyzer [2].

II.2 Electron Cyclotron Resonance Heating (ECRH)

The principle of ECRH is to transfer power from a radio-frequency wave to the electrons in the plasma. It is of great interest in TCV in particular because the heating location, to be verified experimentally, can be chosen at virtually any point in the plasma. Values of T_e of more than 4 keV have already been reached with an input power of 1 MW. []

ECRH is widely used in present-day tokamaks and is planned for applications in ITER (International Thermonuclear Experimental Reactor). It can be used for a wide range of goals starting with bulk heating, to plasma profile *modeling* *in particular* plasma current tailoring, with the aim of enhancing or optimizing stability and confinement properties.

ECRH directly heats the electrons. Depending on the tokamak magnetic field and on the cyclotron harmonic at which the ECRH is designed, high power heating experiments are conducted at frequencies varying between 40 and 160 GHz and at operating densities where the electrons and the ions are generally decoupled, due to

the fact that the electron-ion equipartition time exceeds the energy confinement time, and ECRH has little effect on the ion temperature [3].

The Electron Cyclotron Wave System of TCV, once completed, will include a set of 9 gyrotrons providing a total power of 4.5 MW: of these, 3 MW at the second electron cyclotron harmonic (81.76 GHz) and 1.5 MW at the third harmonic (118 GHz) [4].

The good localization of ECRH power deposition in the discharge allows, in principle, the use of power modulation techniques to extract heat diffusivity and heat convection coefficients from the analysis of the perturbed temperature profiles.

II.3 Soft X-ray tomography

The best way to reconstruct the electron temperature profile evolution of the plasma, is, because of time and spatial resolution, to study the continuous X-ray emission spectrum.

In a hot plasma composed of electrons and hydrogen ions, the electron-ion collisions give rise to electromagnetic emission called bremsstrahlung. Because typical electron temperatures in a tokamak are in the region of keV, most of the bremsstrahlung power will be in the soft X-ray region. For a Maxwellian distribution of electrons, the continuous X-ray spectrum has the form

$$\frac{dN}{dE_x} = \alpha n_e n_i \frac{g_{ff} e^{-E_x/T_e}}{E_x \sqrt{T_e}}, \quad T_e \text{ in eV} \quad (\text{II-1})$$

where $\frac{dN}{dE_x}$ represents the number of quanta emitted per eV, per s, into 4π

steradians by a plasma of 1 m^3 volume;

E_x is the X-ray energy (eV); $\alpha = 9.6 \cdot 10^{-20} \text{ eV}^{1/2} \text{ m}^3 \text{ s}^{-1}$; $g_{ff} \approx 1$;

n_e and n_i are the electron and ion densities respectively.

This strong exponential dependence allows the determination of the electron temperature from experimental measurements of dN/dE_x . A more detailed form of (II-1), taking into account the impurity ions of the plasma, is left to references [3] and [5].

The system mounted on TCV makes use of 10 cameras with 20 detector elements each (see next figure).

TCV XTOMO

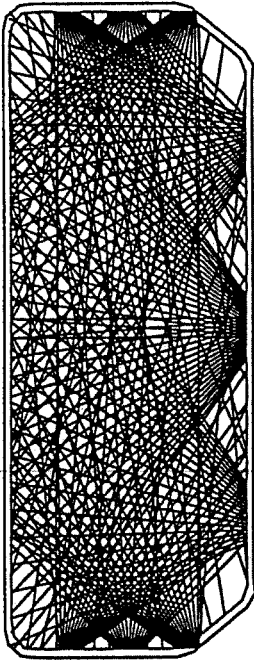


Figure II.2

The system uses 10 linear arrays of 20 Si PIN diodes directly mounted on preamplifier boards placed in 9 ports.

Beryllium windows of 47 μm thickness serve both to block out visible and VUV radiation and to separate the machine vacuum from that of the cameras.

A more complete presentation of the soft X-ray tomography system on TCV can be found in reference [7].

Temporal resolution: maximum acquisition frequency is 10kHz.

Spectral resolution: between 1keV and 30keV is essentially 100% ([3]).

III. Study of the problem

The equation governing the phenomena of transport in ECH-heated plasmas is the continuity equation for the energy, and it is given by

$$\frac{3}{2} \frac{\partial}{\partial t} (nT) = -\bar{\nabla} \cdot \bar{q} + Q \quad (\text{III-1})$$

where n represents the electron density, T the electron temperature and Q the external heat source and where the heat flux \bar{q} is expressed as

$$\bar{q} = -n\chi\bar{\nabla}T + \frac{3}{2}n\bar{v}T \quad (\text{III-2})$$

with the diffusion coefficient χ and the convection coefficient v . Diffusion and convection are generally space-dependent but time-independent. Because of the geometry of the toroidal configuration, it is possible to simplify the equation introducing cylindrical coordinates (the simplification of a cylindrical plasma, though, is only a rough approximation). In this case, the following substitutions

$$\bar{\nabla} = \frac{\partial}{\partial r}, \quad \bar{\nabla} \cdot \bar{\cdot} = \frac{1}{r} \frac{\partial}{\partial r} (r \cdot \cdot), \quad Q = Q(r, t), \quad T = T(r, t)$$

lead to

$$\frac{3}{2} \frac{\partial}{\partial t} (nT) = -\frac{1}{r} \frac{\partial}{\partial r} r \left(n\chi \frac{\partial T}{\partial r} + \frac{3}{2} n v T \right) + Q(r, t) \equiv L \cdot T + Q(r, t) \quad (\text{III-3})$$

The objective is now to solve (III-3) for the electron temperature T and to study the profile identified in this way with respect to the different parameters involved.

expliquer mieux: liste paramètres, différentes situations (stationnaire)

III.1 Stationary transport equation

III.1.1 The simplest case

As a first approach, it is convenient to solve the stationary continuity equation. Making the assumptions of constant density ($n = n_0$), constant diffusion coefficient

($\chi = \chi_0$), and negligible convection ($v=0$) and setting $Q = Q(r) = Q_0(1 - r^2/a^2)^1$, the equation becomes

$$n\chi_0 \frac{1}{r} \frac{\partial}{\partial r} r \frac{\partial T}{\partial r} = Q_0 \left(1 - \frac{r^2}{a^2}\right) \quad \text{(III-4)}$$

with the boundary conditions $T(a)=0$ and $\frac{\partial T}{\partial r}\Big|_{r=0} = 0$.

(III-4) can be easily solved with an eigenmode decomposition of the differential operator $\frac{1}{r} \frac{\partial}{\partial r} \left(r \frac{\partial}{\partial r} \right)$. The eigenmode equation takes the form

$$D \frac{1}{r} \frac{\partial}{\partial r} r \frac{\partial}{\partial r} T_k(r) = \lambda_k T_k(r) \quad \text{(III-5)}$$

Its solutions are the Bessel functions² of first and second order:

$$T_k(r) = c_k \cdot J_0(\alpha_k r / a) + d_k \cdot N_0(\beta_k r / a) \quad k=1, \dots \quad \text{(III-6)}$$

where α_k, β_k are the zeros of respectively J_0 and N_0 .

Because of the boundary conditions d_k becomes 0 for all k and $\lambda_k \equiv c_k$ for all k . It follows that

$$T(r) = \sum_k J_0\left(r \frac{\alpha_k}{a}\right) c_k \quad \text{(III-7)}$$

and

$$D \frac{1}{r} \frac{\partial}{\partial r} \left(r \frac{\partial T(r)}{\partial r} \right) = D \sum_k J_0\left(r \frac{\alpha_k}{a}\right) c_k \frac{\alpha_k^2}{a^2} = Q_0 \left(1 - \frac{r^2}{a^2}\right) \quad \text{(III-8)}$$

(III-8) can now be evaluated numerically³. The following figure shows the resulting amplitude of the temperature profile, as a function of $x=r/a$ and for different values of $D = n\chi_0^4$.

¹ Q_0 must satisfy $\int dV Q(r) = 1 \text{ MW}$

² More on Bessel functions: see for example [7]

³ Algorithm serie1_def.m (Matlab 4.2c)

⁴ $10^{19} \text{ m}^{-1}\text{s}^{-1} < n\chi_0 < 10^{20} \text{ m}^{-1}\text{s}^{-1}$

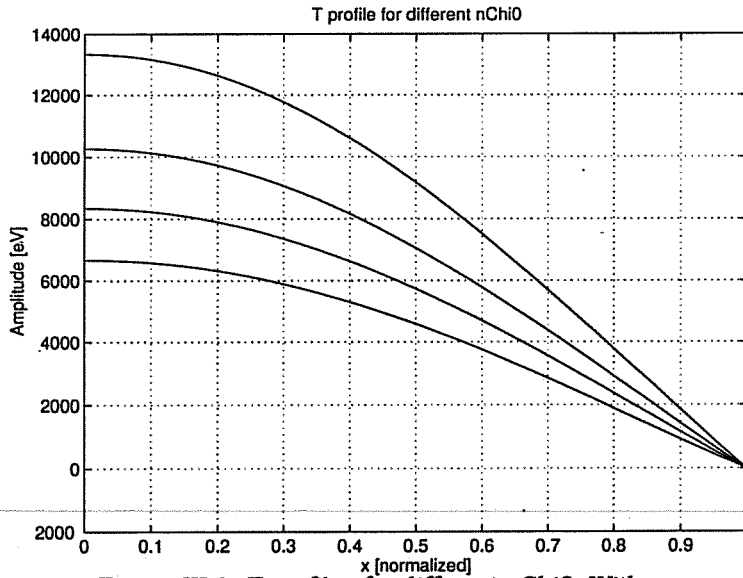


Figure III.1: T profiles for different $n\chi_0$. With increasing parameters the amplitude of the profile decreases.

It can be easily seen that the amplitude of the temperature profile is strongly D -dependent, but not the overall stage.

III.1.2 Extension of the equation

The next step consists of introducing a more general model for the diffusion coefficient and taking into account the convection term too. For these quantities, the following assumptions are made: $n\chi = n\chi_0 + n\chi_1 \cdot \frac{r^2}{a^2}$ and $v = v_0 \cdot \frac{r}{a}$

(III-5) then becomes

$$\frac{1}{r} \frac{\partial}{\partial r} r \left(n\chi(r) \frac{\partial T(r)}{\partial r} + n(r)v(r)T(r) \right) = Q(r) \quad (\text{III-9})$$

Because of the non-zero convection factor $v(r)$, a radial profile for the density is also needed. For our purpose it is convenient to assume a simple quadratic form:

$$n(r) = n_0 \left(1 - r^2/a^2 \right)$$

Again we look for the eigenmodes of the transport operator. Section III.1.1 already suggests an ansatz for the eigenmodes: *not introduced*

$$T_k(r) = \sum_1 J_0 \left(\frac{r}{a} \alpha_1 \right) d_{1k} \quad (\text{III-10})$$

Putting (III-10) into (III-5) gives

$$\sum_l M_{kl} d_{lk} = \sum_l J_0 \left(\frac{r}{a} \alpha_l \right) d_{lk} \cdot c_k \quad (III-11)$$

with M_{kl} a very long expression containing all the explicit derivatives. \rightarrow in annex

On the other hand we have

$$T(r) = \sum_k T_k(r) b_k$$

$$L \cdot T(r) = L \cdot \sum_k T_k(r) b_k = \sum_k L \cdot T_k(r) b_k = \sum_k T_k(r) c_k b_k$$

and with $Q(r) = \sum_k T_k q_k$

it follows $b_k = \frac{q_k}{c_k}$

où est passé le profil de r ?

This set of equations can be also easily solved numerically⁵.

In order to generalize $n\chi(r)$ and $v(r)$ to any radial profile, it is convenient to discretize the differentiation operators inside the transport operator. Again setting (III-10) as the ansatz for $T(r)$, the transport operator reduces to ($x=r/a$)

$$L \cdot T = \frac{e}{a^2} \sum_k \left[\left(\frac{-grad(n\chi) J_1(x\alpha_k) \alpha_{kk}}{a} - \frac{n\chi J_0(x\alpha_k) \alpha_{kk}^2}{a^2} \right) + \frac{3}{2} (div(nv) J_1(x\alpha_k) - \frac{anv J_1(x\alpha_k) \alpha_{kk}}{a}) \right] T_k$$

pas introduit avant \rightarrow par \checkmark nécessaire

where $grad$ and div are the above mentioned discretized operators and e is the electron charge so that T is finally expressed in eV. \checkmark

Putting in the usual expressions for diffusion and convection coefficients, it is now possible to evaluate some temperature profiles for different values of $n\chi_0$, $n\chi_1$ and v_0 and further to compare the resulting graphical solutions with those of the previous simplification in order to check the validity of the modifications.

The following figure shows the calculated⁶ temperature profiles for different values of diffusion and convection coefficients.

$$T(x) = \sum_k J_0(x\alpha_k) d_k$$

$$L \cdot T + Q = 0 \Leftrightarrow \sum_k L J_0(x\alpha_k) d_k + Q(x) = 0$$

$$\rightarrow L J_0 = -\frac{Q(x)}{J_0} = [] \text{ solve for } d_k$$

⁵Algorithm serie2_def.m (Matlab 4.2c)
⁶Algorithm serie3_def.m (Matlab 4.2c)

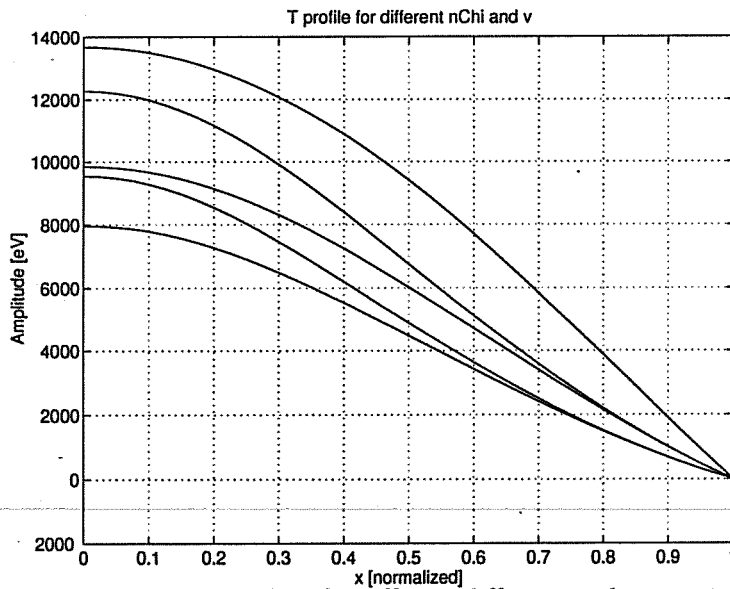


Figure III.2: T profiles for different diffusion and convection parameters. The top curve represents $n\chi_1$ and v_0 equal zero; the four below are coupled: two different $n\chi_1$'s and each time once v_0 equal 0 and once different than 0.

The top profile in figure III.2 represents the case of constant diffusion coefficient ($n\chi_0 = 10^{19} \text{ m}^{-1}\text{s}^{-1}$) and no convection ($v_0 = 0$), while the other four profiles were calculated for two different values of $n\chi_1$ (holding $n\chi_0$ constant), one time with zero convection and one time with non-zero convection. A positive convection induces a movement of particles towards the center ($x=0$) and therefore it produces a higher temperature compared to the non-convection case.

not in eq. III.2

III.2 Non-stationary transport equation

Next, non-stationarity has to be taken into account, and the term on the left-hand-side of (III-3) can no longer be suppressed. The more common methods of dealing with those kinds of equations are Fourier and Laplace transformation analysis. Here we will spend a few words on the Fourier method on the way to the complete time evolution of the temperature profile. More on the Laplace analysis can be found, for example, in references [3], [8] and [9].

III.2.1 Fourier analysis of the problem

The studied equation is, again, the following

$$\frac{3}{2} \frac{\partial}{\partial t} (nT) = -\frac{1}{r} \frac{\partial}{\partial r} r \left(n\chi \frac{\partial T}{\partial r} + \frac{3}{2} nvT \right) + Q(r, t) \quad \text{(III-12)}$$

Modulating the external source Q with a frequency ω , setting

$$Q(r, t) = Q(r) \cdot e^{-i\omega t} \quad \text{with} \quad Q(r) = Q_0 e^{-\left(\frac{r-r_0}{\Delta r}\right)^2}$$

which closely represents a ECRH source and setting $n(r) = (n_0 - n_a)\left(1 - r^2/a^2\right) + n_a$, through Fourier transformation, equation (III-12) takes the form

$$\frac{3}{2} i\omega n \hat{T} = L \cdot \hat{T} + Q(r)$$

which leads to the solution (in the (r, ω) -space)

$$\hat{T}(r, \omega) = \left(\frac{3}{2} i\omega n - L\right)^{-1} \cdot Q(r) \quad \text{(III-13)}$$

It is now possible to study this solution⁷ in the (r, ω) -space varying the different parameters involved. T can then be seen as a multi-variable function of the set of parameters

$$p = \left[f \text{ [Hz]}, r_0 \text{ [m]}, \Delta r \text{ [m]}, P_{in} \text{ [W]}, n_0 \text{ [m}^{-3}\text{]}, n_a \text{ [m}^{-3}\text{]}, \right. \\ \left. n\chi_0 \text{ [m}^{-1}\text{s}^{-1}\text{]}, n\chi_1 \text{ [m}^{-1}\text{s}^{-1}\text{]}, v_0 \text{ [ms}^{-1}\text{]} \right] \quad \text{(III-14)}$$

where $\omega = 2\pi f$. Appendix B lists a series of figures showing the different variations of both amplitude and phase of the temperature profile with respect to the different parameters of p . A brief discussion of these dependencies follows.

III.2.1.1 Amplitude variations

Depending on which parameter is left free to vary, different changes in the profile are observed. In order to understand the influence of each of these parameters, a reference p_0 is chosen and variations around this reference point are observed. The chosen p_0 is

$$p_0 = \left[f \text{ [Hz]}, r_0 \text{ [m]}, \Delta r \text{ [m]}, P_{in} \text{ [W]}, n_0 \text{ [m}^{-3}\text{]}, n_a \text{ [m}^{-3}\text{]}, \right. \\ \left. n\chi_0 \text{ [m}^{-1}\text{s}^{-1}\text{]}, n\chi_1 \text{ [m}^{-1}\text{s}^{-1}\text{]}, v_0 \text{ [ms}^{-1}\text{]} \right] = \quad \text{(III-15)} \\ = [10, 0.35, 0.08, 10^6, 2.5 \cdot 10^{19}, 1 \cdot 10^{18}, 10^{19}, 6 \cdot 10^{19}, 7.5]$$

⁷Algorithm tprofile.m (Matlab 4.2c)

Figure B.1a in appendix B shows the amplitude profile for $T=T(p_0, x)$, where $x=r/a$ (normalized units).

(i) Frequency changes (figure B.2a). Increasing the frequency has two consequences: it produces a global decrease of the resulting temperature distribution and it provides a better focus on the region of power deposition. These observations are easy to understand if we look at the physical meaning of high or low frequency f in the usual (r, t) -space: $f=0$ produces the temperature profile corresponding to $t = \infty$, that means, the stationary profile, while the increasing f leads to the early stages of the temporal evolution of the profile, region where the localisation of the deposition is easier due to the finite time needed by diffusion and convection phenomena to take place and to start influencing the heated particles.

(ii) Diffusion changes (figure B.3a). A decrease (resp. increase) of the $n\chi_1$ coefficient of diffusion leads to an increase (resp. decrease) of the temperature distribution. This is obvious if we think of the physics of diffusion: less diffusion effects actually means better conduction due to fewer energy losses; higher temperatures are then expected. On the other hand, a greater diffusion coefficient means that the energy losses are bigger, leading to lower temperatures.

(iii) Convection changes (figure B.4a). the physical meaning of convection is again enlightening for the explanation of its dependence for the temperature profile: positive convection means transport of particles towards the central region ($x=0$), and therefore an increase of T in the center, while negative convection means transport towards the outer regions leading to a smaller T in the center.

(iv) Deposition coordinates changes (figure B.5a+b). The closer to the center the external power is deposited, the higher temperatures are reached, and vice versa; this is understandable if we think of the system we are dealing with, a toroidal configuration approximated in cylindrical coordinates. Consider the next two figures:

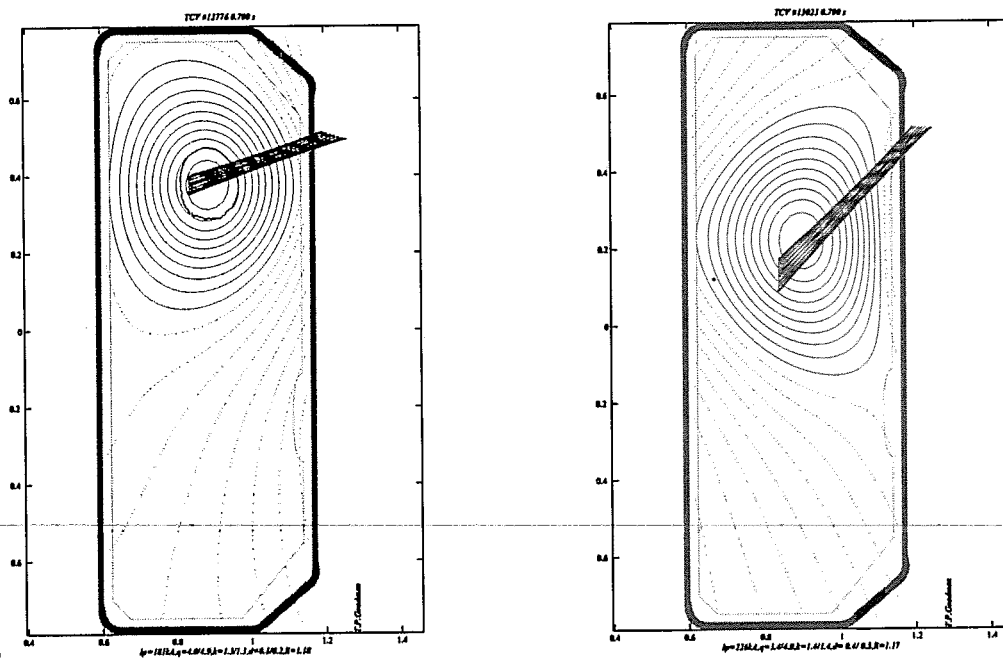


Figure III.3a/b: difference between heating in the center or in outer regions.

Heating in the center means heating in a very localized area with small volume; heating outside means heating the "skin" of a cylinder, equivalent to a bigger volume. The result is a much larger effectiveness if heating near the center.

For the varying of the width of the heat source (Δr), the result is similar: if the source is concentrated into a smaller spatial region, the heating will be more effective, while a larger Δr will produce more energy dissipation and the heating will not be very effective.

(v) ~~Density changes~~(figure B.6a). With increasing density, a sharpening of the profile towards the center is observed, denoting an increase of importance of the convection term inside the transport operator; although it becomes sharper, the profile suffers a loss in magnitude. For lower densities, instead, convection phenomena become smaller, showing a sharpening of the profile in the outer regions, in the vicinity of the deposition.

(vi) ~~External power changes~~. The temperature profile is linearly proportional to the incoming external power, which is evident if looking at the transport equation.

III.2.1.2 Phase variations

Figure B.1b in Appendix B shows the phase profile for $T=T(p_0, x)$.

(i) ~~Frequency changes~~ (figure B.2b). The profile of the phase of T clearly shows a maximum in the region of the power deposition. The higher the frequency is, the sharper the maximum becomes, a characteristic that has already been observed in the case of the amplitude. Modulating at a sufficiently high frequency allows, in principle, the localization of the power deposition.

(ii) Diffusion changes (figure B.3b). Higher diffusion coefficients produce an enlargement of the profile and the loss of the well defined maximum, while lower diffusion (better conduction) improves the quality of the peak.

(iii) Convection changes (figure B.4b). Convection changes have very little effect on the quality of the profile's maximum. Their main effect is a translation of the whole curve towards higher values.

(iv) Deposition coordinates changes (figure B.5c/d). Changes of r_0 and Δr affect the curve in a logical way: varying the deposition coordinate r_0 , its maximum follows the modification, while varying the width of the external source, the definition of the peak improves if Δr decreases or worsens if Δr increases.

(v) Density changes(figure B.6b). Density variations produce similar consequences to those of the frequency variations and show opposite behaviour to the diffusion variations. With higher densities the maximum of the curve tends to become sharper, while with decreasing n , the profile becomes flatter and the phase moves towards zero.

(vi) External power changes. Variations of P_{in} have no effect on the phase.

III.2.1.3 General remarks

From all the observations made, a first feeling of how each parameter influences the temperature profile can be gained, and a few remarks can already be pointed out.

First of all, it is clear that the chosen modulation frequency plays a great role in the problem of the localization of the supplementary heating. If the frequency is high enough to prevent heat diffusion and convection over a distance larger than the spatial resolution required, the bulk temperature oscillates in the region where the power is deposited, drawing the energy deposition profile. Furthermore, the frequency cannot be too high either, since increasing frequency leads to profiles with smaller amplitudes. This means that increasing the modulation frequency too much would lead to the impossibility of measuring the temperature profile because of the requirements needed for the temperature resolution. Further discussions of this technique for the measurement of the energy deposition profile and the study of the plasma transport properties can be found in references [10], [12] and [13].

A second remark concerns the fact that the variation of one particular parameter can induce similar changes to the temperature profile as the variations of others. This means that, in principle, it could be possible that two or more parameters could be chosen in such a way that the resulting profile would suffer only of very small perturbations compared to the starting profile, leading to the impossibility of a clear separation and identification of the two profiles.

Having clarified this, it is now evident that a formalization of the problem is needed in order to understand the importance and the weight of each parameter in the construction of the temperature profile. This formalization is done later in Chapter IV.

What follows, we present the last step to reach the final solution of the transport equation, providing the complete time evolution of the temperature profile.

III.2.2 Complete time evolution

Finally, the complete power balance equation is solved. Using the discretized operators *grad* and *div* inside the transport operator L (section III.1.2), it is convenient to rewrite the differential equation in the following form:

$$\frac{\partial T}{\partial t} = \sum_k J_0(\alpha_k x) \frac{\partial T_k}{\partial t} = \sum_k \frac{2}{3en(r)} L T_k + \frac{2}{3en(r)} Q(r) U(t)$$

or

$$\begin{cases} \frac{\partial T_n}{\partial t} = J_0^{-1}(\alpha_k x) \frac{2}{3en(r)} L T_k + J_0^{-1}(\alpha_k x) \frac{2}{3en(r)} Q(r) U(t) \\ T = \sum_k J_0(\alpha_k x) T_k \end{cases} \quad \text{(III-16)}$$

expliquer

$U(t)$ defines the temporal behaviour of the heat source $Q(r)$.

(III-16) is a particular case of the more general differential equation system

$$\begin{cases} \dot{x} = Ax + Bu \\ y = Cx + Du \end{cases}$$

where

$$A = J_0^{-1}(\alpha_k x) \frac{2}{3en(r)} L, \quad B = J_0^{-1}(\alpha_k x) \frac{2}{3en(r)} Q(r), \quad u = U(t),$$

$$C = J_0(\alpha_k x), \quad D = 0, \quad x = T_k, \quad y = T.$$

This system can now be solved numerically using a simulation function of continuous-time linear system to arbitrary inputs⁸. Figure III.4 shows the three-dimensional simulation of a calculated temperature evolution. The term governing the temporal behaviour of the external source is, in this case, simply $U(t)=1$ for all t 's.

*III - formalisation pour phase
- simulation numérique pour whole
- à part la présentation du modèle
(Ch. 1.2 about) c'est un peu une*

⁸Matlab 4.2c function `lsim` in algorithm `evolution1.m`

- points à relever 18- notes : phase de la mod. 0 fs, "early phase"

T profile evolution for $p=[.35 .08 1E6 2.5E19 1E18 1E19 6E19 8]$

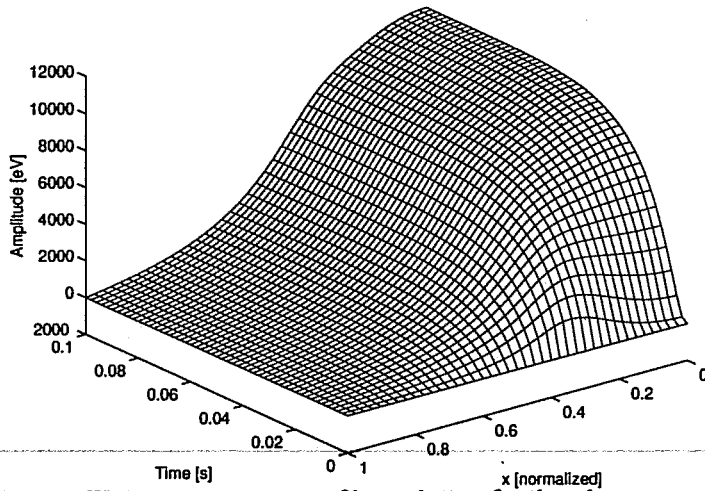


Figure III.4: temperature profile evolution for the above mentioned set of parameters and for $U(t)=1$.

The set of parameters defining the temperature profile evolution no longer explicitly contains the frequency. Implicitly the modulation is still contained, though, being held by the term $U(t)$ that multiplies the external source $Q(r)$. The explicit set of parameters upon which T depends becomes:

$$p = [x_0, \Delta x, P_{in} [W], n_0 [m^{-3}], n_a [m^{-3}], n\chi_0 [m^{-1}s^{-1}], n\chi_1 [m^{-1}s^{-1}], v_0 [ms^{-1}]] \quad (III-17)$$

The normalized parameters x_0 and Δx have been chosen instead of the real parameters r_0 and Δr for the definition of the external heat source Q .

Looking at the figure, it can be seen that the stationary profile is reached very quickly. This "rising time" towards stationarity will become very important later on.

*with
some
Habit*

Appendix C presents a series of figures showing a few temperature profile evolutions as a function of the normalized radius and time, as well as for a few different regions of deposition, of which two graphs are reproduced in Figure III.5a/b.

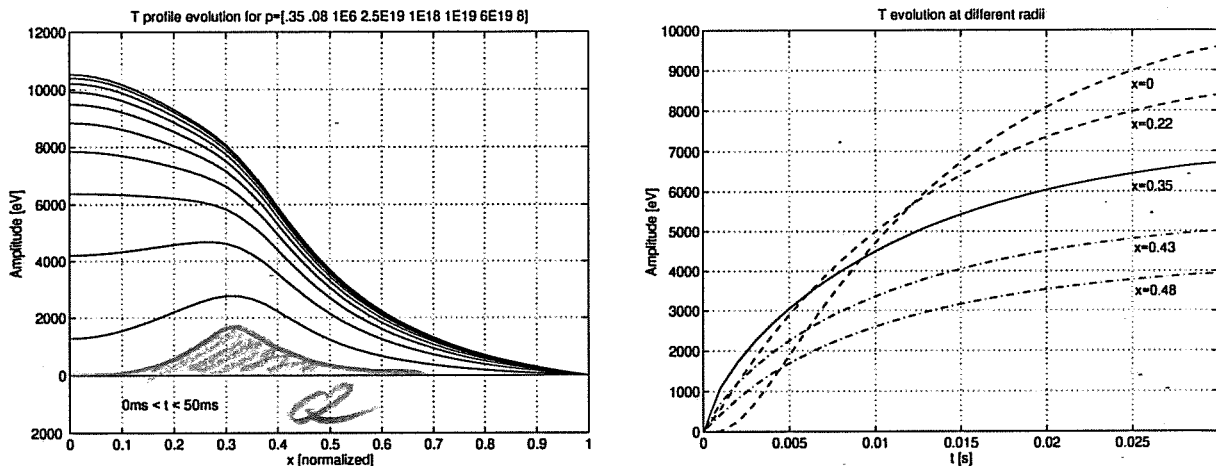


Figure III.5a/b: (a) shows the radial profile evolution (each curve corresponds to a different moment in time); (b) shows the evolution at different radii (each curve stands for a different x).

Figure III.5a shows the temperature profile evolution as a function of the radius. The different curves are taken every 5ms starting from $t=0$ to $t=50$ ms. It is clearly visible how in the early stages of the temporal evolution, when diffusion and convection effects have not much influence, the curve shows a clear maximum in the region where the power is deposited. A better view of the first 10 ms is seen in Figure C.2a in appendix C: here the diffusion and convection effects on the temperature profile, as well as the clear maximum in the deposition region, are clearly visible (curves taken every 2ms). After 2 ms there are almost no effects yet, while after 4 ms they are already of a considerable magnitude. This fact has already been pointed out in section III.2.2 and is now confirmed. It is a very important characteristic of the system and it will be developed later in chapter VI, when modulated sources are treated.

Figure III.5b shows, instead, the temperature evolution at different locations as a function of time. The solid line represents $x = x_0$, where the external power is injected, the dashed line represents $x < x_0$, while the dashed-dotted line stand for $x > x_0$. In the beginning it is evident that T will be higher there, where the power is directly deposited, while later on (here after 5ms for places near the deposition region) the temperature will increase more rapidly towards the center due to diffusion and convection effects. After a certain time the lines will be constant, meaning that stationarity has been reached.

radial
 $\frac{\partial T}{\partial x}$
 20

Next step is to formalize the study of the problem.

conclusion of this chapter:
 power deposition profiles can be derived
 from dynamical experiment

IV. Formalization of the problem

Chapter III showed the path to the solution of the transport equation (III-3), leading to the complete definition of the temperature profile evolution, starting from a set of predefined parameters of the form (III-17). Hence, it is now possible to choose any set of inputs and to construct the temporal evolution. Values for different parameters in the following ranges have been studied:

$$x_0 \in [0,1], \quad \Delta x \in [0.01,0.50], \quad P_{in} \in [5 \cdot 10^5, 2 \cdot 10^6], \quad n_0 \in [5 \cdot 10^{18}, 5 \cdot 10^{19}]$$

$$n_a \in [5 \cdot 10^{17}, 1 \cdot 10^{18}], \quad n\chi_0 \in [10^{18}, 10^{20}], \quad n\chi_1 \in [10^{18}, 10^{20}], \quad v_0 \in [-15,15]$$

with the following units

$$[x_0] = [\Delta x] = 1, \quad [P_{in}] = W, \quad [n_0] = [n_a] = m^{-3}, \quad [n\chi_0] = [n\chi_1] = m^{-1}s^{-1}, \quad [v_0] = ms^{-1}$$

IV.1 Idea and development: the J2 matrix

As already mentioned, it is unthinkable to try to extrapolate information by simply working directly with input parameters and relative output profile evolutions. A formalization of the problem is needed.

The idea for the formalization is the following: since we are interested in the behaviour of the temperature profile with respect to the input changes (and, in particular, to the changes of the two localization parameters x_0 and Δx), it is convenient to choose a fixed point p_0 (as done in section III.2.1) and to study the variations of the function $T(p)$ around the reference temperature profile $T(p_0)$. The studied function is therefore

$$J(p) = \sum_{x,t} [T_0 - T]^2 \quad \text{or better} \quad \langle (T_0 - T)^2 \rangle_{x,t} \quad (IV-1)$$

where $T_0 = T(p_0)$ (reference), $T = T(p) = T(p_0 + dp)$ (varied)

J is then a function of eight variables and can be approximated through an expansion in its derivatives:

specific limites, en part

$$J(p) \approx J(p_0 + dp) \approx J(p_0) + dp \cdot \left. \frac{\partial J}{\partial p} \right|_{p_0} + \frac{1}{2} dp^2 \left. \frac{\partial^2 J}{\partial p^2} \right|_{p_0} \quad (IV-2)$$

Since $J(p_0) = 0$ and $\left. \frac{\partial J}{\partial p} \right|_{p_0} = 0$, (IV-2) reduces to the simple quadratic form

$$J(p) \approx \frac{1}{2} dp^2 \left. \frac{\partial^2 J}{\partial p^2} \right|_{p_0} \equiv \frac{1}{2} dp^T \cdot J2 \cdot dp \quad (IV-3)$$

where $J2 = \frac{\partial^2 J}{\partial p^2} = \frac{\partial^2 J}{\partial p_i \partial p_j}$, $p_{i,j} \in [x_0, \Delta x, P_{in}, n_0, n_a, n\chi_0, n\chi_1, v_0]$, is the matrix of the

second derivative of J . A representation of the considered situation is sketched in the following figure:

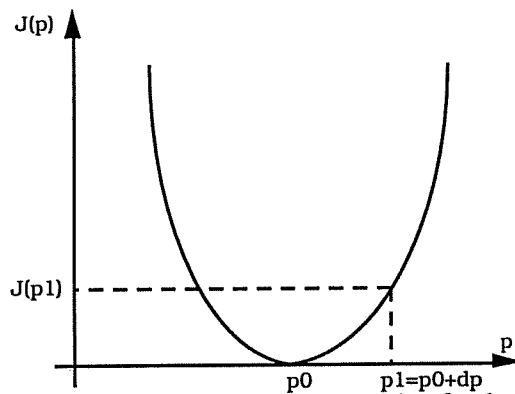


Figure IV.1: representation of the idea for the approximation of J leading to $J2$.

The function J is approximated around the reference point p_0 through its second derivative $J2$. It is this matrix $J2$ that will provide the information we are interested in, concerning the possibility of a localization of power deposition (the inverse problem): once normalized¹, $J2$ will clarify how sharp the function J is around p_0 . In particular, *expl.* an eigenmode-eigenvalue decomposition of the second derivative matrix will give information on the direction and magnitude of the axis of the eight dimensional ellipsoid, that J represents, with p_0 as its center.

$J2$ is built on the basis of²:

$$J(\underline{p}_0 + \underline{dp}_i + \underline{dp}_j) = \frac{1}{2} \left(dp_i^2 \frac{\partial^2 J}{\partial p_i^2} + 2 dp_i dp_j \frac{\partial^2 J}{\partial p_i \partial p_j} + \frac{\partial^2 J}{\partial p_j^2} dp_j^2 \right) \quad (IV-4)$$

relation per pucise

¹For the normalization see Appendix D

²Algorithm deriv.m (Matlab 4.2c)

The coefficients $\frac{\partial^2 J}{\partial p_i^2}$ and $\frac{\partial^2 J}{\partial p_i \partial p_j}$ of J_2 can be easily calculated considering that $J(p_0 + dp_i + dp_j)$ can be evaluated.

IV.2 Application of J_2

As the reference starting point p_0 , the following set of parameters has been chosen:

$$x_0 = 0.35, \Delta x = 0.08, P_m = 10^6 \text{ W}, n_0 = 2.5 \cdot 10^{19} \text{ m}^{-3}$$

$$n_a = 10^{18} \text{ m}^{-3}, n\chi_0 = 10^{19} \text{ m}^{-1}\text{s}^{-1}, n\chi_1 = 6 \cdot 10^{19} \text{ m}^{-1}\text{s}^{-1}, v_0 = 8 \text{ ms}^{-1}$$

The normalized second derivative matrix J_2 evaluated in p_0 gives

$$J_2 = \begin{pmatrix} 8.20 \cdot 10^8 & 9.65 \cdot 10^7 & 0 & 0 & 0 & 0 & 0 & -3.02 \cdot 10^6 \\ 9.65 \cdot 10^7 & 2.31 \cdot 10^7 & 0 & 0 & 0 & 0 & 0 & -3.50 \cdot 10^5 \\ 0 & 0 & 0 & 0 & 0 & 0 & 0 & 0 \\ 0 & 0 & 0 & 0 & 0 & 0 & 0 & 0 \\ 0 & 0 & 0 & 0 & 0 & 0 & 0 & 0 \\ 0 & 0 & 0 & 0 & 0 & 0 & 0 & 0 \\ 0 & 0 & 0 & 0 & 0 & 0 & 0 & 0 \\ -3.02 \cdot 10^6 & -3.50 \cdot 10^5 & 0 & 0 & 0 & 0 & 0 & 1.16 \cdot 10^4 \end{pmatrix} \quad (\text{IV-5})$$

*matrix can
write again
is symmetric*

The matrix coefficients shown as zero are not exactly zero, but are very small compared to the written values, which are completely dominant. Looking only at J_2 , it is not possible to have a clear understanding of which parameters have the strongest influence on J , we therefore make an eigenmode-eigenvalue decomposition such that $J_2 = V \cdot D \cdot V^{-1}$. D and V are then

$$D = \begin{pmatrix} 8 \cdot 10^8 & & & & & & & \\ & 1 \cdot 10^7 & & & & & & \\ & & 4 \cdot 10^2 & & & & & \\ & & & 10^{-14} & & & & \\ & & & & 10^{-71} & & & \\ & & & & & 10^{-72} & & \\ & & & & & & 10^{-74} & \\ & & & & & & & 0 \end{pmatrix} \quad (\text{IV-6})$$

$$V = \begin{pmatrix} 0.99 & 0.12 & & & & & & \\ 0.12 & -0.99 & & & & & & \\ & & -1.00 & & & & & \\ & & & & 1.00 & & & \\ & & & -0.31 & -0.42 & -0.85 & & \\ & & & 0.82 & -0.58 & -0.01 & & \\ & & & 0.49 & 0.70 & -0.52 & & \\ & & & & & & & -1.00 \end{pmatrix} \quad (IV-7)$$

Each column of V represents one eigenvector of J2 corresponding to the respective eigenvalue in D.

These forms of D and V show up some interesting particularities: first of all, it is clear from the different magnitudes of the eigenvalues in D, that the first three have a larger predominance on all others, which have magnitudes comparable to zero with respect to the first three. Furthermore, V fixes the directions of the main axes of the ellipsoid for the variations of mainly three of the parameters: x_0 , Δx and v_0 . This particular result is already noteworthy, because of the fact that two of the major axes are in the direction of the two parameters in which we are particularly interested. This simply means that any small change in x_0 or Δx produces a greater change in J than any other comparable variation of the other parameters, except the convection term v_0 . The large eigenvalue in the direction of the convection change, though, makes things worse for the localization.

IV.3 Quantification of the variations

It is now possible, with the aid of the second derivative matrix J2, to quantify the changes of J varying two of the eight parameters involved. Making use of J2, it is possible to calculate the matrix³

$$F_{ij} = \frac{1}{2} dp_a(i)^+ * J2 * dp_b(j) \quad (IV-8)$$

where $dp_a(i) \equiv i \cdot dp(a)$, $dp_b(j) \equiv j \cdot dp(b)$ and dp is the "unit"-vector of the parameter variation.

why if normalise ✓

Figure IV.2 plots the contour graph of $F(dp_{x_0}, dp_{\Delta x})$, that means, the behaviour of J varying the parameters of the localization.

(simply J((x0, dx; other fixed)))

³Algorithm lev_norm.m (Matlab 4.2c)

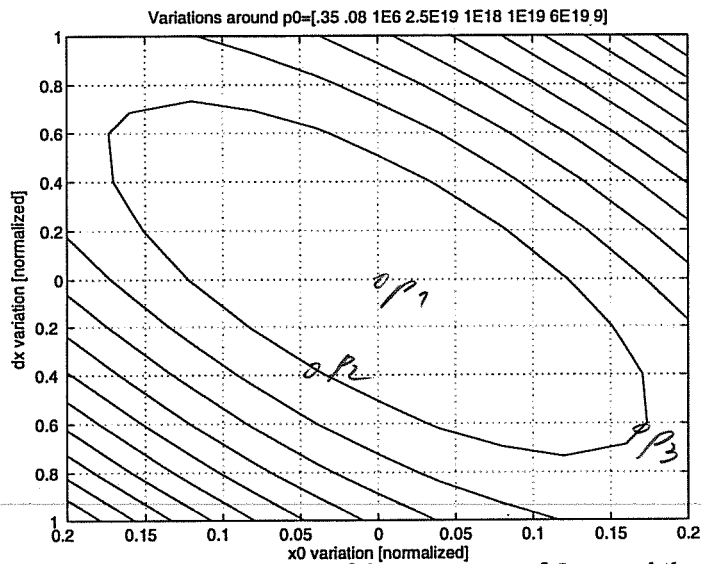


Figure IV.2: contour plot of the variations of J around the chosen working point.

Calculating J_2 and F directly from a given p_0 and plotting this final result like in figure IV.4, gives an idea of how sharp the $T(p)$ function is around its power deposition coordinates x_0 and Δx .

Similar calculations and plots can be done using variations of the other parameters too.

V. Analysis of temperature profiles

Having formalized the problem as presented in chapter IV, all the tools for further investigation of the studied problem are now available. As a fix starting reference point, the following set of parameters has been chosen:

$$\begin{aligned} p_0 &= [r_0 \text{ [m]}, \Delta r \text{ [m]}, P_{in} \text{ [W]}, n_0 \text{ [m}^{-3}\text{]}, n_a \text{ [m}^{-3}\text{]}, \\ & n\chi_0 \text{ [m}^{-1}\text{s}^{-1}\text{]}, n\chi_1 \text{ [m}^{-1}\text{s}^{-1}\text{]}, v_0 \text{ [ms}^{-1}\text{]}] = \quad (V-1) \\ &= [0.35, 0.08, 10^6, 2.5 \cdot 10^{19}, 10^{18}, 10^{19}, 6 \cdot 10^{19}, 8] \end{aligned}$$

V.1 Stationary temperature profile

It is convenient to investigate the stationary case first, not only because, in a perspective view, it will be the normal working situation of a thermonuclear reactor, but also because, as we will see, it will point out a first important result that will influence the course of the analysis.

Using the method developed in section IV.3 and taking advantage of the information contained in figure IV.2, it is possible to find several sets of $(x_{0_1}, \Delta x_1)$, laying on one of the ellipsoids, which lead to stationary temperature profiles differentiating from the reference one by the magnitude specified by matrix F, which is nothing else but the generatrix of the ellipsoids. Following this idea, two sets are chosen,

$$\begin{aligned} p_1 &\leftrightarrow (x_{0_1}, \Delta x_1) = (0.20, 0.30) \\ p_2 &\leftrightarrow (x_{0_2}, \Delta x_2) = (0.43, 0.25) \end{aligned}$$

the other parameters of p_0 remaining unchanged.

Putting these new parameters in the algorithm extrapolating the temperature profile, the following graph comes out:

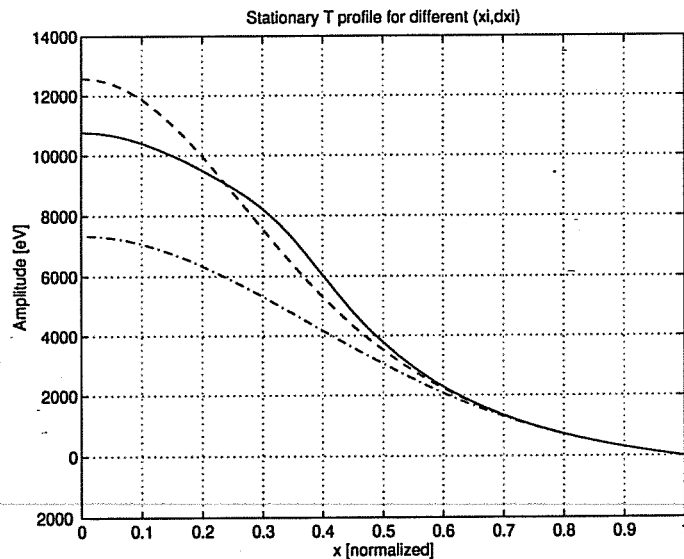


Figure V.1: stationary T profile for starting parameters p_0 (solid line), p_1 (dashed line) and p_2 (dashed-dotted line).

The solid line corresponds to the reference stationary profile, while the dashed and dashed-dotted lines show the heating centered at 0.20 and 0.43 respectively.

Now, taking advantage of the information that the D and V matrices evaluated in p_0 offer, it is possible to change the other parameters in such a way, that the two modified profiles again approach the reference. Setting the following parameters

$$p_1 = [0.20, 0.30, 10^6 \text{ W}, 2.5 \cdot 10^{19} \text{ m}^{-3}, 10^{18} \text{ m}^{-3}, 10^{19} \text{ m}^{-1}\text{s}^{-1}, 4.3 \cdot 10^{19} \text{ m}^{-1}\text{s}^{-1}, 2.5 \text{ ms}^{-1}]$$

$$p_2 = [0.43, 0.25, 10^6 \text{ W}, 2.5 \cdot 10^{19} \text{ m}^{-3}, 10^{18} \text{ m}^{-3}, 10^{19} \text{ m}^{-1}\text{s}^{-1}, 5.2 \cdot 10^{19} \text{ m}^{-1}\text{s}^{-1}, 12.0 \text{ ms}^{-1}]$$

note that the same power is used only transport model is varied V

the next graph can be drawn:

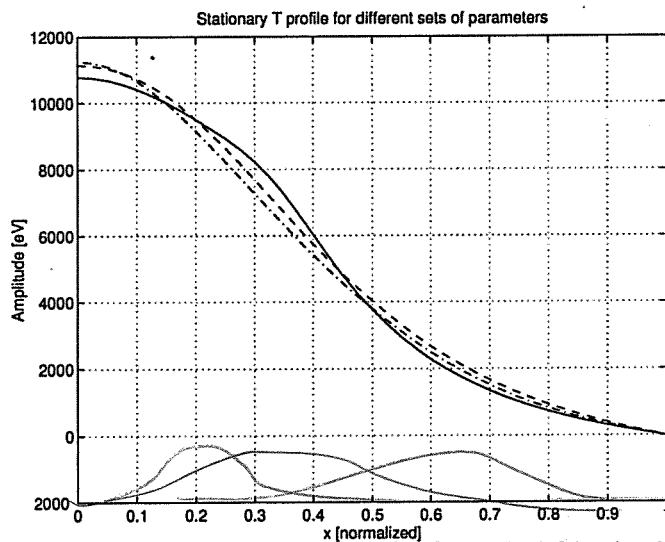


Figure V.2: stationary T profile for p_0 (solid line), p_1 (dashed) and p_2 (dashed-dotted).

Calculating a normalized variance between the profiles resulting from the modified parameters and the reference results in:

$$\sigma_{P_0P_1}^2 = \frac{\sum_x (T_{st}(P_0) - T_{st}(P_1))^2}{\sum_x T_{st}(P_0)^2} = 0.0026$$

$$\sigma_{P_0P_2}^2 = \frac{\sum_x (T_{st}(P_0) - T_{st}(P_2))^2}{\sum_x T_{st}(P_0)^2} = 0.0052$$

leading to an average difference of less than 1% for both cases.

The meaning of this result is clear: it was possible to find three sets of parameters with completely different x_0 and Δx leading, within the resolution capabilities (sawtooth oscillation of the X-ray emission, MHD instabilities), to the same stationary temperature profile. The only other parameters that were changed in order to reach this result were the two unknown coefficients of diffusion and convection. The density parameters were not touched, because the density profile is essentially measurable. In other words, this first result puts the following facts into evidence: it has been demonstrated that, in principle, starting from a measured stationary temperature profile, it is not possible to reconstruct the original set of parameters that generated it, because the three profiles found are not completely separable due to the amount of noise on them and because there are no information about diffusion and convection coefficients (being experimentally directly not measurable), meaning that these have to be left free to vary.

The simple straight application of a fitting algorithm to the reproduction of the generating parameters, starting from a measured stationary temperature profile, could then lead to the wrong parameters, and is therefore a dangerous procedure. Additional information is required, which can be gained by looking at the complete temporal evolution of the temperature profile.

V.2 Temporal evolution

As already mentioned in the previous chapters, if the early stages of the heating are studied, the temperature's curve shows a clear maximum where the energy is directly deposited, suffering then later on, as time t increases, from a smoothing out of the profile due to the influence of diffusion and convection. It is then reasonable to think that, in these early stages, the profiles related to the above defined sets of parameters are more separated, due to the fact that their power deposition regions differ from one another. Looking at figure III.5 it is convenient to study the rising of

the profiles during the first 50 ms. Figure V.3a/b/c show the above mentioned temperature profiles evolution for our three sets of parameters (profiles taken every 5 ms).

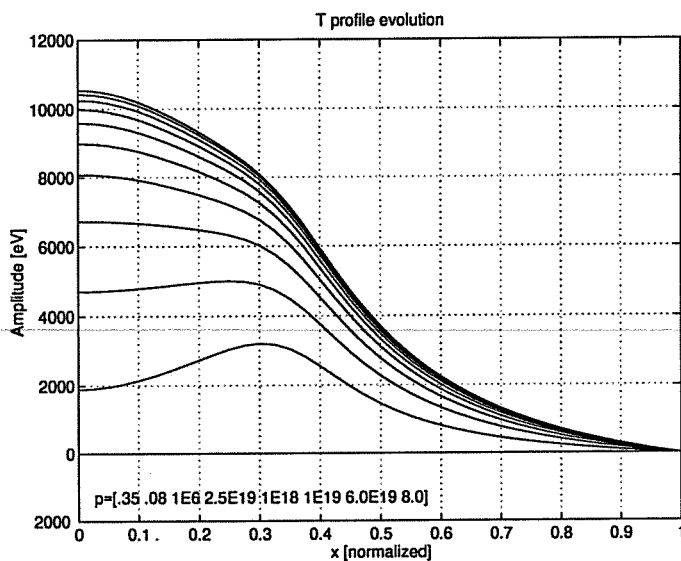


Figure V.3a: *T* profile evolution calculated from the reference set of parameters p_0 .

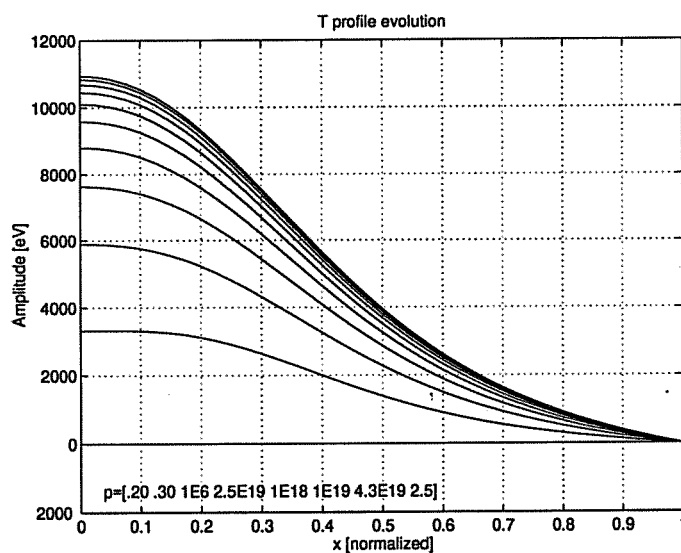


Figure V.3b: *T* profile evolution calculated from the deviated set p_1 .

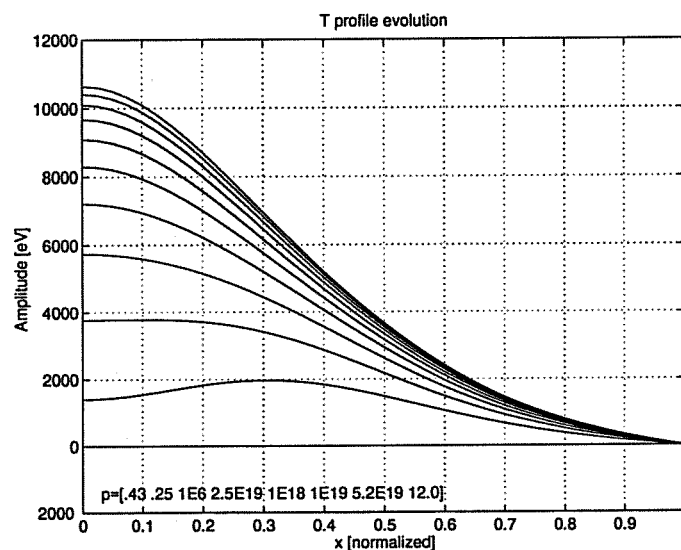


Figure V.3c: *T* profile evolution calculated from the deviated set p_2 .

Looking at these figures it is already visible how the profiles are very different for small t 's, and how diffusion and convection change the profiles heading to the three almost identical stationary curves of the three parameters. Concentrating our view on the first 5 ms of the evolution we can see the situation even more clearly. Figure V.4 displays this.

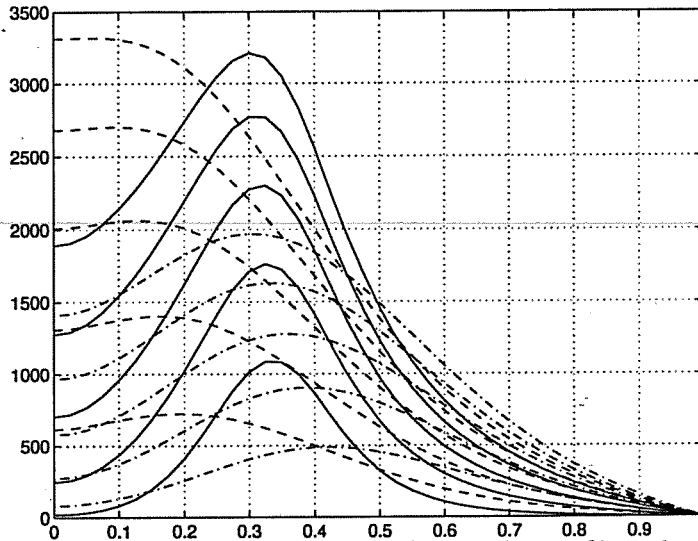


Figure V.4: time evolution of the radial profiles related to the three sets of parameters taken into consideration. x -axis: time [s]; y -axis: amplitude [eV].

For this graph, the profiles were drawn every 2 ms. The solid line represents the evolution of the reference parameter p_0 , while the dashed and the dashed-dotted lines the sets centered at $x_0 = 0.20$ and $x_0 = 0.43$ respectively.

For practical reasons, the set of parameters p_2 will now be put aside, and the two left will be further investigated. Everything pointed out for those, can then be extended to the third one.

V.3 Early stages of the evolution

In order to gain better information on the time interval during which the difference between the two profiles is greater, it is convenient to analyze the temporal evolution of the gap that separates them. Figure V.5 shows this evolution, restricted to the first 100 ms, plotting the "Gap-Function"

$$J(t) = \sum_x (T(p_0) - T(p_1))^2 \quad (V-2)$$

that gives the square-difference at each time point.

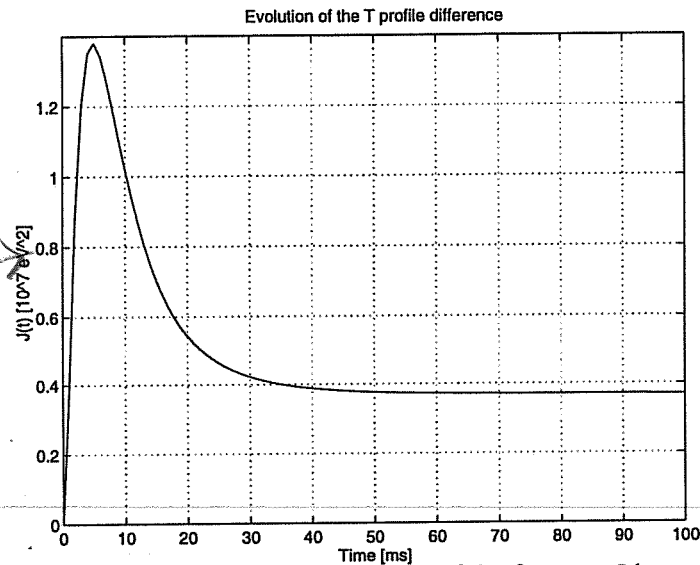


Figure V.5: temporal evolution of the function J (square difference between the two profiles).

All the remarks made above are now clearly visible in this figure: at $t \approx 5$ ms the function J is about three times larger than for $t \rightarrow \infty$, the stationary case. Calculating the normalized variance between the two profiles at $t=5$ ms of the evolution, we obtain

$$\sigma_{P_0 P_1}^2 = \frac{\sum_x (T_{t^*}(p_0) - T_{t^*}(p_1))^2}{\sum_x T_{t^*}(p_0)^2} = 0.1025$$

leading to an average difference between the two profiles in the range of 5%.

Comparing this result with the one for the stationary profiles, we can see that the square deviation grows by a factor of about 40, leading to the above noted average difference.

It is now evident what the next step will be: since our goal is the separation of the two profiles, in order to reach this we need to "force" the two curves into the region of figure V.5, where the difference between them is the largest, and we must keep them in there. To achieve this, it is therefore necessary to modulate the external power injection in such a way, that this difference is maximized. The tool that will provide the information about the improvement or the worsening of the situation, is the J2 matrix developed in chapter IV.

Before doing this, it is necessary to investigate in more detail the behaviour of J2 (and therefore of the temperature profile) for several values of $n\chi_1/n\chi_0$ and av_0/χ_0 . The reason why this is necessary, is that, a priori, we do not know if the influence of diffusion and convection are similar for different values of the above mentioned ratios.

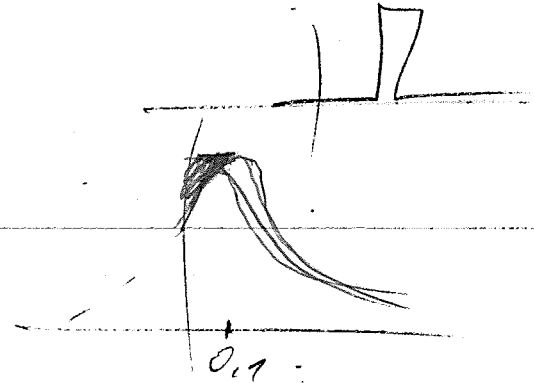
V.4 Investigation of J2

Hence, only looking at the transport equation, it is not possible to exclude a different and maybe strange behaviour of the temperature profile for different ratios of $n\chi_1/n\chi_0$ or av_0/χ_0 . In order to gain the information needed not only for one particular case (p_0), but in general, the different ratios will be studied at three different locations: $x_{01} = 0$, $x_{02} = 0.40$ and $x_{03} = 0.80$.

V.4.1 Heating in the center

As reference starting point, the set of parameters

$$p_1 = [0, 0.10, 10^6, 10^{19}, 10^{18}, 10^{19}, 10^{18}, 0]$$



was chosen, leading to the following D (eigenvalues) and V (eigenvectors) matrices:

$D_1 =$

$7.5 \cdot 10^9$									
	$7.8 \cdot 10^6$								
		$1.6 \cdot 10^4$							
			10^{-14}						
				10^{-68}					
					10^{-70}				
						10^{-72}			
							0		

$V_1 =$

0.50	0.87								
0.87	-0.50								
		1.00							
			-1.00						
				-0.02	0.16	0.99			
				0.19	-0.97	0.16			
				-0.98	-0.19	0.01			
							-1.00		

The main characteristics of these matrices are the same as for the case calculated in section IV.2 for the other set: a predominance of the first three eigenvalues related to the two coordinates and to the convection term. D and V have then been calculated for the following ratios:

$$\frac{n\chi_1}{n\chi_0} = 0, 0.1, 0.5, 1, 5, 10$$

$$\frac{av_0}{\chi_0} = -2.5, -1.25, -0.5, 0, 0.5, 1.25, 2.5$$

Appendix Ea shows a few of those matrices. From all the calculated matrices, no evidence comes out indicating any significant change in the behaviour of the temperature profile around each of the varied points.

V.4.2 Heating half way to the edge

As reference starting point we choose

$$p_2 = [0.40, 0.10, 10^6 \text{ W}, 10^{19} \text{ m}^{-3}, 10^{18} \text{ m}^{-3}, 10^{19} \text{ m}^{-1}\text{s}^{-1}, 10^{18} \text{ m}^{-1}\text{s}^{-1}, 0 \text{ ms}^{-1}]$$

leading to

$$D_2 = \begin{bmatrix} 1.4 \cdot 10^9 & & & & & & & & \\ & 2.9 \cdot 10^7 & & & & & & & \\ & & 1.6 \cdot 10^3 & & & & & & \\ & & & 10^{-14} & & & & & \\ & & & & 10^{-70} & & & & \\ & & & & & 10^{-71} & & & \\ & & & & & & 10^{-73} & & \\ & & & & & & & 0 & \end{bmatrix}$$

$$V_2 = \begin{bmatrix} 0.98 & 0.20 & & & & & & & \\ 0.20 & -0.98 & & & & & & & \\ & & -1.00 & & & & & & \\ & & & & & & & & 1.00 \\ & & & & -0.20 & -0.01 & -0.98 & & \\ & & & & 0.82 & -0.55 & -0.16 & & \\ & & & & 0.53 & 0.84 & -0.12 & & \\ & & & -1.00 & & & & & \end{bmatrix}$$

Appendix Eb shows, as before, a few matrices with the varied ratios. Also in this case no significant change has been observed.

V.4.3 Heating far from the center

The chosen starting point was chosen to be

$$p_3 = [0.80, 0.10, 10^6 \text{ W}, 10^{19} \text{ m}^{-3}, 10^{18} \text{ m}^{-3}, 10^{19} \text{ m}^{-1}\text{s}^{-1}, 10^{18} \text{ m}^{-1}\text{s}^{-1}, 0 \text{ ms}^{-1}]$$

leading to

$$D_3 = \begin{bmatrix} 6.4 \cdot 10^8 & & & & & & & & \\ & 7.2 \cdot 10^6 & & & & & & & \\ & & 4.7 \cdot 10^2 & & & & & & \\ & & & 10^{-16} & & & & & \\ & & & & 10^{-71} & & & & \\ & & & & & 10^{-73} & & & \\ & & & & & & 10^{-74} & & \\ & & & & & & & 0 & \end{bmatrix}$$

$$V_3 = \begin{bmatrix} 0.99 & 0.05 & & & & & & & \\ 0.05 & -0.99 & & & & & & & \\ & & 1.00 & & & & & & \\ & & & -0.32 & -0.23 & -0.92 & & & \\ & & & 0.85 & -0.50 & -0.17 & & & \\ & & & 0.42 & 0.83 & -0.35 & & & \\ & & -1.00 & & & & & & \\ & & & & & & & -1.00 & \end{bmatrix}$$

Appendix Ec shows, again, a few matrices with the varied ratios.

In this case too, no significant change has been observed.

note that for $\chi_0 \rightarrow \chi_0$ and dk are correlated

V.4.4 Remarks on the calculated matrices

The very important result coming out from the study developed above, is that the behaviour of the J2 matrix does not depend on the coordinate of the deposition, nor on the different values of proportionality for diffusion and convection terms. This is important, because it allows us to generalize the results gained from the investigation of one particular chosen case. The first three eigenvalues of D remain dominant in each case studied. There are, though, a few changes in the ratios between them: for example, increasing the value of $n\chi_1/n\chi_0$ (holding av_0/χ_0 constant) induces a reduction of the eigenvalue related to the convection eigenvector, meaning that, for stronger diffusion, the convection effects become smaller. The same effect, but less

significant, is produced, if the starting convection coefficient is larger: the higher v_0 , the smaller will be the changes of J_2 due to variations of v_0 itself.

Another remark that can be made is related to the different relationships between the eigenvalues depending on the choice of x_0 .

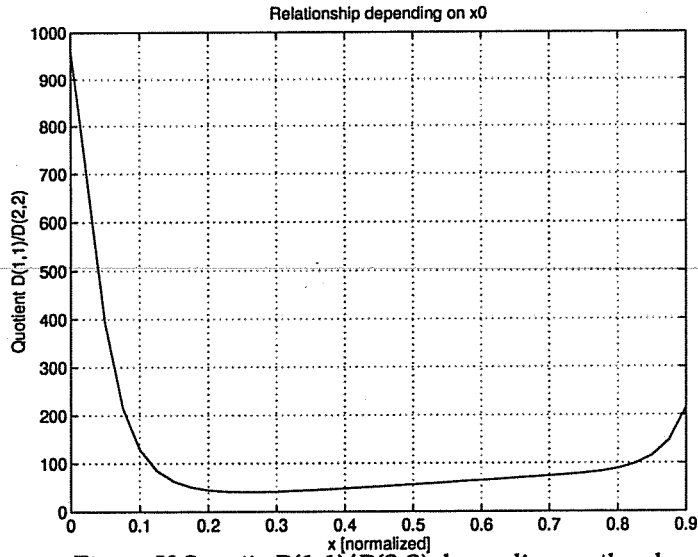


Figure V.6: ratio $D(1,1)/D(2,2)$ depending on the chosen x_0 .

Figure V.6 shows the ratio between the first and second eigenvalues of the D matrix depending on the starting value of x_0 . With the heating centered around $x_0=0$, the eigenvalue of the $\Delta(x_0)$ eigenvector exceeds the one of the $\Delta(\Delta x)$ by several hundreds, while after a certain point (about 0.10) it becomes almost constant significantly below 100. This means that, in principle, a localization of power deposition is easier if heated near the center, while it gets harder in the outer regions, due to the fact that x_0 and Δx become more related to each other. Diffusion and convection are the reason for this situation: their effect acts in such a way that heat is transported from the direct deposition region towards the center. Since in the case of central deposition these two places coincide, diffusion and convection effects become smaller and a better localization is therefore possible.

Comparing the two first eigenvalues with the third one in the same way as above, the following graphs can be drawn:

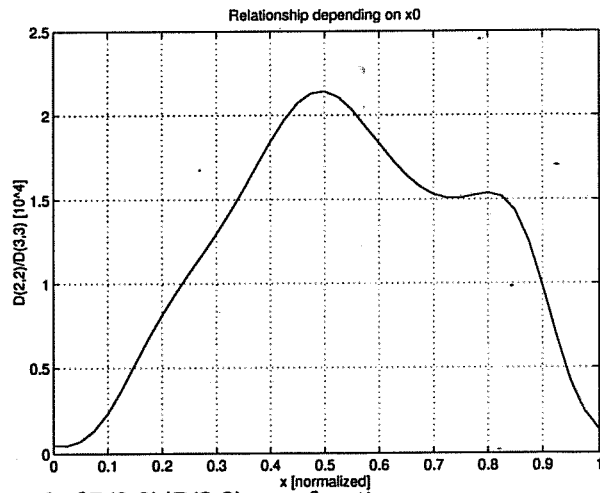
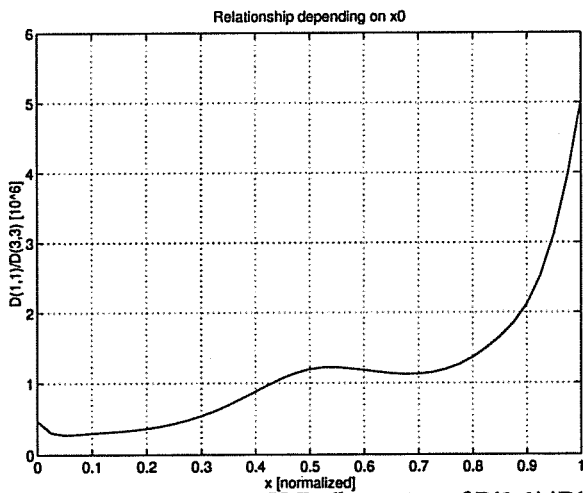


Figure V.7a/b: ratios of $D(1,1)/D(3,3)$ and of $D(2,2)/D(3,3)$ as a function of the starting value of x_0 .

Figure V.7a shows the relationship between the third and the first eigenvalues, figure V.7b between the third and the second. While in the first case (Figure V.7a) the curve remains pretty much constant, in the second (Figure V.7b) the curve shows a completely different form: between the center and $x=0.5$ there is a factor 35 difference, meaning that towards the center the second and third eigenvectors are more dependent on each other than for larger x 's. Since the ratios between them are in the order of $10^3 - 10^4$, though, this feature does not affect the conclusions in a significant way. It is interesting to note, though, that the two ratios show opposite behaviour.

Having now demonstrated that the main characteristics of the J2 matrix are not very much affected by different ratios between the diffusion and convection parameters, nor by different chosen x_0 's, we can now proceed with the next chapter: the treatment of the problem with modulated sources.

so what the 3rd eigen vector is kind of
 correction. Does it help understanding?

$\frac{\partial F}{\partial t} = Dg + Q$

$g = -\frac{\partial^2 \psi}{\partial x^2} - \frac{\partial \psi}{\partial t} \quad v < 0$

$P = -D \nabla^2 \psi + v \psi$

VI. Modulation of the source

The two profiles we are trying to separate from each other are those related to the following sets of parameters:

$$p_1 = [0.35, 0.08, 10^6 \text{ W}, 2.5 \cdot 10^{19} \text{ m}^{-3}, 10^{18} \text{ m}^{-3}, 10^{19} \text{ m}^{-1}\text{s}^{-1}, 6 \cdot 10^{19} \text{ m}^{-1}\text{s}^{-1}, 8 \text{ ms}^{-1}]$$
$$p_2 = [0.20, 0.30, 10^6 \text{ W}, 2.5 \cdot 10^{19} \text{ m}^{-3}, 10^{18} \text{ m}^{-3}, 10^{19} \text{ m}^{-1}\text{s}^{-1}, 4.2 \cdot 10^{19} \text{ m}^{-1}\text{s}^{-1}, 2.5 \text{ ms}^{-1}]$$

Figures V.3a/b show their temporal evolution for the first 50 ms after the turning on of the additional heating.

We now need to find the best possible modulation keeping the two temperature profiles in the regions where they are most apart from each other. Before doing this, for completeness, we will take up the non modulated case.

VI.1 The non modulated case

For the purpose of this chapter, the evolution of the temperature profiles during 0.5 s has been studied.

Considering the evolution of the temperature for different radii, it is convenient to draw the following graph:

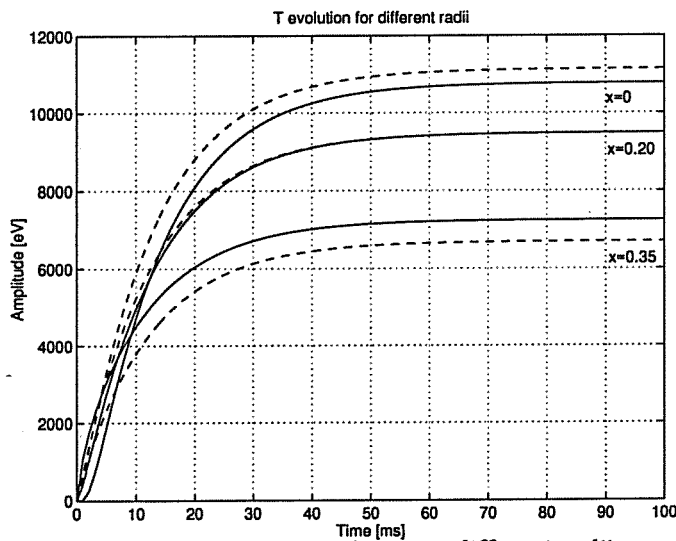


Figure VI.1: temperature evolution at different radii.

Figure VI.1 shows the evolution of T at x=0, x=0.20 and x=0.35. The solid line represents p₁, while the dashed line p₂. The evolution reaches stationarity quickly:

after 100 ms, T remains constant for the remaining 400 ms, but the changes are very small already after 40 ms. The strongest time dependences lay in the first 40 ms of heating, and this for both profiles.

Another way to gain the information about this so called "rising time", is to study the square difference evolution of the two profiles¹:

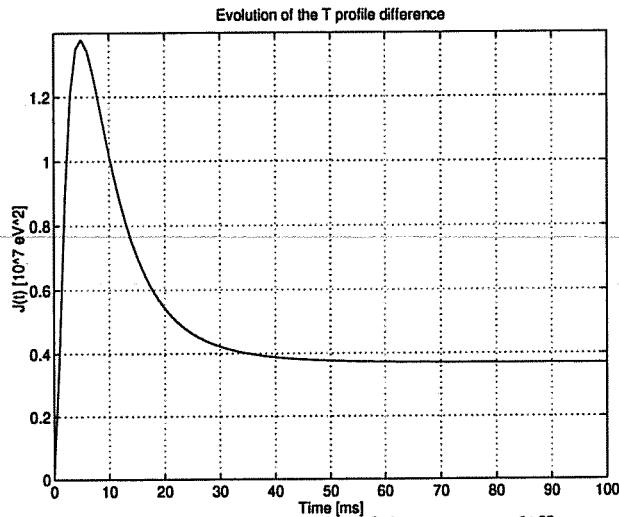


Figure VI.2: time evolution of the square difference between the two profiles.

Figure VI.2 recalls Figure V.5 , showing the above mentioned curve. When looking for the best modulation, this graph will become important, because it points out a first guess for the modulation frequency, and because it will show its effects on the differences between the profiles.

Before starting with modulated sources, the normalized variance, the three main eigenvalues of J2 (evaluated in p₁) and their relative ratios are reported:

$$\sigma_1^2 = \frac{\sum_{x,t} (T(p_1) - T(p_2))^2}{\sum_{x,t} T(p_1)^2} = 0.0026 \quad (\text{VI-1})$$

$$D_1 = 8.31 \cdot 10^8, D_2 = 1.15 \cdot 10^7, D_3 = 4.06 \cdot 10^2$$

$$\frac{D_1}{D_2} = 72, \frac{D_2}{D_3} = 2.8 \cdot 10^4 \quad (\text{VI-2})$$

¹See section V.3

VI.2 Sinusoidal modulation

The first attempt to try to improve the separation between the two profiles, is to modulate the external power injection with a sinusoidal signal. This means that for our calculations $U(t)$ in (III-16) takes the form

$$U(t) = \frac{1}{2} + \frac{1}{2} \cdot \sin(\omega t) \quad \text{where} \quad \omega = 2\pi f \quad (\text{VI-3})$$

In order to maximize the possible gain derived from this modulation, we need to find an appropriate frequency. The chosen frequency will have to maximize the functional

$$J^2 = \sum_{x,t} (T(p_1) - T(p_2))^2 \quad (\text{VI-4})$$

Plotting (VI-3) as a function of the frequency, we obtain

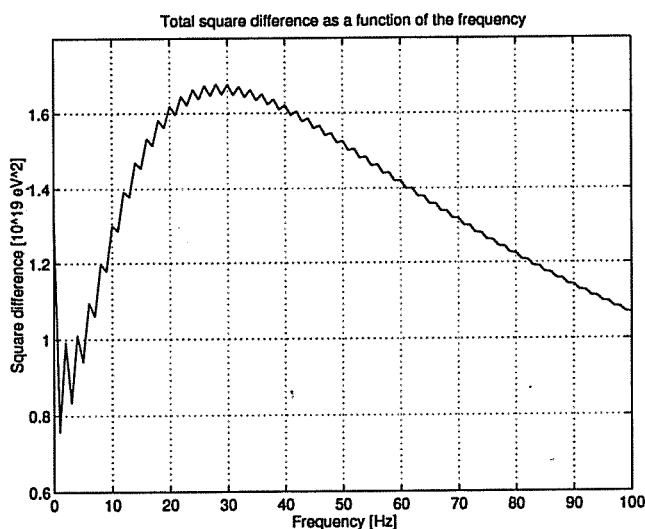
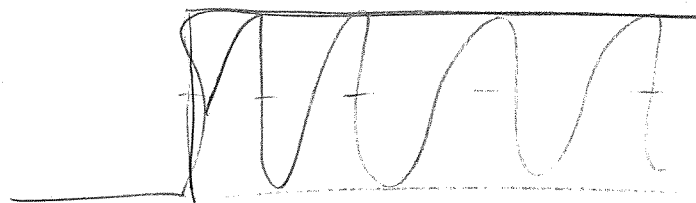


Figure VI.3: total square difference between the two profiles as a function of the modulating frequency.

From this figure, the optimal frequency $f = 30\text{Hz}$ is derived. Modulating the external power source with this f we get:



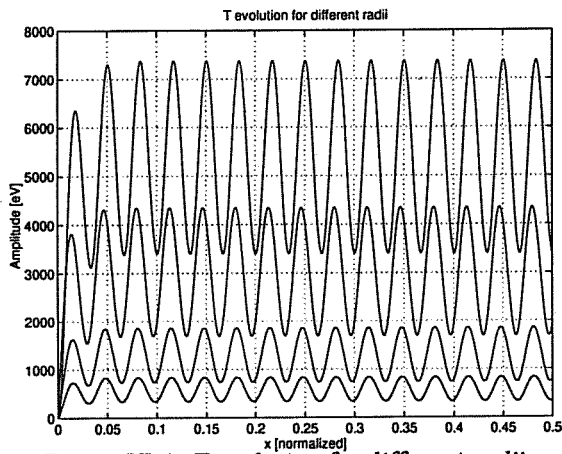


Figure VI.4: T evolution for different radii.

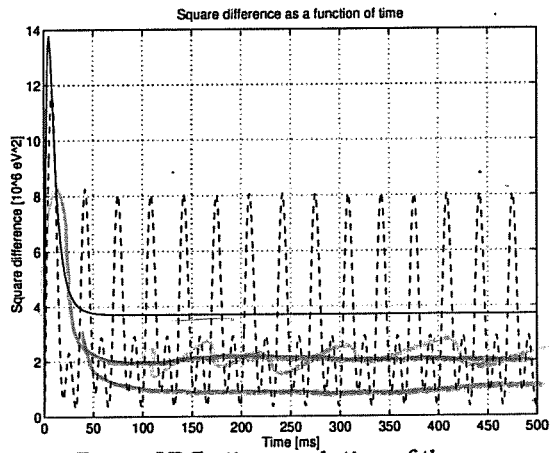


Figure VI.5: time evolution of the square difference between the profiles.

Figure VI.4 plots the temperature evolution at different locations, showing clearly the modulation of the external power exerting its influence on the time dependence of T. Figure VI.5 shows the square difference of the two modulated temperature profiles as a function of time compared to the previous square difference for the non modulated case. There where, for the non modulated case, the curve is constant (solid line), the new obtained curve (dashed line) shows bigger differences during well defined time intervals. However, as the elapsed time grows, the total square difference is larger for the non modulated case (see figure VI.6).

Comparison should be done at same power level. It's hard for us to compare

*U(t) = 1/2
 => T -> T/2
 => J -> J/4*

*<> must be better because
 J -> de
 F t -> 100*

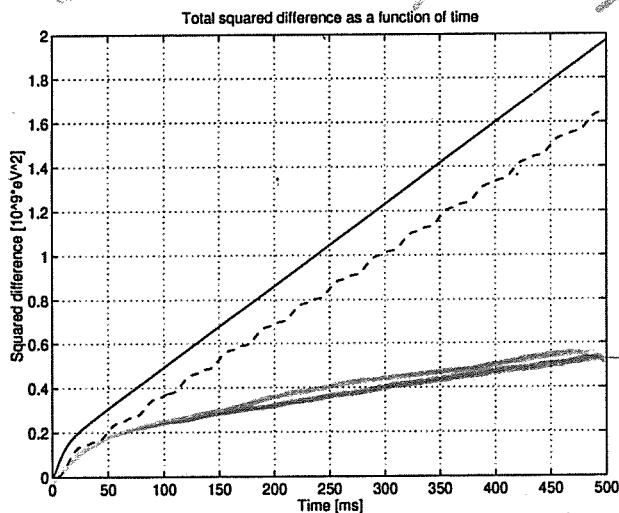


Figure VI.6: total square difference between the two profiles as a function of time.

If the normalized variance is calculated, though, we obtain

$$\sigma_2^2 = \frac{\sum_{x,t} (T(p_1) - T(p_2))^2}{\sum_{x,t} T(p_1)^2} = 0.0079 \quad (VI-5)$$

showing that, even if the total square difference between the two profiles is smaller, the standard deviation increases, meaning that the two profiles are actually better

separated. Calculating the eigenvalues of J_2 and their relative ratios gives confirmation of the improvement:

$$D_1 = 2.37 \cdot 10^8, D_2 = 4.43 \cdot 10^6, D_3 = 3.59 \cdot 10^2$$

$$\frac{D_1}{D_2} = 53, \frac{D_2}{D_3} = 1.2 \cdot 10^4 \quad (\text{VI-6})$$

The ratios pass from 72 to 53 and from $2.8 \cdot 10^4$ to $1.2 \cdot 10^4$ respectively. This means that the relationship between the x_0 and Δx parameters becomes closer, leading in principle to a better reconstruction potential. The improvement is in the order of a factor 3.0 (comparing the standard deviations).

VI.3 Modulation with Random Binary Signal

Our second try for the improvement, is the choice of Random Binary Signal (RBS) as the modulation signal for the external power injection. In this case $U(t)$ will be of the form

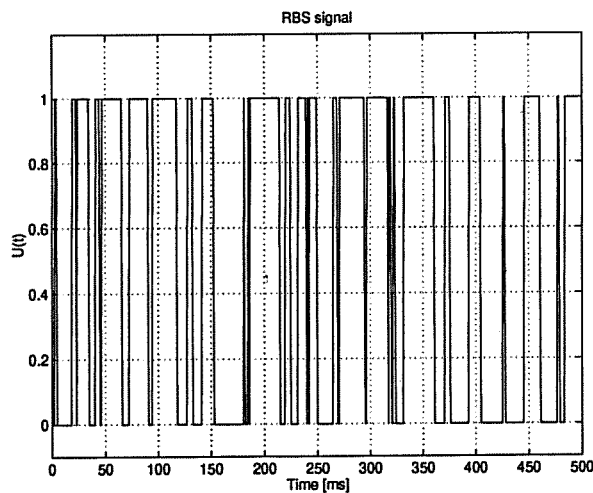
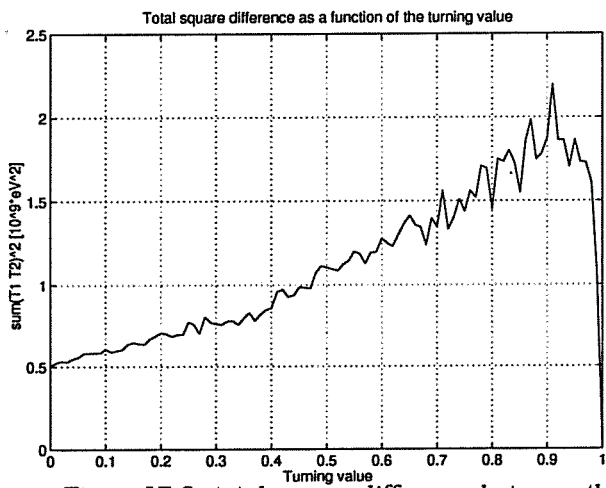


Figure VI.7: RBS signal.

Following the same idea as in the previous section, this time we have to find the best "turning value" defining RBS. This "turning value" is the number (between 0 and 1) that decides whether the generated random number of the algorithm will change the previous value of the function $U(t)$ or not.

more precisely:



This depends on the complex time

Figure VI.8: total square difference between the profiles as a function of the "turning value".

Figure VI.8 indicates that this best value has to be chosen as equal about 0.90. Modulating the external power source with this signal produces the following plots:

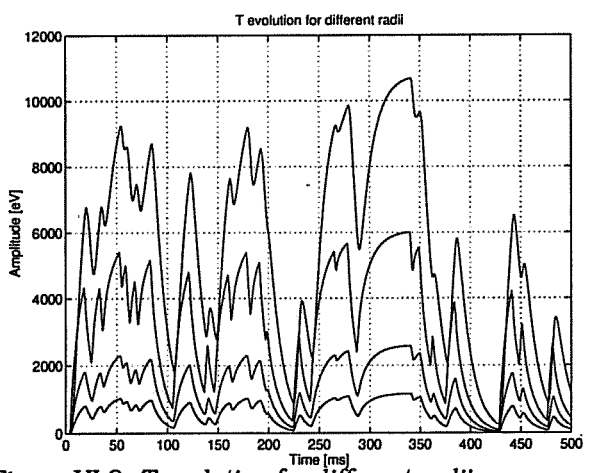


Figure VI.9: T evolution for different radii.

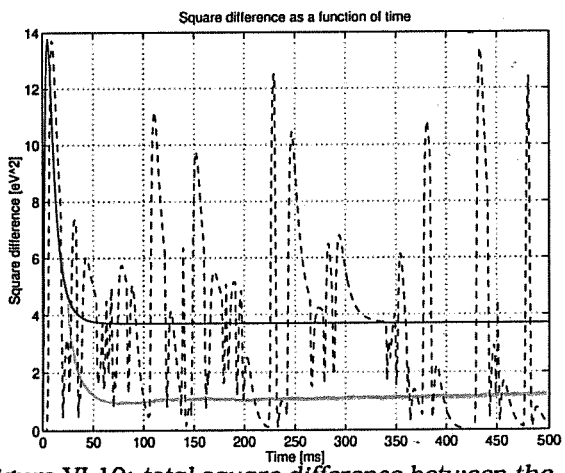


Figure VI.10: total square difference between the profiles as a function of time.

Figure VI.9 reports the temperature evolution at the same locations as in figure VI.4. The RBS modulation of the source is clearly visible. Figure VI.10 shows the square difference of the two modulated profiles as a function of time. This time the curve grows more rapidly than before, as reported by the next figure:

Some remarks

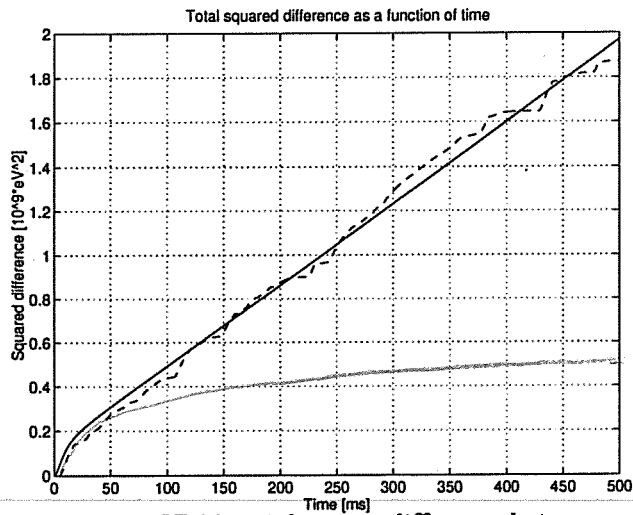


Figure VI.11: total square difference between the profiles as a function of the time.

The growing of the curve stabilizes around the same slope as for the non modulated case. Calculating the normalized variance, we get

$$\sigma_3^2 = \frac{\sum_{x,t} (T(p_1) - T(p_2))^2}{\sum_{x,t} T(p_1)^2} = 0.0071 \quad (\text{VI-7})$$

showing that this modulation provides a further improvement compared to the two previous cases. Like before, we calculate the eigenvalues of J2 and their relative ratios:

$$D_1 = 2.95 \cdot 10^8, D_2 = 5.49 \cdot 10^6, D_3 = 4.58 \cdot 10^2$$

$$\frac{D_1}{D_2} = 53, \frac{D_2}{D_3} = 1.2 \cdot 10^4 \quad (\text{VI-8})$$

The relationship between x_0 and Δx has again become sharper (compared to the non modulated case). The improvement compared to the non modulated case is in the order of a factor 2.7.

VI.4 On/Off square modulation

VI.4.1 Regularly spaced signal

This time the chosen signal for the modulation is a regularly spaced on/off square signal, having the form

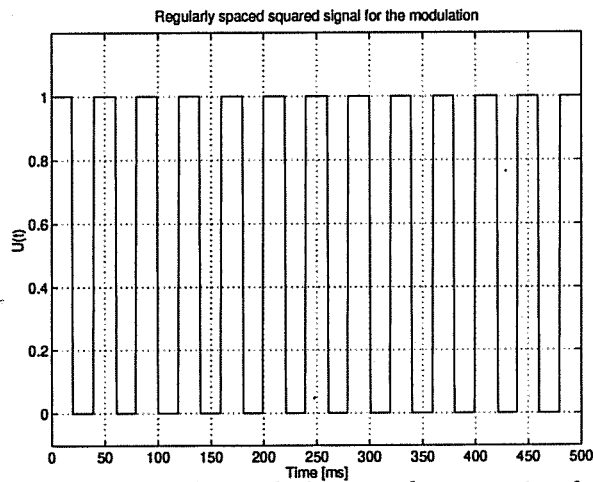


Figure VI.12: regularly spaced square signal.

Now, this time the quantity we need to fix in order to maximize the difference between the profiles, is the width of the square signal. As before, we plot this difference as a function of the searched width, and we obtain

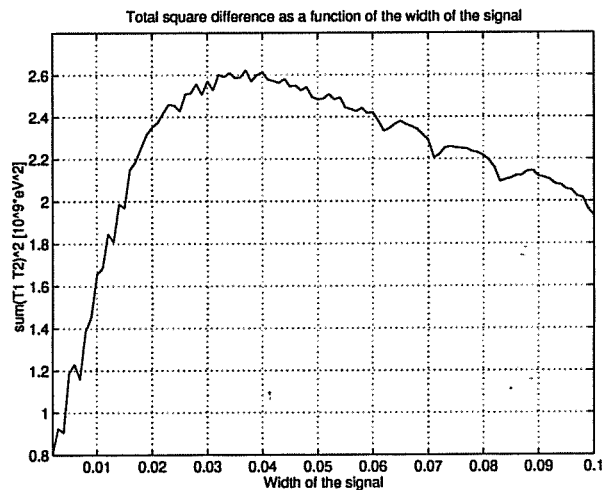


Figure VI.8: total square difference between the profiles as a function of the width of the signal.

From this curve, we set the value to be equal to 0.040 seconds. Modulating the source with this signal we obtain

note that this correspond to the optimum frequency for sine modulation

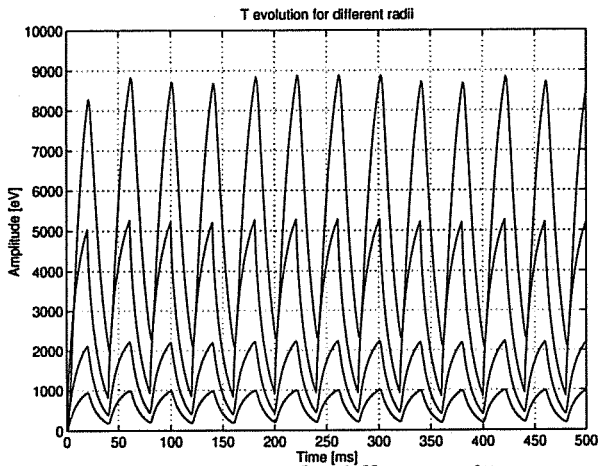


Figure VI.14: T evolution for different radii.

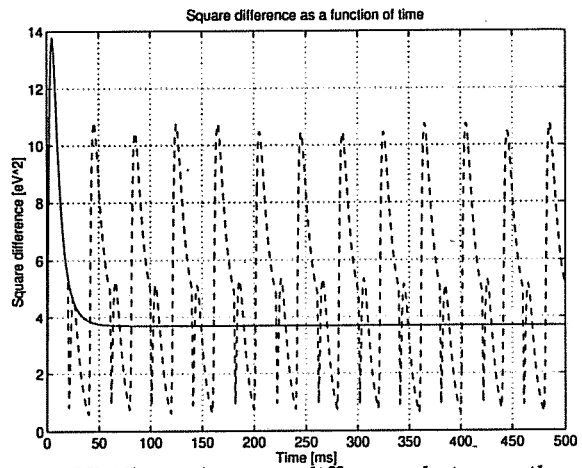


Figure VI.15: total square difference between the profiles as a function of time.

Figure VI.14 shows the temperature evolution at different locations. Figure VI.15 shows the square difference of the two modulated temperature profiles as a function of time. This time it is clearly visible how much bigger the difference between the two profiles is, due to the particular chosen modulation. We can see this better, plotting, as before, the total square difference as a function of time:

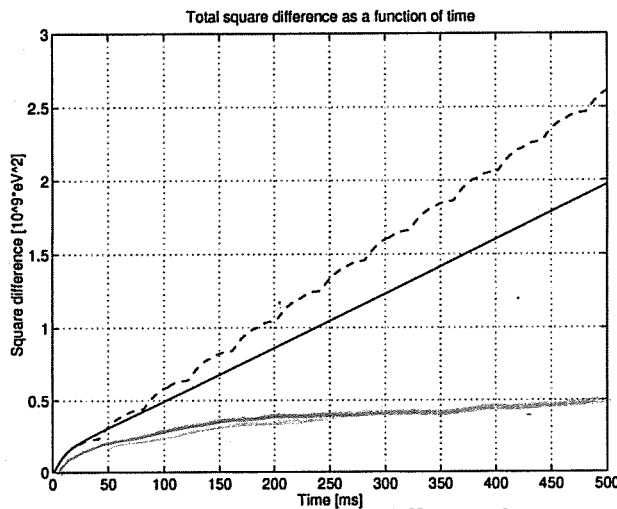


Figure VI.16: total square difference between the profiles as a function of time.

Calculating the normalized variance, we get

$$\sigma_4^2 = \frac{\sum_{x,t} (T(p_1) - T(p_2))^2}{\sum_{x,t} T(p_1)^2} = 0.0108 \quad (\text{VI-9})$$

The regularly spaced square signal provides then the best improvement so far for our purposes of separation. Calculating the eigenvalues of J2 and their relative ratios gives further evidence of the improvement:

$$D_1 = 2.84 \cdot 10^8, D_2 = 6.14 \cdot 10^6, D_3 = 5.59 \cdot 10^2$$

$$\frac{D_1}{D_2} = 46, \frac{D_2}{D_3} = 1.1 \cdot 10^4 \quad \text{(VI-10)}$$

The improvement, compared to the non modulated case, of the regularly spaced square signal, is of a factor 4.2.

Appendix F shows a few temporal evolutions with this chosen modulation.

VI.4.2 Optimized square signal

In section VI.4.1 we worked with a regularly spaced signal, meaning that the involved time intervals were all equal. Now, we try to see if there is a way to improve this case. Since the time needed by the temperature profile to rise is much smaller than the time taken to decrease, the idea is the following: we build a signal in which the time interval where the power is turned on, is shorter than the one when it is turned off. In this way, we let the profile approach zero again, the region where a greater difference in the profiles is detectable.

Keeping the time interval between one turn on of the additional power and the following at a constant value of 40 ms, we vary the time length of the pulse (heating turned on). Plotting this we get

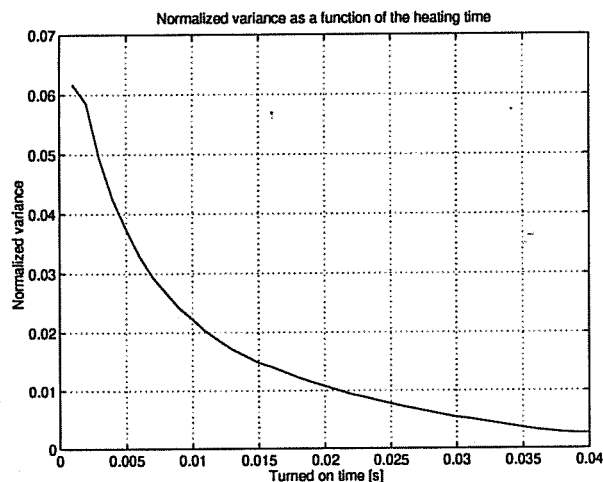


Figure VI.17: *normalized variance between the two profiles as a function of the turn on time.*

What comes out is that in principle, the shorter the heating pulse is, the higher the normalized variance becomes, revealing a bigger difference between the two profiles. On the other hand, though, if the pulse is too short, the temperatures reached during the evolution will be too low for a meaningful detection. Therefore we need to study the relationship between pulse length and reached temperatures, too.

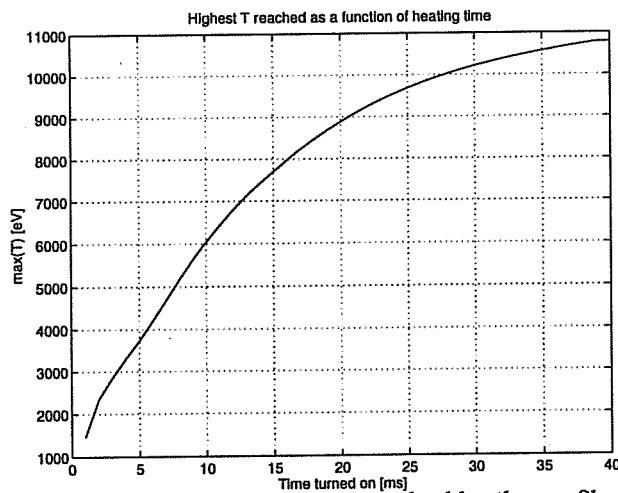


Figure VI.18: highest T reached by the profile as a function of the turn on time.

Figure VI.18 shows the maximum temperature reached as a function of the pulse length. Pulse lengths of 5-10 ms produce temperatures up to 4-6 keV, we can then choose in this time interval. A pulse of 10 or 5 ms has as consequence the following normalized variances between the resulting modulated temperature profiles:

$$\sigma_5^2 = \frac{\sum_{x,t} (T(p_1) - T(p_2))^2}{\sum_{x,t} T(p_1)^2} = 0.0223 \quad (\text{VI-11})$$

$$\sigma_6^2 = \frac{\sum_{x,t} (T(p_1) - T(p_2))^2}{\sum_{x,t} T(p_1)^2} = 0.0373 \quad (\text{VI-12})$$

Calculating the eigenvalues and their respective ratios for the case of a 5 ms pulse, we obtain

$$D_1 = 3.32 \cdot 10^7, D_2 = 1.44 \cdot 10^6, D_3 = 1.01 \cdot 10^2 \quad (\text{VI-13})$$

$$\frac{D_1}{D_2} = 23, \frac{D_2}{D_3} = 1.4 \cdot 10^4$$

Comparing these values with those without modulation, we have an improvement, for the normalized variance, of a factor 8.6 for 10 ms pulses, and of a factor 14.3 for 5 ms pulses. The improvement is evident.

Q: is there a better optimum if both frequency and duty cycle are varied?

Q: how can we compare when $\langle U(t) \rangle$ is varying (before always 10)

VI.5 Summary and remarks

Summarizing, for our purpose of localization of power deposition, several kinds of modulation were adopted and studied in order to increase the gap between the profiles resulting from the two chosen sets of parameters: a sinusoidal, a random binary and a square on/off modulation signal. Both for sinusoidal and regularly spaced modulations, the frequency cannot be chosen as high as wished, for if it is too high, the temperature profile will not have enough time to decrease consistently, and stationarity will be reached any way. Therefore, the frequency has to be chosen in order for the temperature to have enough time to decrease towards lower values, allowing, within reasonable limits, the restoring of the previous starting conditions.

Summarizing the results reached in the previous sections in a table, we get:

Modulation	σ^2	$D_1 [10^8]$	$D_2 [10^6]$	$D_3 [10^2]$	$\frac{D_1}{D_2}$	$\frac{D_2}{D_3} [10^4]$
None	0.0026	8.31	11.5	4.06	72	2.8
Sinusoidal	0.0079	2.37	4.43	3.59	53	1.2
RBS	0.0071	2.95	5.49	4.58	53	1.2
Regularly spaced	0.0108	2.84	6.14	5.59	46	1.1
Optimized	0.0373	0.33	1.44	1.01	23	1.4

Table VI.1

The next step is now the inverse problem: the reconstruction of the parameters with a fitting algorithm, starting from a given temperature profile evolution.

VII. Reconstruction of the parameters

The following step is now to create a reconstruction algorithm¹ that, starting from a reference temperature profile evolution and giving a first guess for the searched parameters, makes a fit of the data and minimizes a predefined functional. In our case, the functional to minimize is:

$$J(p) = \frac{1}{T_{\text{ref}}} \cdot \sqrt{\frac{1}{n_x \cdot n_t} \sum_{x,t} (T_0 - T(p))^2} \quad (\text{VII-1})$$

where T_{ref} is a reference temperature for the normalization of J ($T_{\text{ref}}=1\text{keV}$);
 $T_0 = T(p_0)$ represents the profile to reconstruct or, later on, the experimentally measured temperature profile evolution;
 $T(p)$ are the profiles built by the algorithm while minimizing J .

The reconstruction procedure will be executed for three cases: the non modulated, the regularly spaced and the optimized on/off signals.

VII.1 Reconstruction

VII.1.1 No modulation

The temperature profile evolution from which the parameters have to be regained, are the ones created from the following sets:

$$p_1 = [0.35, 0.08, 10^6 \text{ W}, 2.5 \cdot 10^{19} \text{ m}^{-3}, 10^{18} \text{ m}^{-3}, 10^{19} \text{ m}^{-1}\text{s}^{-1}, 6 \cdot 10^{19} \text{ m}^{-1}\text{s}^{-1}, 8 \text{ ms}^{-1}]$$
$$p_2 = [0.20, 0.30, 10^6 \text{ W}, 2.5 \cdot 10^{19} \text{ m}^{-3}, 10^{18} \text{ m}^{-3}, 10^{19} \text{ m}^{-1}\text{s}^{-1}, 4.2 \cdot 10^{19} \text{ m}^{-1}\text{s}^{-1}, 2.5 \text{ ms}^{-1}]$$

(VII-2)

Giving as first guess

$$p = [0.3, 0.1, 10^6 \text{ W}, 2.5 \cdot 10^{19} \text{ m}^{-3}, 10^{18} \text{ m}^{-3}, 10^{19} \text{ m}^{-1}\text{s}^{-1}, 5 \cdot 10^{19} \text{ m}^{-1}\text{s}^{-1}, 5 \text{ ms}^{-1}]$$

and applying the reconstruction algorithm we obtain²

¹Algorithm reconstr.m (Matlab 4.2c)

²The density parameters were kept fixed

$$\bar{p}_1 = [0.3500, 0.0800, 10^6, 2.5 \cdot 10^{19}, 10^{18}, 9.9999 \cdot 10^{18}, 6.0001 \cdot 10^{19}, 8.0000]$$

$$\bar{p}_2 = [0.2000, 0.3000, 10^6, 2.5 \cdot 10^{19}, 10^{18}, 9.9982 \cdot 10^{18}, 4.3001 \cdot 10^{19}, 2.4983]$$

where the $\bar{\cdot}$ defines the reconstructed parameters.

Both parameter vectors are accurately reconstructed due to the fact that the "experimental" temperature profile T_0 is actually a well defined function with no uncertainties produced by noise.

Adding some noise³ to the clean profile and recalculating the parameters, we get

$$\bar{p}_1 = [0.3469, 0.0609, 9.4153 \cdot 10^5, 2.5 \cdot 10^{19}, 10^{18}, 1.2661 \cdot 10^{19}, 5.2522 \cdot 10^{19}, 9.9460]$$

$$\bar{p}_2 = [0.1917, 0.3148, 1.0091 \cdot 10^6, 2.5 \cdot 10^{19}, 10^{18}, 1.2308 \cdot 10^{19}, 4.1308 \cdot 10^{19}, 4.8582]$$

Admitting an uncertainty of about 10% in the values of T_0 , it is clearly visible by how much the reconstructed parameters deviate from the actual value searched.

VII.1.2 Regularly spaced modulation

Again, applying the algorithm for the pure temperature profile (no noise) the starting parameters are reconstructed with practically no error.

Adding, as before, some noise, the following parameter estimates are obtained:

$$\bar{p}_1 = [0.3495, 0.0810, 9.9730 \cdot 10^5, 2.5 \cdot 10^{19}, 10^{18}, 9.8784 \cdot 10^{18}, 5.9728 \cdot 10^{19}, 7.7922]$$

$$\bar{p}_2 = [0.2077, 0.2935, 9.9749 \cdot 10^5, 2.5 \cdot 10^{19}, 10^{18}, 1.919 \cdot 10^{19}, 4.2091 \cdot 10^{19}, 3.3577]$$

The improvement is clear, giving further confirmation of the results obtained in chapter VI. Strong deviations are still detectable for the transport parameters $n\chi_0$, $n\chi_1$ and v_0 .

VII.1.3 Optimized modulation

Applying the reconstruction algorithm for the noise free profile again returns the exact parameters. Applying it in the case with noise added to the profile, it returns the following:

³Noise \propto 10% · T

$$\bar{p}_1 = [0.3501, 0.0785, 1.0040 \cdot 10^6, 2.5 \cdot 10^{19}, 10^{18}, 9.9421 \cdot 10^{18}, 6.0372 \cdot 10^{19}, 7.9960]$$

$$\bar{p}_2 = [0.1922, 0.3064, 9.9897 \cdot 10^5, 2.5 \cdot 10^{19}, 10^{18}, 9.7889 \cdot 10^{18}, 4.3319 \cdot 10^{19}, 2.3800]$$

For most of the parameters a further improvement is achieved, while for some others there is a stabilization or even a worsening.

VII.2 Results and discussion

Summarizing the results of the different reconstructions, we can make the following table:

p	Modulation	<i>reference</i> Absolute deviation from the real value [%]								
		<i>γ₀</i>	<i>dk</i>	<i>P_{in}</i>			<i>ω₀</i>	<i>ω₁</i>	<i>ω₂</i>	
P ₁	None	0.89	23.9	5.85	-	-	26.6	12.5	24.3	
	Reg. on/off	0.14	0.12	0.27	-	-	1.22	0.45	2.60	
	Opt. on/off	0.03	1.88	0.40	-	-	0.58	0.62	0.05	
P ₂	None	4.15	4.93	0.91	-	-	23.1	3.93	94.3	
	Reg. on/off	3.85	2.17	0.25	-	-	9.19	2.11	34.3	
	Opt. on/off	3.90	2.13	0.10	-	-	2.01	0.74	4.8	

Table VII.1

An important remark we can make, is that the quality improvement of the reconstruction is much greater when recalculating p_1 instead of p_2 . This is due to the fact that it was p_1 which was actually chosen as reference starting point, treating p_2 as a disturbance leading to the same stationary profile. During our thoughts and calculations, then, everything was done in order to separate the two sets from each other, basing the different choices, though, on p_1 and not on p_2 . The best frequency for the regularly spaced square signal, for example, was chosen studying the standard deviation of the two profiles with respect to the profile related to p_1 . This fact is now clearly visible in these last results: the chosen modulation reconstructs much better p_1 than p_2 . This means that future work will have to aim at this direction, trying to generalize the reconstruction procedure taking the statements above into consideration or iterating again using the reconstructed parameters as new starting

point for the next iteration. As already mentioned in chapter VI, the chosen modulation frequency depends on the "rising time" towards the stationary temperature profile. This means that further studies will have to deal with this fact. A first step that should be taken is the normalization of time, deepening its meaning and its consequences on the treated problem.

Table VII.1 also shows some less comprehensible results: if we look at the changes of the reconstructed parameters Δx , P_{in} , and $n\chi_1$ for p_1 , and x_0 and Δx for p_2 , we see that moving from the regularly spaced modulation to the optimized, these parameters are actually less precisely reconstructed. In this direction further investigations will have to be made.

I would also inspect the J_2 values for both cases. May be the 2nd one is "intentionally" less well "adjusted".

VIII. Analysis of TCV shot # 12508

has sent me

Finally, after the development of the reconstruction algorithm, it is now possible to attack a real experiment.

During the past campaign, four TCV shots were heated with modulated ECRH:

- TCV # 12505, 12506, 12507; modulation of 1 ms; injected power of 500 kW;
- TCV # 12508; modulation of 10 ms; injected power of 500 kW.

For all four shots the confinement time was of the order of 30-35 ms.

There are two reasons for the choice of shot # 12508 for the further analysis: the first one is because of time constraints, the second one is due to the sawtooth oscillations which have a period of about 2 ms, meaning that the modulation of 1 ms induces changes of the profiles in the range of the sawtooth instabilities themselves.

VIII.1 TCV shot # 12508

The shot was studied for $t \in [0.4 \text{ s}, 0.6 \text{ s}]$, the modulated ECRH being turned on at $t_0 = 0.44 \text{ s}$. The soft X-ray tomography system was chosen as the diagnostic for the extrapolation of the temperature profile evolution at different locations: of all the cameras in the system, three have been selected: cameras 1, 3 and 4. The next figure shows the experimental setup.

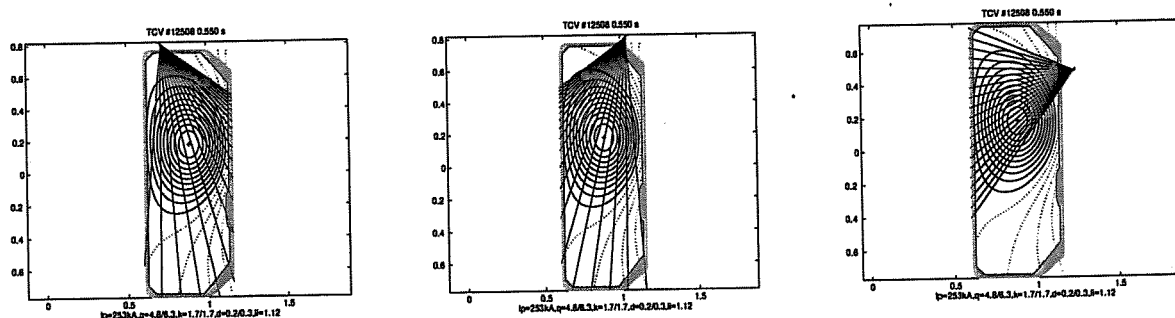


Figure VIII.1a/b/c: schematic view of the chords of the three chosen cameras for TCV shot # 12508.

Each camera has a set of 20 channels (expressed by the different chords in the figures), measuring the X-ray intensity along the chords. Since the greatest part of the emission is concentrated where the chord gets the closest to the center of the plasma (where the highest temperatures are reached), it is possible to gain information about the radial temperature profile¹. The coordinate x is then found approximating the total

¹Algorithm foram.m (Matlab 4.2c)

X-ray emission to the point where the chord is tangent to a magnetic flux surface. One typical emission signal is shown below.

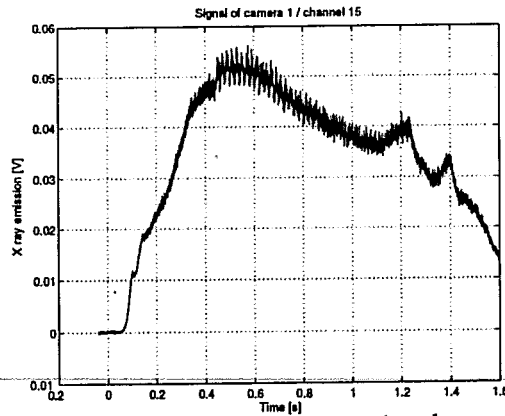


Figure VIII.2: X-ray emission signal measured by channel 15 of camera 1.

The moment in time when the external power is injected is clearly visible at $t \approx 0.44$ s. Appendix G shows a scope² survey of the shot. In particular, the injected and reflected power are reported.

The confinement time for this shot is $\tau_E \approx 34$ ms.

VIII.2 Tomography data processing

The stored signals from the three cameras have to be treated in such a way that the temperature profile evolution induced by the modulated ECRH can be derived. The base signal contains not only the additional heating, but also the ohmic heating, that means that we need to normalize the signal eliminating the ohmic part. This is carried out in this way:

$$s_{\text{norm}} = \frac{[(s - \text{offset}) - s_0]}{s_0} \quad (\text{VIII-1})$$

where s = basic signal; offset = mean value of s before starting the shot;
 s_0 = mean value reached through ohmic heating and before ECRH.

Having normalized the signal with (VIII-1), we can now focus our attention to the time interval we are interested in. Doing this we then obtain the result in the next figure.

²Scope: program used to display measurements of TCV shots

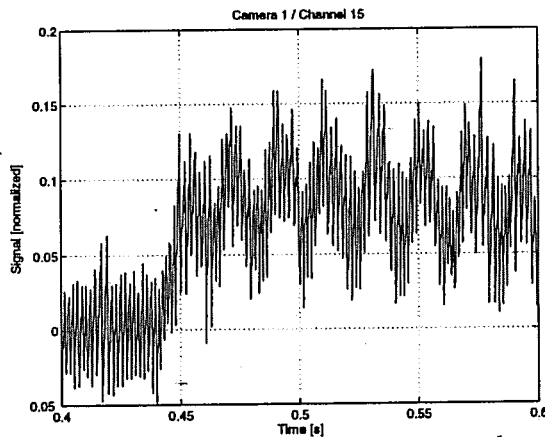


Figure VIII.3: normalized X-ray emission signal measured by channel 15 of camera 1 and focused for the time interval between 0.4 and 0.6 seconds.

This normalized signal is proportional to the temperature changes induced by ECRH. Taking advantage of the relationship

$$\Phi_X \propto n^2 T_e^\alpha$$

(VIII-2)

it then follows that

$$\frac{d\Phi_X}{\Phi_X} \propto \alpha \frac{dT_e}{T_e}$$

(VIII-3)

The curve shown in figure VIII.3 represents $d\Phi_X/\Phi_X$. T_e is the mean electron temperature and can be taken from the electron temperature profiles measured by the Thomson-scattering diagnostic system. This is, of course, only an approximation, considering that the temporal resolution of the Thomson diagnostic is 50 ms. The α coefficient is a term that depends on the impurities of the plasma. It is temperature dependent and can be approximated by a polynomial of 2nd degree in T with the assumption of just carbon impurities.

From (VIII-3) we then get

$$dT_e \propto \frac{d\Phi_X}{\Phi_X} \cdot \frac{T_e}{\alpha}$$

(VIII-4)

Proceeding in this way for all the channels of each camera leads to the final temperature evolution at different locations induced by ECRH.

In principle it should be possible to work with all 60 channels, but because many chords are pointed outside the outer border of the plasma, and because signals of other channels show large disturbances, a choice has been made: 41 out of the 60 possible channels have been chosen, covering the whole radius of the plasma.

The experimental temperature evolution signal has been defined as T_0 and has the dimensions 2001 x 41 (time x space).

VIII.3 Parameters reconstruction

Having transformed the base signal into a temperature profile evolution T_0 , it is now possible, as presented in the previous chapter, to reconstruct the parameters that generated our experimental profile.

The parameters of the density are now left out, since the density profile is known via the Thomson diagnostic. Applying the reconstruction algorithm³ we get

$$\begin{aligned} x_0 &= 0.50 \pm 0.07 & P_{in} &= (7.05 \pm 0.53) \cdot 10^4 \text{ W} & n\chi_1 &= (2.69 \pm 0.02) \cdot 10^{19} \text{ m}^{-1}\text{s}^{-1} \\ \Delta x &= 0.15 \pm 0.02 & n\chi_0 &= (4.87 \pm 0.02) \cdot 10^{19} \text{ m}^{-1}\text{s}^{-1} & v_0 &= 9.30 \pm 0.60 \text{ ms}^{-1} \end{aligned}$$

the error of each of the parameters being derived from the calculation of J2 (see later). A surprising result comes out from the reconstruction of the P_{in} parameter: values of 200-400 kW were expected but only about 70 kW have been calculated. As a check of the correctness of the reconstruction, P_{in} can also be calculated in a different way starting from dT/dt at the start of the ECH pulse and integrating over the whole space:

$$P = \frac{3}{2} e \int dV \frac{dT}{dt} n = \frac{3}{2} e (2\pi)^2 R a^2 \int dx \cdot x \cdot \frac{dT}{dt} = 5.48 \cdot 10^4 \text{ W} \quad \text{(VIII-5)}$$

where is R?

This calculation confirms the order of the value found above. The great amount of losses is probably due to a bad conditioning of the device during this particular shot.

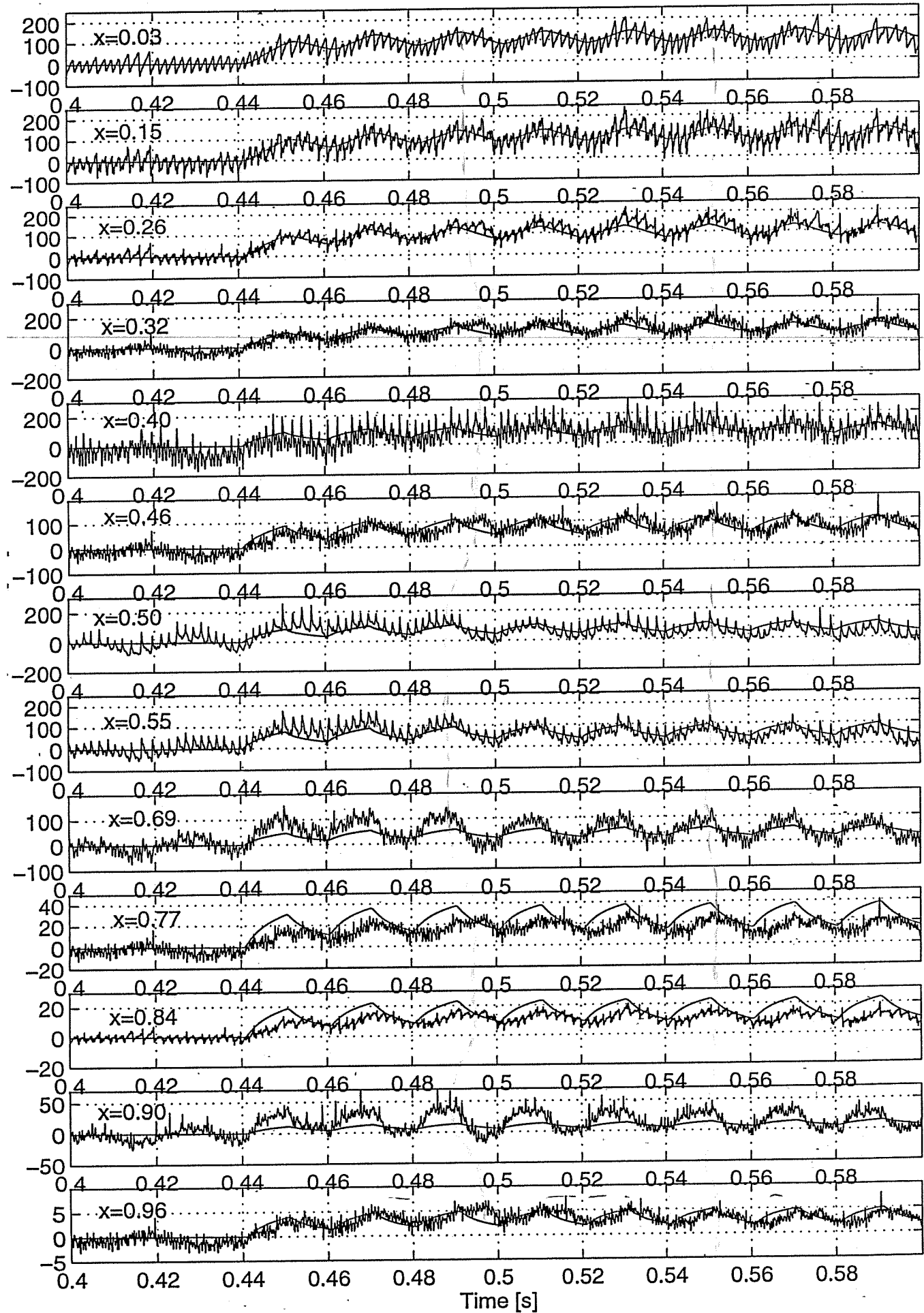
From the reconstruction algorithm we obtain a power deposition localized at $x_0 = 0.50$ with a width of $\Delta x = 0.15$. As further evidence that x_0 is actually localized in this region, the figure in the next page shows a selection of experimental signals and reconstructed profiles for different x 's. Looking at the phase of the signals shows the region of the power deposition. Appendix H shows all the experimental profiles with their corresponding reconstructed curves.

Calculating the normalized variance between the experimental and the reconstructed profiles we obtain

$$\sigma^2 = \frac{\sum_{x,t} (T_0 - T(P_1))^2}{\sum_{x,t} T_0^2} = 0.1438 \quad \text{(VIII-6)}$$

³Algorithm rec.m (Matlab 4.2c)

T evolution at different radii



where p_1 stands for the reconstructed parameters, leading to an average difference between T_0 and T of the order of 38%, but we will come back to this later.

Calculating the J_2 matrix for the reconstructed parameters and taking the experimental T_0 as the reference point we get

$$J_2 = \begin{bmatrix} 0.60 \cdot 10^6 & -0.67 \cdot 10^6 & 0 & 0 & 0 & 6.6 \cdot 10^3 \\ -0.67 \cdot 10^6 & 3.80 \cdot 10^6 & 0 & 0 & 0 & 4.4 \cdot 10^3 \\ 0 & 0 & 0 & 0 & 0 & 0 \\ 0 & 0 & 0 & 0 & 0 & 0 \\ 0 & 0 & 0 & 0 & 0 & 0 \\ 6.6 \cdot 10^3 & 4.4 \cdot 10^3 & 0 & 0 & 0 & 6.0 \cdot 10^2 \end{bmatrix}$$

and for the eigenmode-eigenvalue decomposition

$$D = \begin{bmatrix} 3.94 \cdot 10^6 & & & & & \\ & 4.65 \cdot 10^5 & & & & \\ & & 4.36 \cdot 10^2 & & & \\ & & & 5 \cdot 10^{-13} & & \\ & & & & 10^{-69} & \\ & & & & & 0 \end{bmatrix}$$

$$V = \begin{bmatrix} 0.20 & -0.98 & & & & \\ -0.98 & -0.20 & & & & \\ & & -1.00 & & & \\ & & & & & 1.00 \\ & & & & -1.00 & \\ & -1.00 & & & & \end{bmatrix}$$

with the ratios

$$\frac{D_{11}}{D_{22}} = 8 \quad \text{and} \quad \frac{D_{22}}{D_{33}} = 1.1 \cdot 10^3$$

These results show that the biggest contribution to the difference between the calculated and the experimental profile is given by the two localization parameters. Power deposition localization developed with the TORAY code [16] confirmed the results found by the reconstruction algorithm. The next figures show TORAY results.

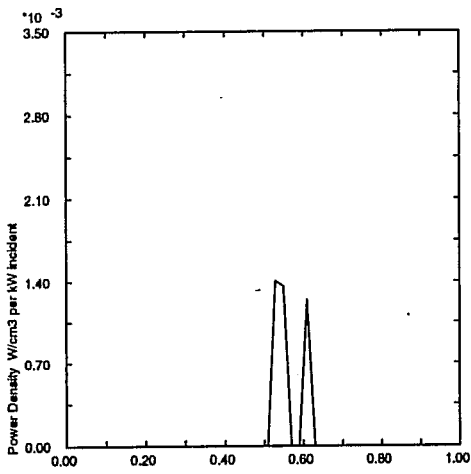


Figure VIII.5: TORAY power deposition localization.

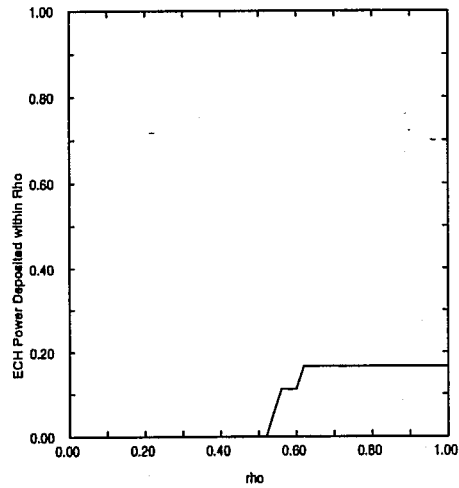


Figure VIII.6: TORAY normalized deposited power.

Figures VIII.5 and VIII.6 show a power deposition in the region $x_0 \in [0.5, 0.6]$ and a deposited power of less than 20% of the actual injected power. The scope survey of this shot (see Appendix G) allows us to get the information about the injected power, and it is of the order of 400 kW. This means that only about 70-80 kW are actually deposited, confirming the results of the reconstruction algorithm.

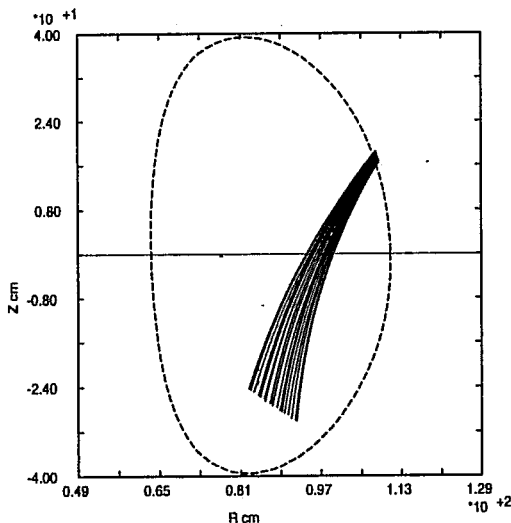


Figure VIII.7: ECRH waves trajectory during heating.

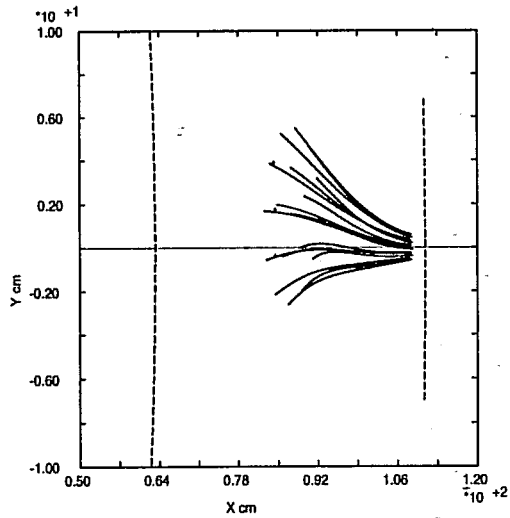


Figure VIII.8: top view of Figure VIII.7.

Figures VIII.7 and VIII.8 clarify the problem of the bad heating effectiveness: since the plasma of this shot has a large elongation, the angle of incidence of the ECRH waves has to be very large to aim at the center of the plasma. Doing this, though, diffraction effects become important, avoiding an effective heating at the resonance of the plasma.

A few words have now to be spent on the large value found for the normalized variance and the relative average difference between the profiles. Consider the next figures.

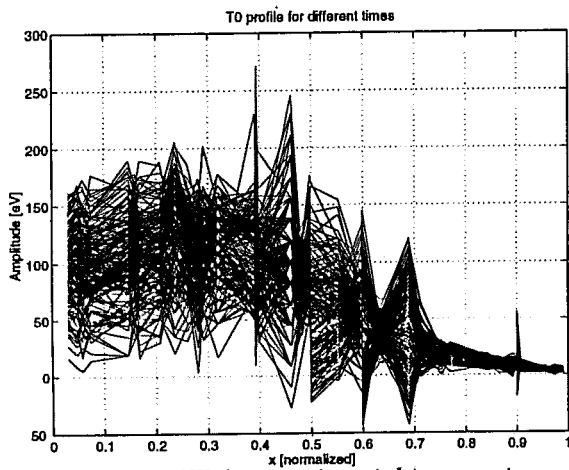


Figure VIII.9: *experimental temperature profile during 0.02 seconds.*

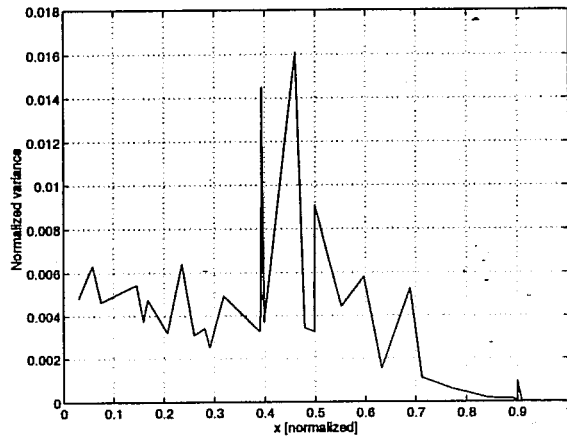


Figure VIII.10: *normalized variance of each channel.*

Figure VIII.9 shows the experimental temperature profile evolution during 0.02 seconds (containing then the modulation); Figure VIII.10 shows the contribution that each channel gives to the total normalized variance.

It is hard to find the right explanation for the large value found. There are a few channels in which the temperature oscillates way outside the "mean oscillation region". This could be due to the different spatial distribution of the chords of the three used cameras as well as to more uncertain values of the exponent α , that means, to greater incertitudes for the impurities.

These are, though, only a few possibilities, maybe even related to the dispersion phenomena of the ECRH waves visible in Figure VIII.7. More time should be invested to try to identify the actual reasons of this situation.

IX. Conclusions

The aim of the work that was carried out and summarized in this report, ^{main} was the study of the energy transport equation with respect to a set of chosen parameters upon which it directly depends. ^{main} The ultimate goal of this research and of the further improvements it needs, is the localization of the ECRH power deposition in TCV. ^{main + reliability}

the self system
In order to gain useful information about the behaviour of the temperature profile depending on the given set of parameters, the solution of the transport equation has been calculated and an algorithm for $T=T(p)$ has been developed, allowing the calculation of the temperature profile evolution for any set of parameters. The high number of parameters involved (eight) reinforces the actual need to formalize the problem, in order to be able to deepen the study of the different dependences. This formalization of the problem leads to the construction of the J2 matrix, representing the second derivative matrix of the function J (defined by (IV-1)) and giving the mean square difference of a temperature profile evaluated in p with respect to a reference profile T_0 evaluated in a reference point p_0 .

The formalization allows us to find three sets of parameters leading to the same stationary temperature profile. The meaning of this result is that, in principle, starting from a measured stationary profile (disturbed by a certain amount of noise due to the many plasma instabilities), it is not possible to reconstruct the original set of parameters that generated it. The simple straight application of a fitting algorithm to a stationary temperature profile could therefore lead to the wrong parameters. *good*

The way out of this situation is the study of the temporal evolution of the profiles, leading to the need of modulating the external power injection in order to separate the profiles belonging to different sets of parameters. *good but need further formal*

Having determined (through investigation of J2) that the main characteristics of the J function are not very much affected by differently chosen ratios between diffusion and convection parameters, as well as by different chosen x_0 's (section V.4), we then passed to the treatment of the problem with modulated sources (chapter VI), concentrating our study on the separation of two of the three treated starting vectors. *give the results (30) (00)*

Modulations with four different signals (sinusoidal, RBS, regularly spaced on/off and optimized on/off) show, always keeping in mind the confinement time, the improvement of the separability of the temperature profiles through calculation of *not defined*

normalized variance and eigenvalues of the J2 matrix. The investigation shows that, with the optimized on/off signal, the improvement of separability is, for the normalized variance, of the order of a factor 14, leading to an absolute improvement of almost a factor 4.

The studying of a reconstruction algorithm gives further evidence of the improvement found in the previous chapter, pointing out the importance of the chosen modulation. A particularly well chosen modulation is the basis for a good power deposition localization.

The study of the TCV shot # 12508, which is, at the moment, the only treatable experimental shot with modulated ECRH, reveals a power deposition at $x=0.50$ (normalized units) with a corresponding width of $\Delta x=0.15$ (normalized units). The actual absorbed power has been found to be about 70 kW compared to the approximately 400 kW that have not been reflected and that arrived in the torus. TORAY calculations confirm these results pointing out that the reason of this important loss of power is probably due to dispersion of the injected radiation because of the large angle of incidence.

A graph also of "error bars" to show that reliability, the major concern of your work, has been assessed.

X. Bibliography

- [1] N. J. Lopes Cardozo, Perturbative Transport Studies in Fusion Plasmas, *Plasma Physics and Controlled Fusion*, **37**, 799 (1995)
- [2] J. Paméla et M. Chatelier, **Des premier tokamaks au projet ITER**, *La Recherche* (june 1997)
- [3] J. Wesson, **Tokamaks**, Oxford Science Publications (1987)
- [4] CRPP, CRPP-TF/EPFL, Report 1993-1994
- [5] A. Pochelon, Electron Cyclotron Resonance Heating, for the 36th Course of the "Association Vaudoise des Chercheurs en Physique", published as LRP 505/94 (1994)
- [6] I. H. Hutchinson, **Principles of Plasma Diagnostics**, Cambridge University Press (1992)
- [7] M. Anton et al., X-Ray Tomography on TCV, published as LRP 547/96 (1996)
- [8] T. P. Goodman et al., Invited paper at the 3rd International Workshop on Strong Microwaves in Plasmas, Nizhny Novgorod, published as LRP 556/96 (1996)
- [9] G.B. Arfken and H.J. Weber, **Mathematical Methods for Physicists**, Academic Press, 4th edition (1995)
- [10] J.M. Moret, Identification of Systems with Distributed Parameters, EUR-CEA-FC-1409 (1990)
- [11] J.-M. Moret et al., Tokamak Transport Phenomenology and Plasma Dynamic Response, *Nuclear Fusion*, **32**, 1241 (1992)
- [12] D. J. Gambier et al., ICRF Power Deposition Profile and Determination of the Electron Thermal Diffusivity by Modulation Experiments in JET, *Nuclear Fusion*, **30**, 23 (1990)
- [13] Hogeweji et al., The Analysis of Coupled Heat and Particle Transport in Tokamaks by Means of Fourier Transform, *Plasma Physics and Controlled Fusion*, **34**, 641 (1992)
- [14] E. Barbato et al., A Possible Measure of the Energy Deposition Profile in Additional Plasma Heating Experiments (?)
- [15] J.C.M. deHaas et al., Modulated ECH Experiments at DIII-D, General Atomics
- [16] R.C. Myer et al., Electron Cyclotron Wave Propagation and Absorption in the Compact Ignition Tokamak, *Nuclear Fusion*, **29**, 2155 (1989)

Appendix A

List of the principle algorithms used for the different calculations of this report.

```

serie1_def.m
% Stationary transport equation
% Diffusion n*Chi=nChi0;
% Convection u=0;

% Fixed parameters
a=.24;
R0=.89
Pin=1E6;
e=1.6e-19;
x=linspace(0,1,41);
alpha=bessel0zeros(30);
nChi0=1e19;

% Source
Q0=Pin/(R0*pi^2*a^2)/nChi0/e;
Q=Q0*(1-x.^2);

% Problem resolution
J=besselj(0,x*alpha);
d=J\Q;
alpha1=alpha.^2;
c=a^2*d./alpha1;
T=J*c;

plot(x,T); grid on;
xlabel('x [normalized]'); ylabel('Amplitude [eV]');
title('T profile for different nChi0');

)

serie2_def.m
% Stationary transport equation
% Diffusion n*Chi=nChi0+nChi1*(x/a)^2
% Convection u=u0*x/a

% Fixed parameters
a=.24;
R0=.89;
Pin=1E6;
nChi0=1E19;
e=1.6E-19;
n0=1E19;
x=linspace(0,.24,41);
L1=length(x);
x2=x.^2;
x3=x.^3;
alpha=bessel0zeros(21);
alpha2=alpha.^2;
L2=length(alpha);

X=rep(x,L2);
X2=rep(x2,L2);
X3=rep(x3,L2);
alm=rep(alpha,L1);
al2m=rep(alpha2,L1);
J=besselj(0,x*alpha/a);
J1=besselj(1,x*alpha/a);

% Variable parameters
nChi1=0;
u0=0;
Q0=Pin/(R0*pi^2*a^2)/e;
c1=nChi0/a^2;
c2=nChi1/a^3;
c3=nChi1/a^4;
c4=5/2*n0*u0/a;
c5=5/2*n0*u0/a^2;

% Problem resolution
M=c1*J.*al2m+c2*J1.*alm+c3*(J-J1).*al2m+c4*(2-4/a*X2).*J+c5*(X-
X3/a).*J1;
Q=Q0*(1-x.^2/a^2);
A=J\M;
[U,S,V]=svd(A);
c=eig(S);

T=J*U;
q=T\Q;
b=q./c;
T1=T*b;

plot(x/a,T1)
xlabel('x [normalized]')
ylabel('Amplitude [eV]')
title('T profile for different nChi and v')

serie3_def.m
function T=serie3_def(p)
% TPROFILE(p)
%
% p=[Pin n0 na nChi0 nChi1 u0];
% x0 (deposition [normalized units])
% deltax (FWHM [normalized units])
% Pin (power in [W])
% nChi(x)=nChi0+nChi1*x^2 (diffusion [m^-1*s^-1])
% u=u0*x (convection [m/s])
% n=(n0-na)*(1-x^2)+na (density [m^-3])
% p=[1E6 2.5E19 1E18 1E19 6E19 7.5];

```

```

% Physical parameters
a=.24;
R=.89;
e=1.6E-19;
nChi0=1E19;

% Computation parameters
nx=41;
x=linspace(0,1,nx)';
nJ=21;
alpha=bessel0zeros(nJ);
J0=besselj(0,x*alpha);
J1=besselj(1,x*alpha);
psitbxsg('NRHG',nx,'NTHG',7)
[grad,div]=psitbxrhp('1S',DIV);
Pin=p(1); n0=p(2); na=p(3); nChi0=p(4); nChi1=p(5); u0=p(6);
u=u0*x;
nChi=nChi0+nChi1*x.^2;
n=(n0-na)*(1-x.^2)+na;

% Definition of the source
G=1-x.^2;
G=G*(Pin/(4*pi^2*a^2*R/nx*sum(G.*x)));

% Transport operator
Lcond=e/a.^2*(-diag(grad*nChi)*J1*diag(alpha)-
diag(nChi)*J0*diag(alpha.^2));
Lconv=e/a.^3/2*(diag(div*(n.*u))*J0-dia(n.*u)*J1*diag(alpha));
L=Lcond+Lconv;

% ss matrices
A=J0\diag(2/3/e./n)*L;
B=J0\diag(2/3/e./n)*G;
C=J0;

% Solution
T=-C*(A\B);

plot(x,T)
% xlabel('x [normalized]'); ylabel('Amplitude [eV]')
% plot(x,angle(T))

tprofile.m
function T=tprofile(p)
% TPROFILE(p)
%
% p=[x0 deltax Pin n0 na nChi0 nChi1 u0];

% Physical parameters
% x0 (deposition [normalized units])
% deltax (FWHM [normalized units])
% Pin (power in [W])
% nChi(x)=nChi0+nChi1*x^2 (diffusion [m^-1*s^-1])
% u=u0*x (convection [m/s])
% n=(n0-na)*(1-x^2)+na (density [m^-3])
% p=[500 .35 .08 1E6 2.5E19 1E18 1E19 6E19 8];

% Physical parameters
a=.24;
R=.89;
e=1.6E-19;
nChi0=1E19;

% Computation parameters
nx=41;
x=linspace(0,1,nx);
nJ=21;
f=p(1); x0=p(2); dx=p(3); Pin=p(4); n0=p(5);
na=p(6); nChi0=p(7); nChi1=p(8); u0=p(9);
w=2*pi*f;
u=u0*x;
nChi=nChi0+nChi1*x.^2;
n=(n0-na)*(1-x.^2)+na;
alpha=bessel0zeros(nJ);
J0=besselj(0,x*alpha);
J1=besselj(1,x*alpha);
psitbxsg('NRHG',nx,'NTHG',7)
[grad,div]=psitbxrhp('1S',DIV);

% Definition of the source
G=exp(-(x-x0)/dx).^2;
G=G*(Pin/(4*pi^2*a^2*R/nx*sum(G.*x)));

% Transport operator
Lcond=e/a.^2*(-diag(grad*nChi)*J1*diag(alpha)-
diag(nChi)*J0*diag(alpha.^2));
Lconv=e/a.^3/2*(diag(div*(n.*u))*J0-dia(n.*u)*J1*diag(alpha));
L=Lcond+Lconv;

% ss matrices
A=J0\diag(2/3/e./n)*L;
B=J0\diag(2/3/e./n)*G;
C=J0;

for k=1:length(alpha)
id(k,k)=1;
end;
wm=w*id;

% Solution
T=C*(i*wm-A)\B);

```

```

% plot(x,abs(T))
% xlabel('x [normalized]'); ylabel('Amplitude [eV])
% plot(x,angle(T))

evolution1.m
function [Tinf,T]=evolution1(p)
% TEVOLUTION(p)
%
% p=[x0,deltax,Pin,n0,na,nChi0,nChi1,u0];
% x0 (deposition [normalized units])
% deltax (FWHM [normalized units])
% Pin [power in [W])
% nChi(x)=nChi0+nChi1*x^2 (diffusion [m^-1*s^-1])
% u=u0*x (convection [m/s])
% n=(n0-na)*(1-x^2)+na (density [m^-3])
% p=[.35 .08 1E6 2.5E19 1E18 1E19 6E19 8];

% Physical parameters
a=.24;
R=.89;
e=1.6E-19;
nt=501; t=linspace(0,.5,nt);
x0=p(1); dx=p(2); Pin=p(3); n0=p(4); na=p(5);
nChi0=p(6); nChi1=p(7); u0=p(8);

% Computation parameters
nx=41;
x=linspace(0,1,nx);
nJ=21;
u=u0*x;
nChi=nChi0+nChi1*x.^2;
n=(n0-na)*(1-x.^2)+na;
alpha=bessel0zeros(nJ);
J0=besselj(0,x*alpha);
J1=besselj(1,x*alpha);
psitbxgsg(NRHG,nx,NTHG,7)
[grad,div]=psitbxrhp('1S',DIV);

U=ones(size(t));
% Definition of the source
Q=exp(-(x-x0)/dx).^2;
Q=Q*(Pin/(4*pi^2*a^2*R/nx*sum(Q.*x)));

% Transport operator
Lcond=e/a^2*(-diag(grad*nChi)*J1*diag(alpha)-
diag(nChi)*J0*diag(alpha.^2));
Lconv=e/a^3/2*(diag(div*(n.*u))*J0-dia(n.*u)*J1*diag(alpha));
L=Lcond+Lconv;

% Computational matrices
A=J0\diag(2/3/e./n)*L;
B=J0\diag(2/3/e./n)*Q;
C=J0;
Dz=zeros(nx,1);

% Steady solution
Tinf=C*(A\B);

% Evolution
T=lsim(A,B,C,Dz,U,t);
% mesh(x,t,T)
% set(gca,'XDir','reverse')

main_alg1.m
% Main program
% p1=[.35 .08 1E6 2.5E19 1E18 1E19 6.0E19 8.0];
% p2=[.20 .30 1E6 2.5E19 1E18 1E19 4.3E19 2.5];
% p3=[.43 .25 1E6 2.5E19 1E18 1E19 5.2E19 12.0];
% p=[.3 .1 1e6 2.5e19 1e18 1e19 5e19 5];
% p0=[.35 .08 1E6 2.5E19 1E18 1E19 6E19 9.0];

global a R e n0 Chi0 nx x t nJ nt alpha J0 J1 grad div M M1
a=.24; R=.89; e=1.6E-19; nx=41; nJ=21; nt=501;
n0=1e19; Chi0=1; x=linspace(0,1,nx);t=linspace(0,.5,nt);
alpha=bessel0zeros(nJ);
J0=besselj(0,x*alpha);
J1=besselj(1,x*alpha);
psitbxgsg(NRHG,nx,NTHG,7)
[grad,div]=psitbxrhp('1S',DIV);
M(1,1)=1; M(2,2)=1; M(3,3)=1e6; M(4,4)=1e19;
M(5,5)=1e19; M(6,6)=1e19; M(7,7)=1e19; M(8,8)=10;
M1(1,1)=1; M1(2,2)=1; M1(3,3)=a^2/(Chi0*1000); M1(4,4)=1/n0;
M1(5,5)=1/n0;
M1(6,6)=1/(n0*Chi0); M1(7,7)=1/(n0*Chi0); M1(8,8)=a/Chi0;

U1=ones(size(t));
U2=sin(2*pi*8.5*t).^2;
rand('seed',0);
U3(1)=0;
for i=2:length(t)
ch=rand(1);
if ch<.95
U3(i)=U3(i-1);
else
U3(i)=~U3(i-1);
end
end

```

```

end
end;
for i=1:length(t)
if rem(t(i),.06)<.03
    U5(i)=1;
else
    U5(i)=0;
end
end;
% global T0
% [Tinf,T0]=evol(p0,U); [K,L]=size(T0);
% for k=1:K
% for l=1"L
% To(k,l)=T0(k,l)+randn(1)*T0(k,l)/10;
% end;
% end;

% T profile
[Tinf,T0]=evol(p0,U);
% J2 matrix
[J2,V,D]=deriv(p0,U);
% Contour
F=lev_norm(p0,U,10);
% Reconstruction algorithm
p=[.3 1 1e6 2.5e19 1e18 1e19 5e19 5];
p=reconstr(p,p0,U);

evol.m
function [Tinf,T]=evol(p,U)
global a R e n x nt x nJ alpha J0 J1 grad div M1

% TEVOLUTION(p,U)
%
% p=[x0,deltax,Pin,n0,na,nChi0,nChi1,u0];
% x0 (deposition [normalized units])
% deltax (FWHM [normalized units])
% Pin (power in [W])
% nChi(x)=nChi0+nChi1*x^2 (diffusion [m^-1*s^-1])
% u=u0*x (convection [m/s])
% n=(n0-na)*(1-x^2)+na (density [m^-3])
% p=[.35 .08 1E6 2.5E19 1E18 1E19 6E19 7];
% Physical parameters
x0=p(1); dx=p(2); Pin=p(3); n0=p(4); na=p(5);
nChi0=p(6); nChi1=p(7); u0=p(8);

% Computation parameters
u=u0*x;
nChi=nChi0+nChi1*x.^2;
n=(n0-na)*(1-x.^2)+na;

% Definition of the source
Q=exp(-(x-x0)/dx).^2);
Q=Q*(Pin/(4*pi^2*a^2*R/nx*sum(Q.*x)));

% Transport operator
Lcond=e/a^2*(-diag(grad*nChi)*J1*diag(alpha)-
diag(nChi)*J0*diag(alpha.^2));
Lconv=e/a^3/2*(diag(div*(n.*u))*J0-dia(n.*u)*J1*diag(alpha));
L=Lcond+Lconv;

% Computational matrices
A=J0\diag(2/3/e./n)*L;
B=J0\diag(2/3/e./n)*Q;
C=J0;
Dz=zeros(nx,1);

% Steady solution
Tinf=C*(A\B);

% Evolution
T=ism(A,B,C,Dz,U,t);
% mesh(x,t,T); set(gca,'XDir','reverse')

deriv.m
function [J2,V,D]=deriv(p0,U)
global a R e n x nt x nJ alpha J0 J1 grad div M1

% DERIV(po,dp)
% p0=[x0,deltax,Pin,n0,na,nChi0,nChi1,u0] (starting point;
reference)

% Reference
% p0=[.35 .08 1E6 2.5E19 1E18 1E19 6E19 9];

[Teff,T0]=evol(p0,U);
dp=[0.1/10000 p0(2)/10000 p0(3)/10000 p0(4)/10000
p0(5)/10000 p0(6)/10000 1E14 1E-4];

% Construction of J2
for k=1:8
    p=p0;
    p(k)=p(k)+dp(k);
    [Teff,T]=evol(p,U);
    J2(k,k)=2/dp(k)^2*sum(sum(abs(T0-T).^2));
end;

for k=1:8
    for l=k+1:8
        p=p0;
        p(k)=p(k)+dp(k);

```

```

p(l)=p(l)+dp(l);
[Teff,T]=evol(p,U);
J2(k,l)=1/(dp(k)*dp(l))*(sum(sum(abs((TO-T).^2)))-.5*J2(k,k)*dp(k)^2-
.5*J2(l,l)*dp(l)^2);
J2(l,k)=J2(k,l);
end
end;
J2=J2/nx/nt;
J2=M1*J2*M1;
[V,D]=eig(J2);

lev_norm.m
function F=lev_norm(p0,U,lines)
global a
% p0=[x0 deltax Pin n0 na nChi0 nChi1 u0]
% p0=[.35 .08 1E6 2.5E19 1E18 1E19 6E19 9];
Chi0=1; n0=1E19; TO=1000;
dp1=[.1/100 .01/100 p0(3)/100 p0(4)/100 p0(5)/100 1E14 1E12
1E-4];
M(1,1)=1; M(2,2)=1; M(3,3)=a^2/(Chi0*TO);
M(4,4)=1; M(5,5)=1; M(6,6)=1/(n0*Chi0);
M(7,7)=1/(n0*Chi0); M(8,8)=a/Chi0;
dp0=M*dp1;
[J2,D,V]=deriv(p0,U);
for i=1:11,
for j=1:11,
dp=[(i-6)*40*dp0(1),(j-6)*2000*dp0(2),0,0,0,0,0,0];
F(i,j)=1/2*dp'*J2*dp;
end;
end;
for i=1:11
x1(i)=(i-6)*40*dp0(1);
y1(i)=(i-6)*2000*dp0(2);
end;
contour(x1,y1,F,lines)
xlabel('x0 variation [normalized]')
ylabel('dx variation [normalized]')
grid on
title('Deviation x0 and deltax')
reconstr.m
function p=reconstr(p,p0,U)
global nx nt M U TO
p=inv(M)*p;
vib=[0 .01 .5 p(4) p(5) .1 .1 -1];
vub=[1 1 1.5 p(4) p(5) 10 10 +1];
p=constr('fun',p,[],vib,vub);
p=M*p;

fun.m
function [J,g]=fun(p,p0)
global nx nt M U TO
p=M*p;
[Tinf,T]=evol(p,U);
J=sqrt(1/nx/nt*sum(sum(abs((TO-T).^2)))/1000);
g=[];

board.m
global nx x1 xx nt t n M M1 a e R nJ alpha J0 J0x J1 grad div T0 U
load x1; xx=linspace(0,1,41); load n;n=n'; load t; load t0;
nx=length(x1); nt=length(t); nJ=21; a=-24*sqrt(1.7); R=.89; e=1.602e-19;
x1=x1';
alpha=bessel0zeros(nJ);
J0x=besselj(0,xx*alpha);
J0=besselj(0,x1*alpha);
J1=besselj(1,xx*alpha);
psitbxsg('NRHG',41,'NTHG',7)
[grad,div]=psitbxrhp('IS','DIV');Chi0=1;n0=1e19;
M(1,1)=1; M(2,2)=1; M(3,3)=1e5; M(4,4)=1e19; M(5,5)=1e19;
M(6,6)=10;
M1(1,1)=1; M1(2,2)=1; M1(3,3)=a^2/(Chi0*1000);
M1(4,4)=1/(n0*Chi0); M1(5,5)=1/(n0*Chi0); M1(6,6)=a/Chi0;
t=t';
for i=1:length(t)
if t(i)<.4405
U(i)=0;
else
if rem(t(i)-.4405,.02)<.01
U(i)=1;

```

```

else
  U(i)=0;
end
end
end
end;

p=[0.1 5.0e5 1e19 1e19 0];
p1=rec(p);
[Tinf,T]=calct(p1);
[J2,V,D]=j2_exp(p1);
function p=rec(p)

global nx x1 xx nt t n M M1 a e R nJ alpha J0 J0x J1 grad div T0 U

p=inv(M)*p;
vlb=[0 -0.1 1 1 1 -1]; % no density!
vub=[1 1 7 10 10 1]; % no density!

opt(1)=1; opt(14)=1000;
p=constr('funz',p,opt,vlb,vub);

p=M*p;
function [J,g]=funz(p)

global nx x1 xx nt t n M M1 a e R nJ alpha J0 J0x J1 grad div T0 U

p=M*p;
[Tinf,T]=calct(p);

J=sqrt(1/nx/nt*sum(abs((T0-T).^2)))/1000;
g=[];
function [Tinf,T]=calct(p)

% TEVOLUTION(p)
%
% p=[x0,deltax,Pin,nChi0,nChi1,u0];
% x0 (deposition [normalized units])
% deltax (FWHM [normalized units])
% Pin (power in [W])
% nChi(x)=nChi0+nChi1*x^2 (diffusion [m^-1*s^-1])
% u=u0*x (convection [m/s])
% Pin modulated with square fct of period 40ms

global x1 xx a R e t nJ nt nx alpha J0x J0 J1 grad div n U

% Physical parameters
x0=p(1); dx=p(2); Pin=p(3); nChi0=p(4); nChi1=p(5); u0=p(6);
nChi=nChi0+nChi1*xx.^2;
% Definition of the source
G=exp(-(xx-x0)/dx).^2;
G=G*(Pin/(4*pi^2*a^2*R/41*sum(G.*xx)));
% Transport operator
Lcond=e/a^2*(-diag(grad*nChi)*J1*diag(alpha)-diag(nChi)*J0x*diag(alpha.^2));
Lconv=e/a^3/2*(diag(div*(n.*u))*J0x-dia(n.*u)*J1*diag(alpha));
L=Lcond+Lconv;
% Computational matrices
A=J0x\diag(2/3/e./n)*L;
B=J0x\diag(2/3/e./n)*Q;
C=J0;
Dz=zeros(nx,1);
% Steady solution
Tinf=C*(A\B);
% Evolution
T=lsim(A,B,C,Dz,U,t);
% mesh(x,t,T); set(gca,'XDir','reverse')

function [J2,V,D]=j2_exp(p)
global a R e nx nt x nJ alpha J0 J1 grad div M1 T0 U

dp=[0.1/10000 p(2)/10000 p(3)/10000 p(4)/10000 1E14 1E-4];
% Construction of J2
for k=1:6
  p=p;
  p(k)=p(k)+dp(k);
  [Teff,T]=calct(p);
  J2(k,k)=2/dp(k)^2*sum(sum(abs((T0-T).^2)));
end;
for k=1:6
  for l=k+1:6
    p=p;
    p(k)=p(k)+dp(k);
    p(l)=p(l)+dp(l);
    [Teff,T]=calct(p);
    J2(k,l)=1/(dp(k)*dp(l))*sum(sum(abs((T0-T).^2)))-5*J2(k,k)*dp(k)^2-5*J2(l,l)*dp(l)^2;
  end
end;
J2=J2/nx/nt;
J2=M1*J2*M1;
[V,D]=calct(p);

```

Appendix B

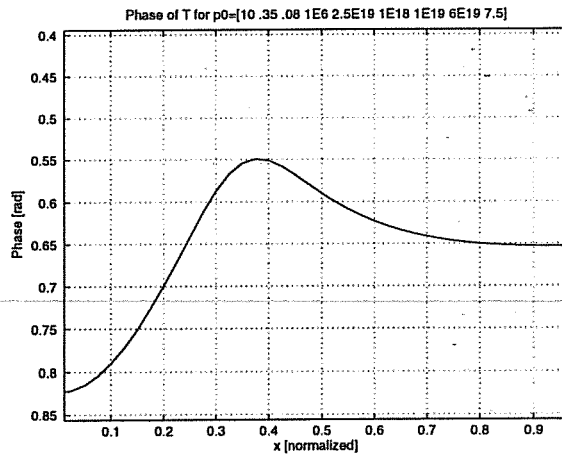
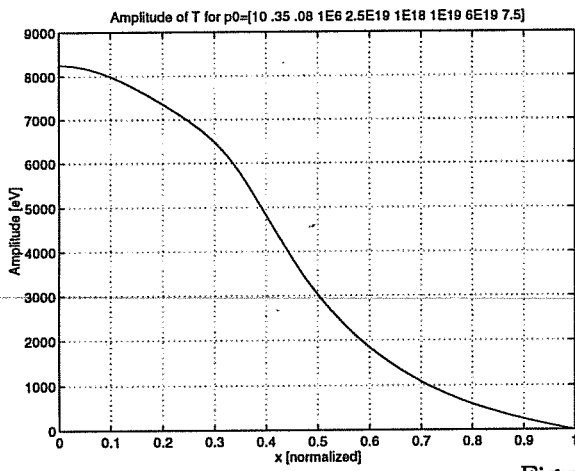


Figure B.1 a/b

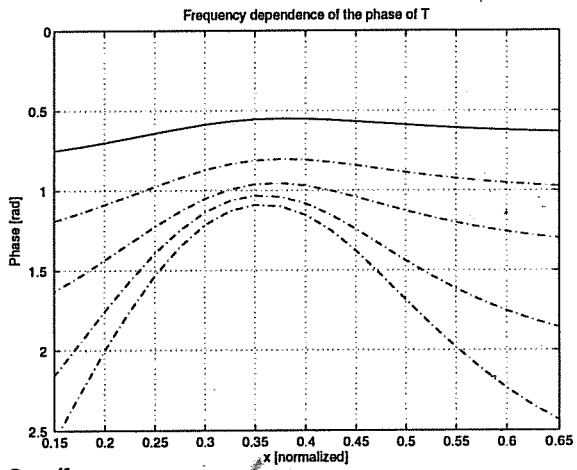
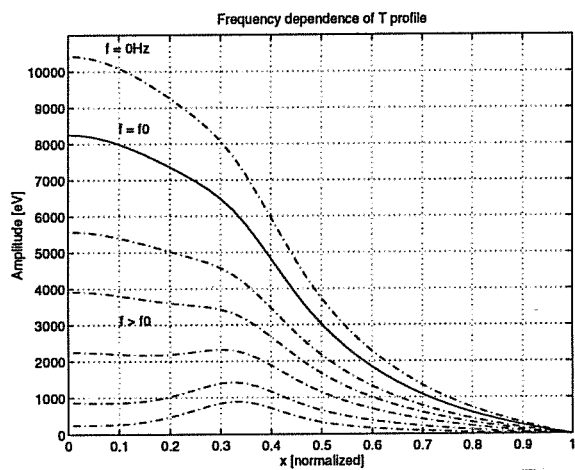


Figure B.2 a/b

equilibrium + resonance

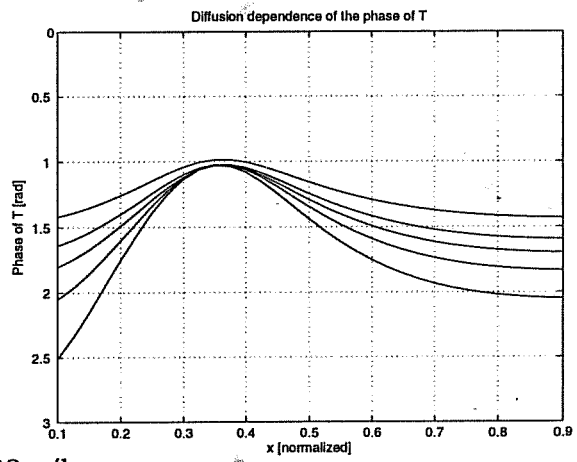
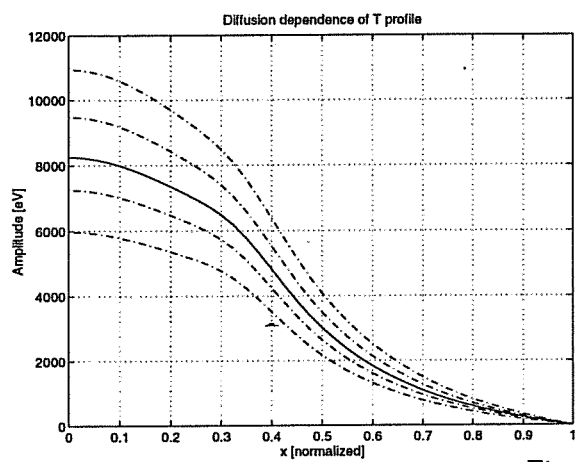


Figure B3 a/b

idem

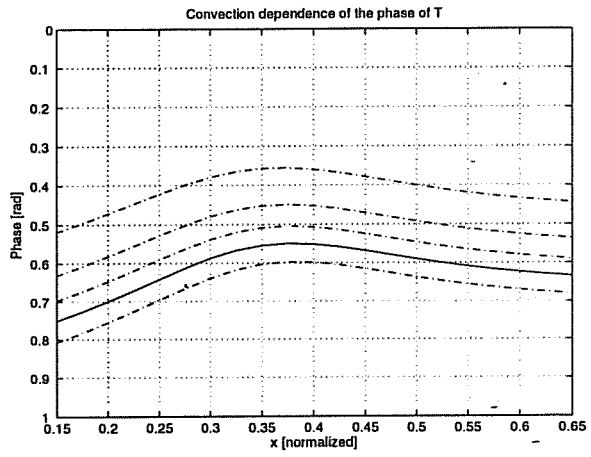
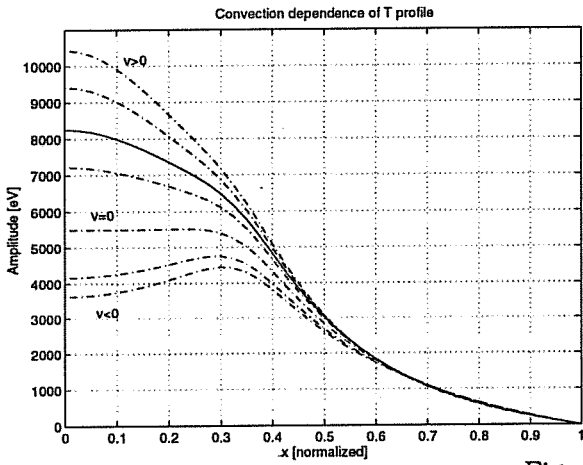


Figure B.4 a/b

Handwritten signature

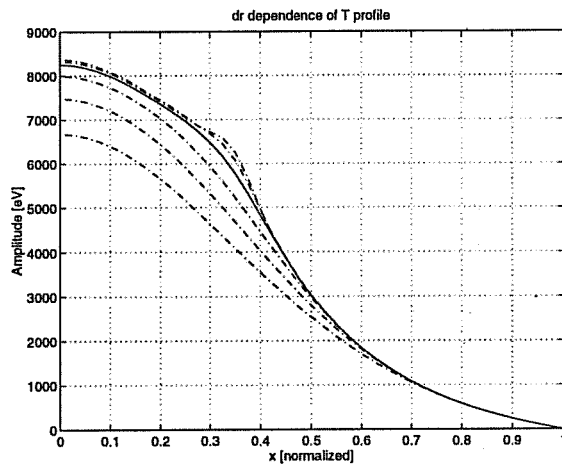
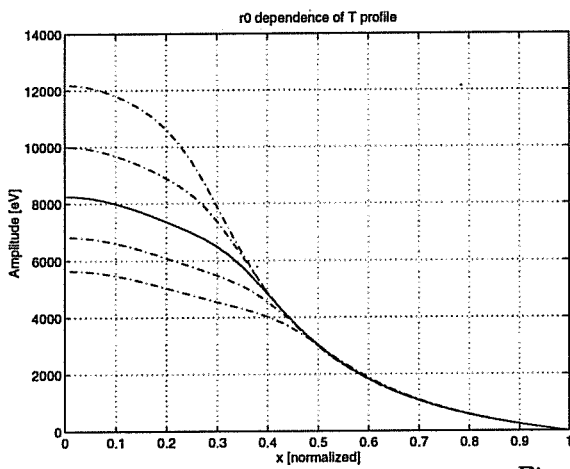


Figure B.5 a/b

Handwritten signature

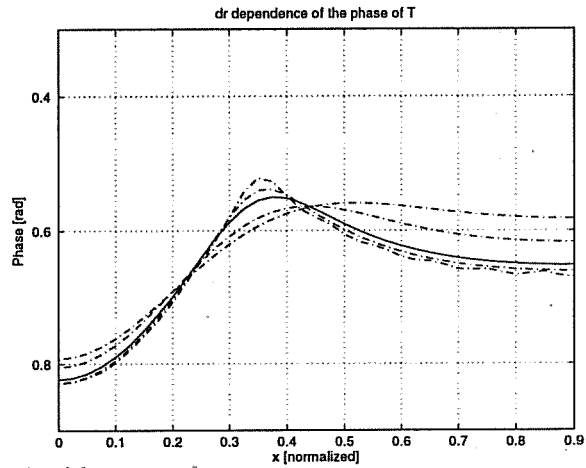
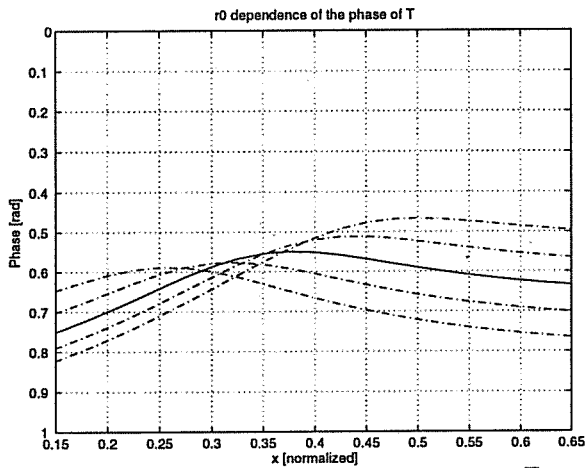


Figure B.5 c/d

Handwritten signature

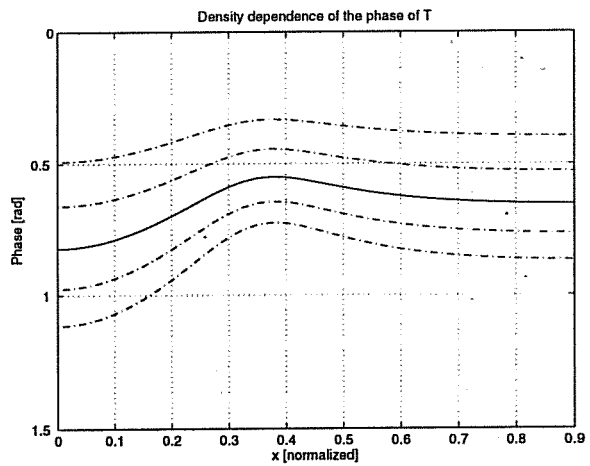
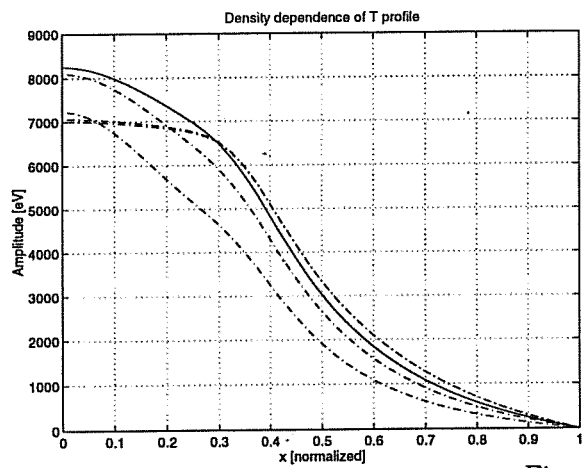


Figure B.6 a/b

Handwritten signature or mark

Appendix C

Series of plots showing temperature profile evolutions evaluated with the algorithm evolution1.m.

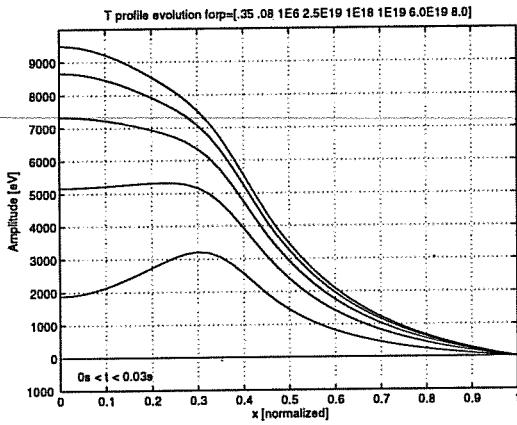


Figure C1a

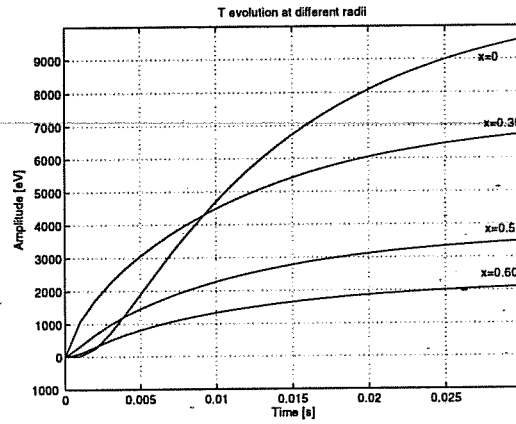


Figure C1b

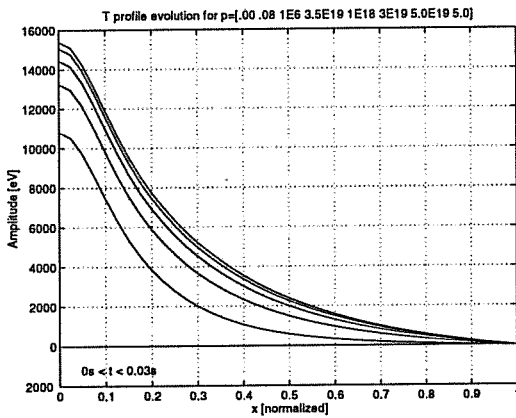


Figure C2a

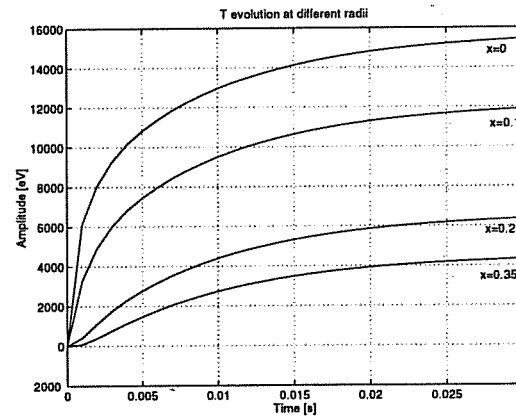


Figure C2b

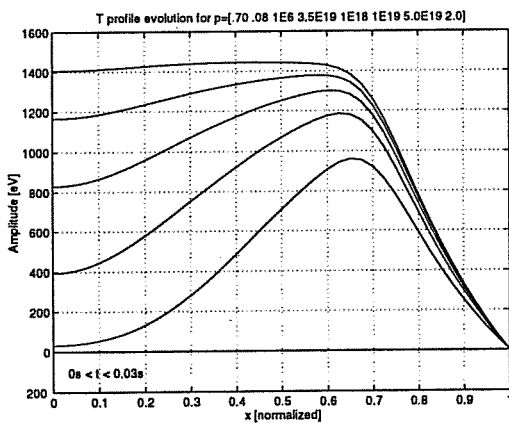


Figure C3a

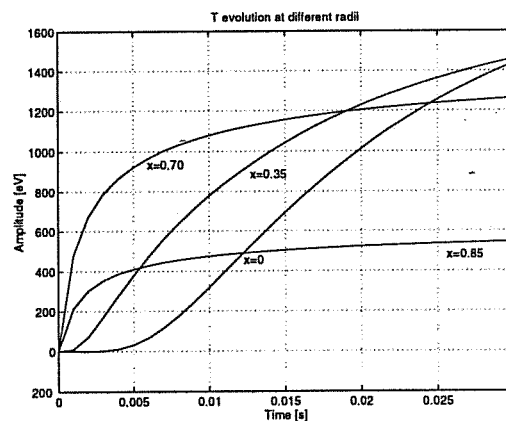


Figure C3b

Appendix D

The equation that has to be normalized is the following:

$$\frac{3}{2} \frac{\partial}{\partial t} (nT) - \frac{1}{r} \frac{\partial}{\partial r} r \left(n\chi \frac{\partial T}{\partial r} + \frac{3}{2} nvT \right) + Q \quad (\text{A.D-1})$$

Step 1: normalization of r; setting $x=r/a$, it follows

$$\frac{3}{2} \frac{\partial}{\partial t} (nT) = \frac{1}{x} \frac{\partial}{\partial x} x \left(\frac{n\chi}{a^2} \frac{\partial T}{\partial x} + \frac{3}{2} \frac{nv}{a} T \right) + Q$$

Step 2: normalization of χ ; multiplying by $\frac{a^2}{\chi_0}$, it follows

$$\frac{3}{2} \frac{a^2}{\chi_0} \frac{\partial}{\partial t} (nT) = \frac{1}{x} \frac{\partial}{\partial x} x \left(\frac{\chi}{\chi_0} n \frac{\partial T}{\partial x} + \frac{3}{2} \frac{av}{\chi_0} nT \right) + \frac{Qa^2}{\chi_0}$$

Step 3: normalization of T and n; setting $T=T/T_0$ and $n=n/n_0$ it follows

$$\frac{3}{2} \frac{a^2}{\chi_0} \frac{\partial}{\partial t} \left(\frac{n}{n_0} \frac{T}{T_0} \right) = \frac{1}{x} \frac{\partial}{\partial x} x \left(\frac{n\chi}{n_0\chi_0} \frac{1}{T_0} \frac{\partial T}{\partial x} + \frac{3}{2} \frac{av}{\chi_0} \frac{n}{n_0} \frac{T}{T_0} \right) + \frac{Qa^2}{T_0\chi_0} \quad (\text{A.D-2})$$

The J2 matrix is of the form

$$J_{2,ij} = \left[\frac{\partial^2 f}{\partial p_i \partial p_j} \right] \text{ with } p_i \in [x_0, \Delta x, P_{in}, n_0, n\chi_0, n\chi_1, v_0]$$

and it follows then

$$\begin{aligned} dt &= \frac{\chi_0}{a^2} d\bar{t} \\ dP_{in} &= \frac{\chi_0 T_0}{a^2 n_0} d\bar{P}_{in} \\ dn_0 &= n_0 d\bar{n}_0 \\ d(n\chi_0) &= n_0 \chi_0 d(\bar{n}\bar{\chi}_0) \\ d(n\chi_1) &= n_0 \chi_0 d(\bar{n}\bar{\chi}_1) \\ dv_0 &= \frac{\chi_0}{a} d\bar{v}_0 \end{aligned}$$

$J_{2, norm} = \frac{\partial^2 f}{n_0 \chi_0 \partial(\bar{p}_i \bar{p}_j)}$
 $J_{2, norm} = n_0 \chi_0 J_{2,ij}$

Appendix E

List of some calculated D and V matrices treated in section V.4.

a. Heating in the center

$$\frac{n\chi_1}{n\chi_0} = 0; \frac{av_0}{\chi_0} = 0$$

$$D = \begin{pmatrix} 7.5 \cdot 10^9 & & & \\ & 8.1 \cdot 10^6 & & \\ & & 1.8 \cdot 10^4 & \\ & & & [\sim 0] \end{pmatrix}$$

$$\frac{n\chi_1}{n\chi_0} = 5; \frac{av_0}{\chi_0} = 0$$

$$D = \begin{pmatrix} 6.4 \cdot 10^9 & & & \\ & 4.9 \cdot 10^6 & & \\ & & 7.3 \cdot 10^2 & \\ & & & [\sim 0] \end{pmatrix}$$

$$\frac{n\chi_1}{n\chi_0} = 1; \frac{av_0}{\chi_0} = 2.5$$

$$D = \begin{pmatrix} 7.7 \cdot 10^9 & & & \\ & 7.5 \cdot 10^6 & & \\ & & 1.3 \cdot 10^4 & \\ & & & [\sim 0] \end{pmatrix}$$

$$\frac{n\chi_1}{n\chi_0} = 1; \frac{av_0}{\chi_0} = -0.5$$

$$D = \begin{pmatrix} 7.1 \cdot 10^9 & & & \\ & 6.2 \cdot 10^6 & & \\ & & 5.7 \cdot 10^3 & \\ & & & [\sim 0] \end{pmatrix}$$

$$\frac{n\chi_1}{n\chi_0} = 10; \frac{av_0}{\chi_0} = -2.5$$

$$D = \begin{pmatrix} 5.5 \cdot 10^9 & & & \\ & 4.5 \cdot 10^6 & & \\ & & 1.2 \cdot 10^2 & \\ & & & [\sim 0] \end{pmatrix}$$

$$\frac{n\chi_1}{n\chi_0} = 1; \frac{av_0}{\chi_0} = 0$$

$$D = \begin{pmatrix} 7.2 \cdot 10^9 & & & \\ & 6.3 \cdot 10^6 & & \\ & & 6.5 \cdot 10^3 & \\ & & & [\sim 0] \end{pmatrix}$$

$$\frac{n\chi_1}{n\chi_0} = 10; \frac{av_0}{\chi_0} = 0$$

$$D = \begin{pmatrix} 5.7 \cdot 10^9 & & & \\ & 4.5 \cdot 10^6 & & \\ & & 1.6 \cdot 10^2 & \\ & & & [\sim 0] \end{pmatrix}$$

$$\frac{n\chi_1}{n\chi_0} = 1; \frac{av_0}{\chi_0} = 0.5$$

$$D = \begin{pmatrix} 7.3 \cdot 10^9 & & & \\ & 6.5 \cdot 10^6 & & \\ & & 7.4 \cdot 10^3 & \\ & & & [\sim 0] \end{pmatrix}$$

$$\frac{n\chi_1}{n\chi_0} = 1; \frac{av_0}{\chi_0} = -2.5$$

$$D = \begin{pmatrix} 6.8 \cdot 10^9 & & & \\ & 5.7 \cdot 10^6 & & \\ & & 3.3 \cdot 10^3 & \\ & & & [\sim 0] \end{pmatrix}$$

$$\frac{n\chi_1}{n\chi_0} = 10; \frac{av_0}{\chi_0} = +2.5$$

$$D = \begin{pmatrix} 5.9 \cdot 10^9 & & & \\ & 4.5 \cdot 10^6 & & \\ & & 2.1 \cdot 10^2 & \\ & & & [\sim 0] \end{pmatrix}$$

$$\frac{n\chi_1}{n\chi_0} = 5; \frac{av_0}{\chi_0} = -1.25$$

$$D = \begin{pmatrix} 6.3 \cdot 10^9 & & & \\ & 4.9 \cdot 10^6 & & \\ & & 6.0 \cdot 10^2 & \\ & & & [\sim 0] \end{pmatrix}$$

$$\frac{n\chi_1}{n\chi_0} = 5; \frac{av_0}{\chi_0} = -0.5$$

$$D = \begin{pmatrix} 6.3 \cdot 10^9 & & & \\ & 4.9 \cdot 10^6 & & \\ & & 6.7 \cdot 10^2 & \\ & & & [\sim 0] \end{pmatrix}$$

$$\frac{n\chi_1}{n\chi_0} = 5; \frac{av_0}{\chi_0} = +1.25$$

$$D = \begin{pmatrix} 6.5 \cdot 10^9 & & & \\ & 4.9 \cdot 10^6 & & \\ & & 9.0 \cdot 10^2 & \\ & & & [\sim 0] \end{pmatrix}$$

$$\frac{n\chi_1}{n\chi_0} = 5; \frac{av_0}{\chi_0} = +0.5$$

$$D = \begin{pmatrix} 6.4 \cdot 10^9 & & & \\ & 4.9 \cdot 10^6 & & \\ & & 7.9 \cdot 10^2 & \\ & & & [\sim 0] \end{pmatrix}$$

b. Heating half way to the edge

$$\frac{n\chi_1}{n\chi_0} = 0; \frac{av_0}{\chi_0} = 0$$

$$D = \begin{pmatrix} 1.4 \cdot 10^9 & & & \\ & 3.0 \cdot 10^7 & & \\ & & 1.9 \cdot 10^3 & \\ & & & [\sim 0] \end{pmatrix}$$

$$\frac{n\chi_1}{n\chi_0} = 5; \frac{av_0}{\chi_0} = 0$$

$$\frac{n\chi_1}{n\chi_0} = 1; \frac{av_0}{\chi_0} = 0$$

$$D = \begin{pmatrix} 1.6 \cdot 10^9 & & & \\ & 2.2 \cdot 10^7 & & \\ & & 4.1 \cdot 10^2 & \\ & & & [\sim 0] \end{pmatrix}$$

$$\frac{n\chi_1}{n\chi_0} = 10; \frac{av_0}{\chi_0} = 0$$

$$D = \begin{pmatrix} 4.3 \cdot 10^8 & & & \\ & 9.6 \cdot 10^7 & & \\ & & 29.6 & \\ & & & [\sim 0] \end{pmatrix}$$

$$D = \begin{pmatrix} 2.1 \cdot 10^8 & & & \\ & 4.9 \cdot 10^7 & & \\ & & 6.5 & \\ & & & [\sim 0] \end{pmatrix}$$

$$\frac{n\chi_1}{n\chi_0} = 1; \frac{av_0}{\chi_0} = 2.5$$

$$D = \begin{pmatrix} 1.5 \cdot 10^9 & & & \\ & 2.3 \cdot 10^7 & & \\ & & 8.2 \cdot 10^2 & \\ & & & [\sim 0] \end{pmatrix}$$

$$\frac{n\chi_1}{n\chi_0} = 1; \frac{av_0}{\chi_0} = 0.5$$

$$D = \begin{pmatrix} 1.1 \cdot 10^9 & & & \\ & 2.2 \cdot 10^7 & & \\ & & 4.7 \cdot 10^2 & \\ & & & [\sim 0] \end{pmatrix}$$

$$\frac{n\chi_1}{n\chi_0} = 1; \frac{av_0}{\chi_0} = -0.5$$

$$D = \begin{pmatrix} 9.7 \cdot 10^8 & & & \\ & 2.2 \cdot 10^7 & & \\ & & 3.6 \cdot 10^2 & \\ & & & [\sim 0] \end{pmatrix}$$

$$\frac{n\chi_1}{n\chi_0} = 1; \frac{av_0}{\chi_0} = -2.5$$

$$D = \begin{pmatrix} 7.3 \cdot 10^8 & & & \\ & 2.1 \cdot 10^7 & & \\ & & 2.3 \cdot 10^2 & \\ & & & [\sim 0] \end{pmatrix}$$

$$\frac{n\chi_1}{n\chi_0} = 10; \frac{av_0}{\chi_0} = -2.5$$

$$D = \begin{pmatrix} 1.7 \cdot 10^8 & & & \\ & 4.8 \cdot 10^6 & & \\ & & 4.9 & \\ & & & [\sim 0] \end{pmatrix}$$

$$\frac{n\chi_1}{n\chi_0} = 5; \frac{av_0}{\chi_0} = -1.25$$

$$D = \begin{pmatrix} 3.8 \cdot 10^8 & & & \\ & 9.5 \cdot 10^6 & & \\ & & 24.4 & \\ & & & [\sim 0] \end{pmatrix}$$

$$\frac{n\chi_1}{n\chi_0} = 10; \frac{av_0}{\chi_0} = 2.5$$

$$D = \begin{pmatrix} 2.6 \cdot 10^8 & & & \\ & 5.0 \cdot 10^6 & & \\ & & 8.8 & \\ & & & [\sim 0] \end{pmatrix}$$

$$\frac{n\chi_1}{n\chi_0} = 5; \frac{av_0}{\chi_0} = 0.5$$

$$D = \begin{pmatrix} 4.5 \cdot 10^8 & & & \\ & 9.7 \cdot 10^6 & & \\ & & 32.0 & \\ & & & [\sim 0] \end{pmatrix}$$

b. Heating half way to the edge

$$\frac{n\chi_1}{n\chi_0} = 0; \frac{av_0}{\chi_0} = 0$$

$$D = \begin{pmatrix} 7.2 \cdot 10^8 & & & \\ & 8.2 \cdot 10^6 & & \\ & & 5.7 \cdot 10^2 & \\ & & & [\sim 0] \end{pmatrix}$$

$$\frac{n\chi_1}{n\chi_0} = 10; \frac{av_0}{\chi_0} = 0$$

$$D = \begin{pmatrix} 1.4 \cdot 10^7 & & & \\ & 1.6 \cdot 10^5 & & \\ & & 1.3 & \\ & & & [\sim 0] \end{pmatrix}$$

$$\frac{n\chi_1}{n\chi_0} = 1; \frac{av_0}{\chi_0} = 0.5$$

$$D = \begin{pmatrix} 3.2 \cdot 10^8 & & & \\ & 3.1 \cdot 10^6 & & \\ & & 1.5 \cdot 10^2 & \\ & & & [\sim 0] \end{pmatrix}$$

$$\frac{n\chi_1}{n\chi_0} = 1; \frac{av_0}{\chi_0} = -2.5$$

$$D = \begin{pmatrix} 1.3 \cdot 10^8 & & & \\ & 2.9 \cdot 10^6 & & \\ & & 54.2 & \\ & & & [\sim 0] \end{pmatrix}$$

$$\frac{n\chi_1}{n\chi_0} = 5; \frac{av_0}{\chi_0} = 0$$

$$D = \begin{pmatrix} 4.3 \cdot 10^7 & & & \\ & 4.9 \cdot 10^5 & & \\ & & 7.5 & \\ & & & [\sim 0] \end{pmatrix}$$

$$\frac{n\chi_1}{n\chi_0} = 1; \frac{av_0}{\chi_0} = 2.5$$

$$D = \begin{pmatrix} 6.4 \cdot 10^8 & & & \\ & 3.1 \cdot 10^6 & & \\ & & 2.9 \cdot 10^2 & \\ & & & [\sim 0] \end{pmatrix}$$

$$\frac{n\chi_1}{n\chi_0} = 1; \frac{av_0}{\chi_0} = -0.5$$

$$D = \begin{pmatrix} 2.3 \cdot 10^8 & & & \\ & 3.1 \cdot 10^6 & & \\ & & 1.1 \cdot 10^2 & \\ & & & [\sim 0] \end{pmatrix}$$

$$\frac{n\chi_1}{n\chi_0} = 10; \frac{av_0}{\chi_0} = -2.5$$

$$D = \begin{pmatrix} 1.1 \cdot 10^7 & & & \\ & 1.6 \cdot 10^5 & & \\ & & 0.9 & \\ & & & [\sim 0] \end{pmatrix}$$

$$\frac{n\chi_1}{n\chi_0} = 10; \frac{av_0}{\chi_0} = 2.5$$

$$D = \begin{pmatrix} 1.9 \cdot 10^7 & & & \\ & 1.6 \cdot 10^5 & & \\ & & 1.8 & \\ & & & [\sim 0] \end{pmatrix}$$

$$\frac{n\chi_1}{n\chi_0} = 5; \frac{av_0}{\chi_0} = 0.5$$

$$D = \begin{pmatrix} 4.7 \cdot 10^7 & & & \\ & 4.9 \cdot 10^5 & & \\ & & 8.3 & \\ & & & [\sim 0] \end{pmatrix}$$

$$\frac{n\chi_1}{n\chi_0} = 5; \frac{av_0}{\chi_0} = -1.25$$

$$D = \begin{pmatrix} 3.5 \cdot 10^7 & & & \\ & 4.8 \cdot 10^5 & & \\ & & 5.9 & \\ & & & [\sim 0] \end{pmatrix}$$

Appendix F

Some temperature profile evolutions with modulated sources.

a. Regularly spaced square modulation

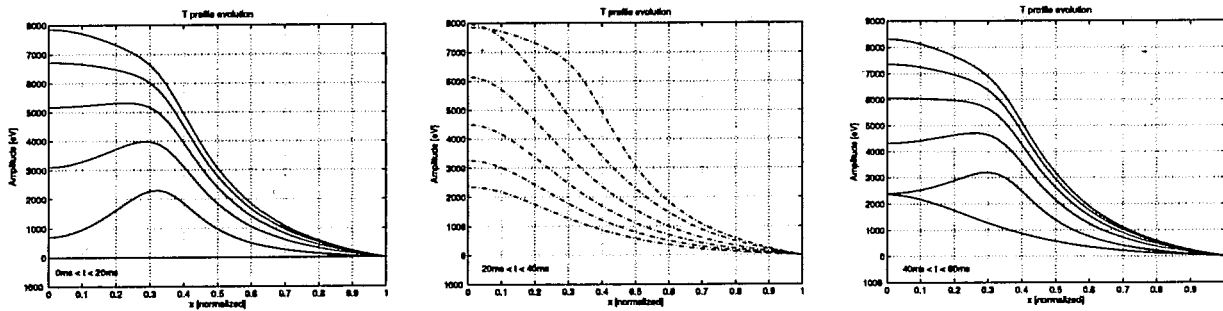


Figure A.1 a/b/c

Figure A.1 shows the profile evolution for the first 60 ms taken in p_1 .
a: profile increasing; b: profile decreasing; c: profile increasing.

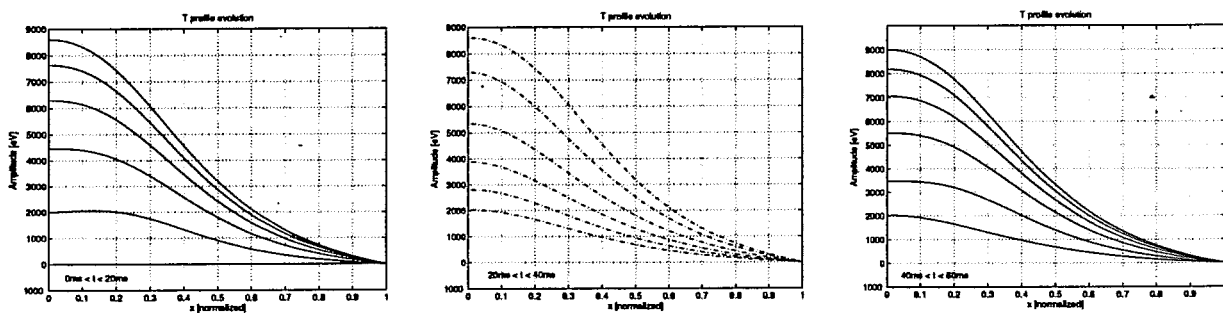


Figure A.1 a/b/c

Figure A.2 shows the profile evolution for the first 60 ms taken in p_2 .
a: profile increasing; b: profile decreasing; c: profile increasing.

b. Optimized square modulation

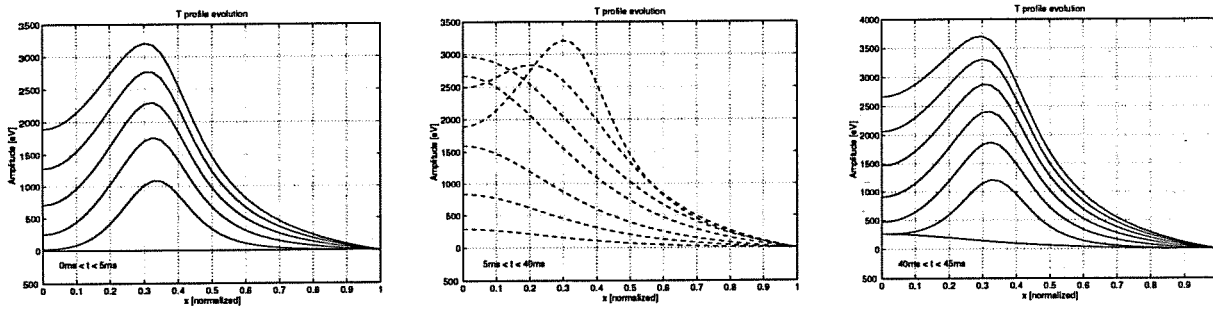


Figure A.3 a/b/c

Figure A.3 shows the profile evolution for the first 45 ms taken in p_1 .
a: profile increasing; b: profile decreasing; c: profile increasing.

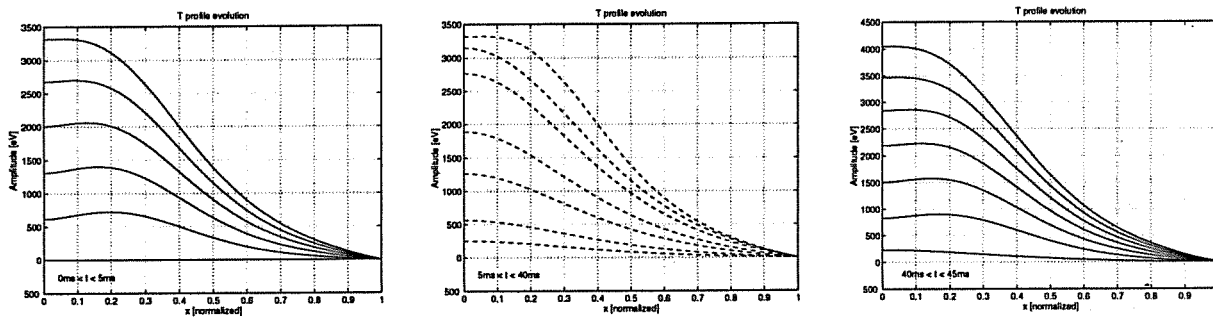
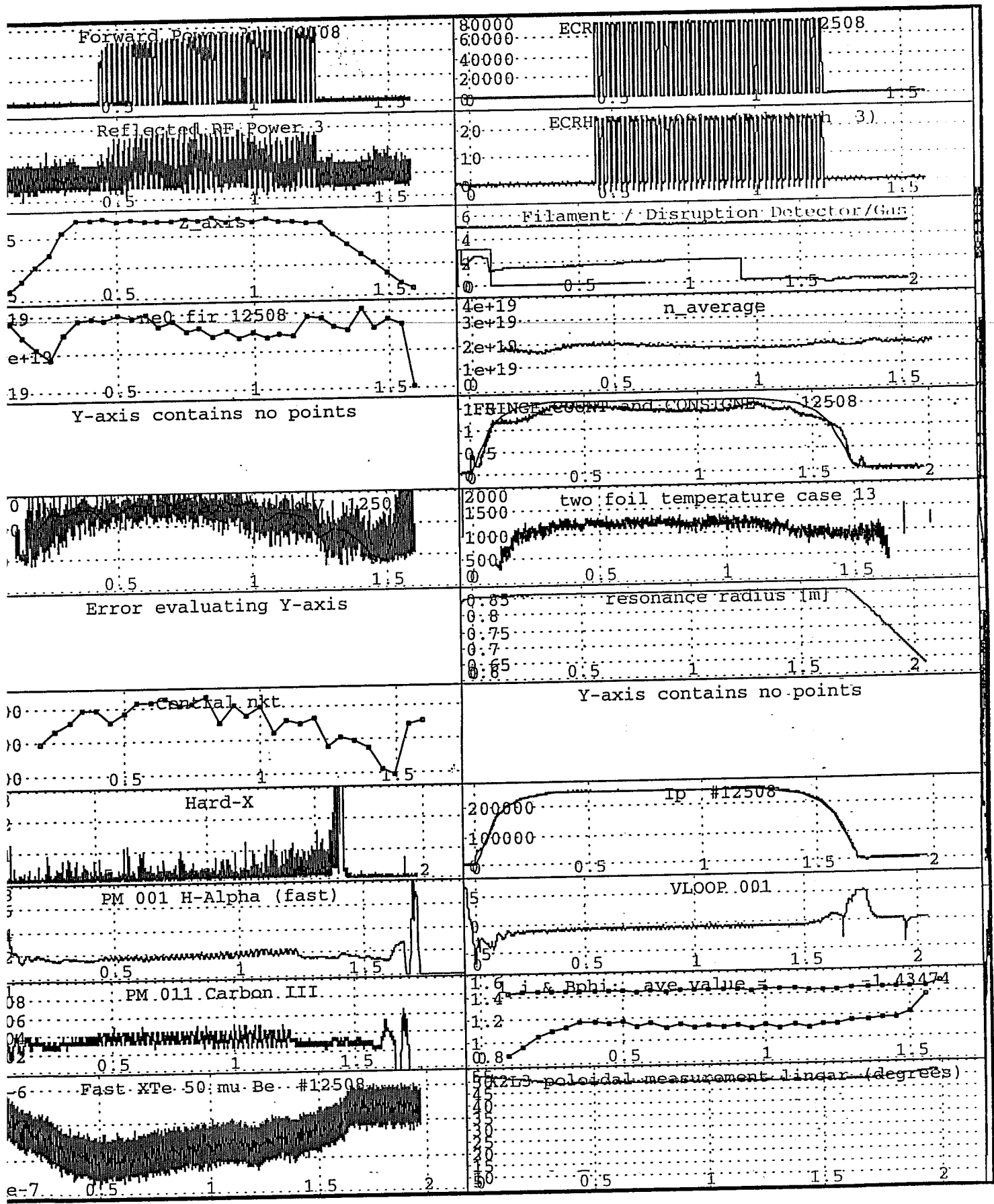


Figure A.4 a/b/c

Figure A.4 shows the profile evolution for the first 45 ms taken in p_2 .
a: profile increasing; b: profile decreasing; c: profile increasing.

Appendix G

Scope survey of shot TCV # 12508.



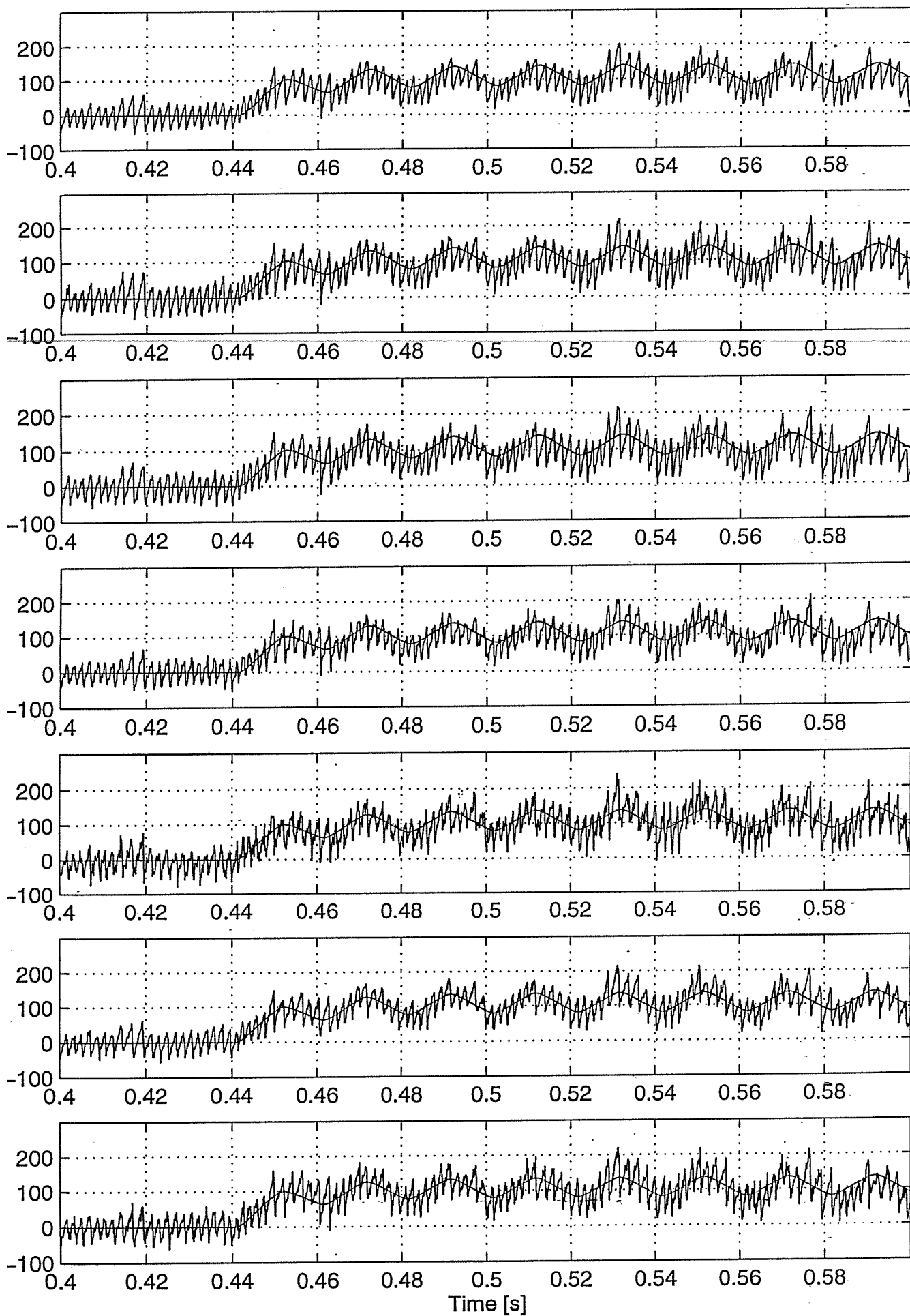
Appendix H

Experimental vs. reconstructed temperature profiles for the different x's.

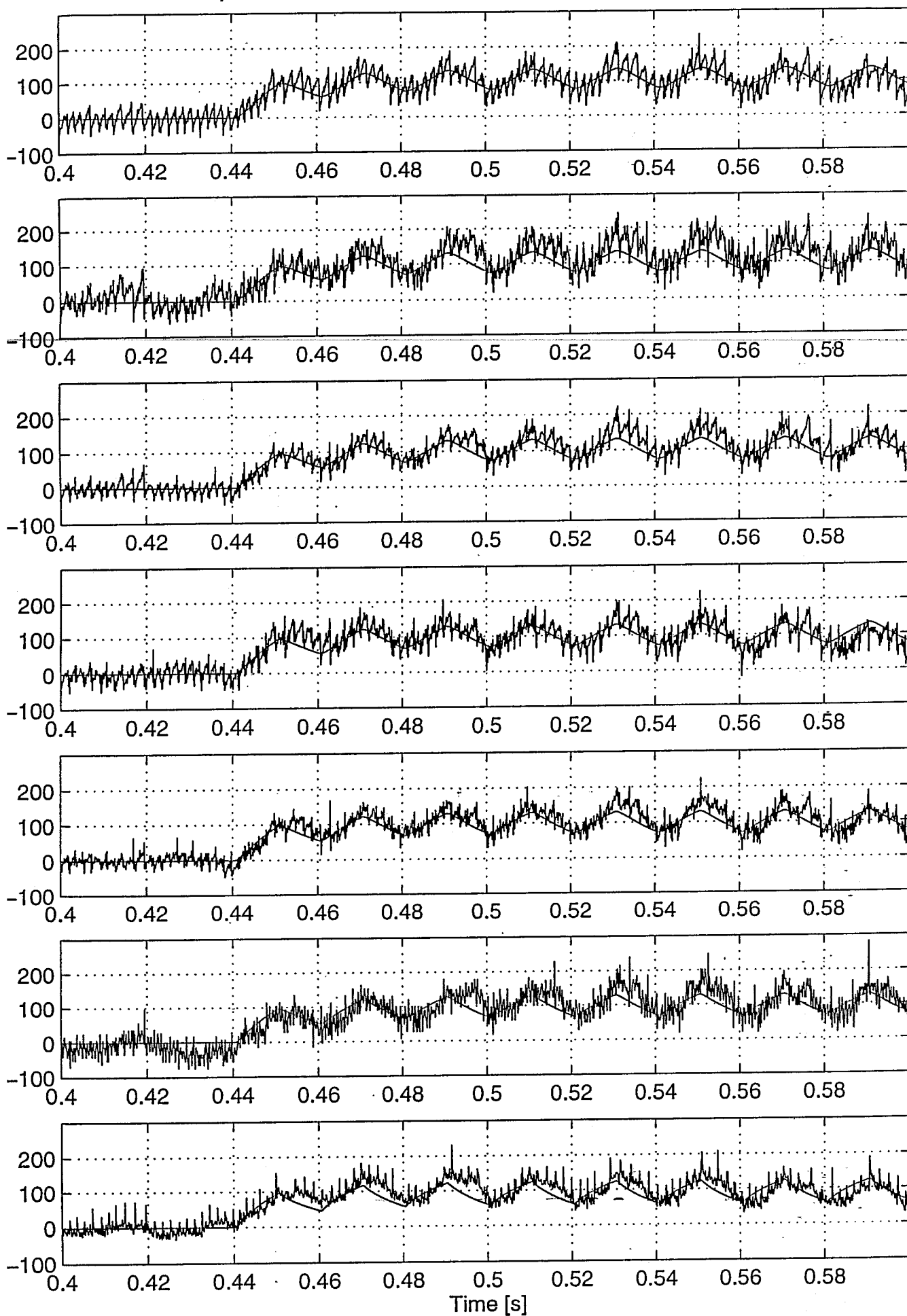
The graphs correspond to the following x-coordinates:

p. 86	p. 87	p. 88	p. 89	p. 90	p. 91
0.031	0.207	0.392	0.552	0.770	0.946
0.048	0.236	0.394	0.598	0.842	0.957
0.058	0.260	0.398	0.599	0.866	0.961
0.075	0.281	0.461	0.632	0.892	0.973
0.146	0.291	0.479	0.689	0.900	0.990
0.160	0.319	0.498	0.712	0.900	0.991
0.168	0.390	0.499	0.752	0.909	

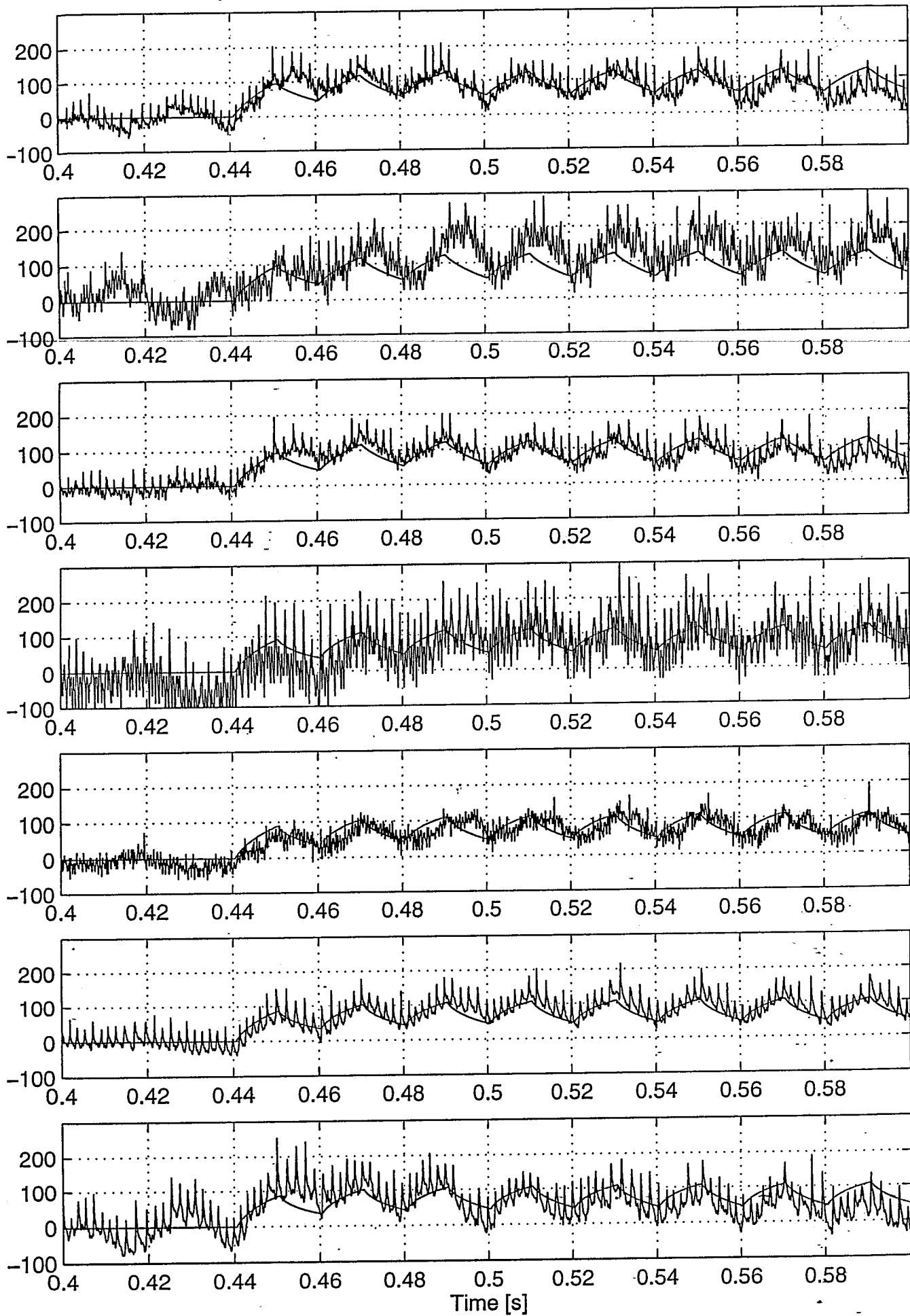
Experimental vs reconstructed T evolutions for different radii



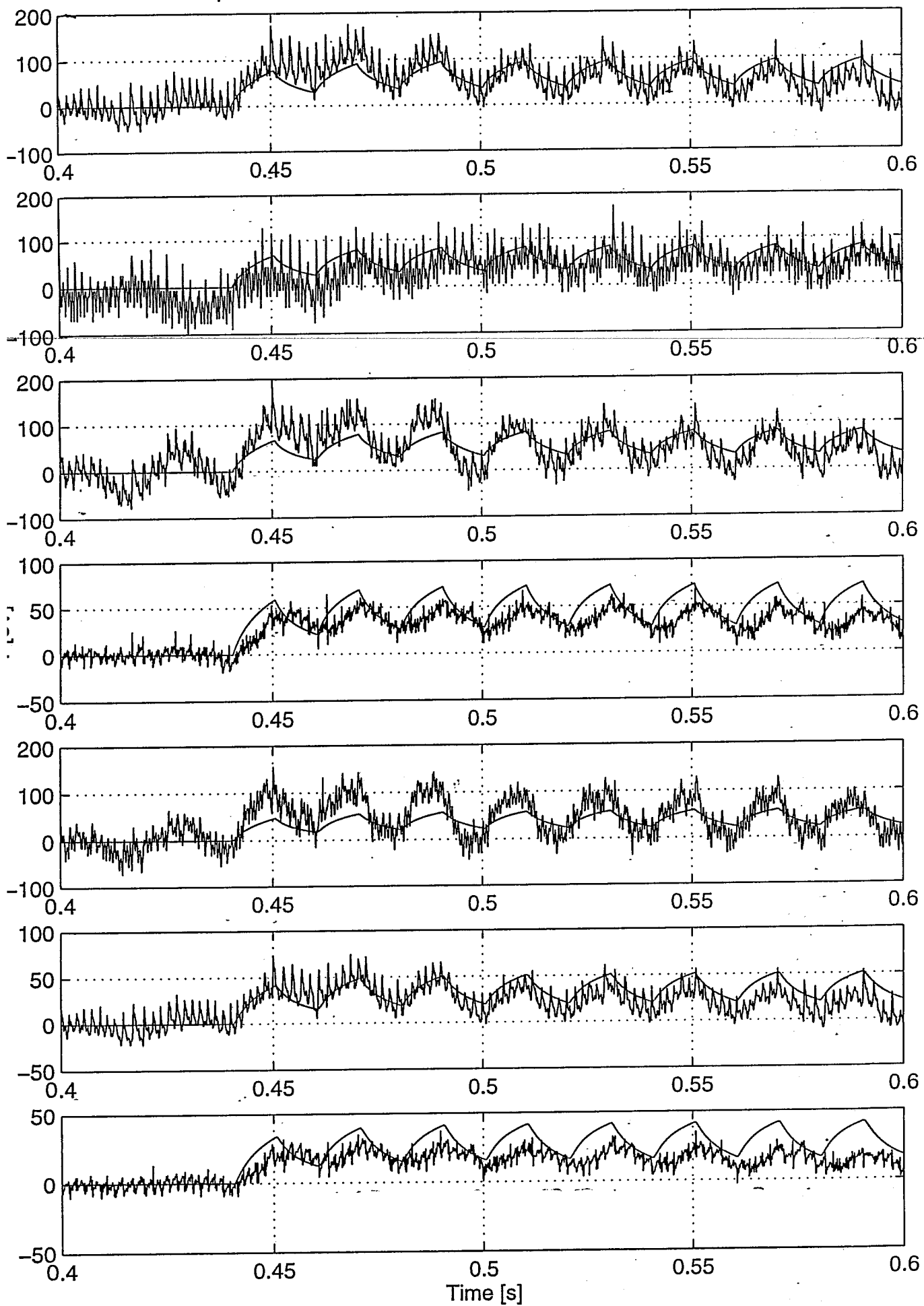
Experimental vs reconstructed T evolutions for different radii



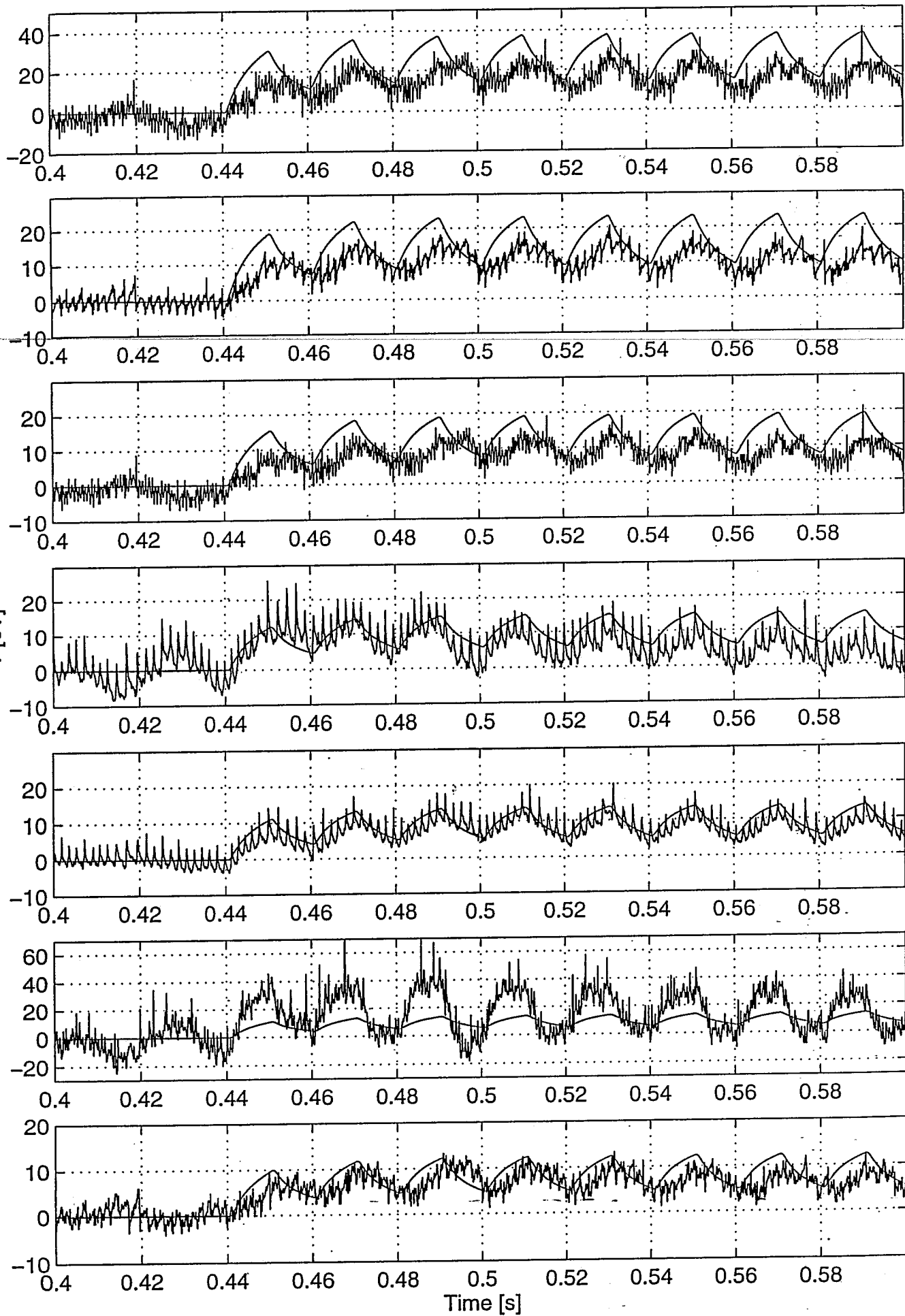
Experimental vs reconstructed T evolutions for different radii



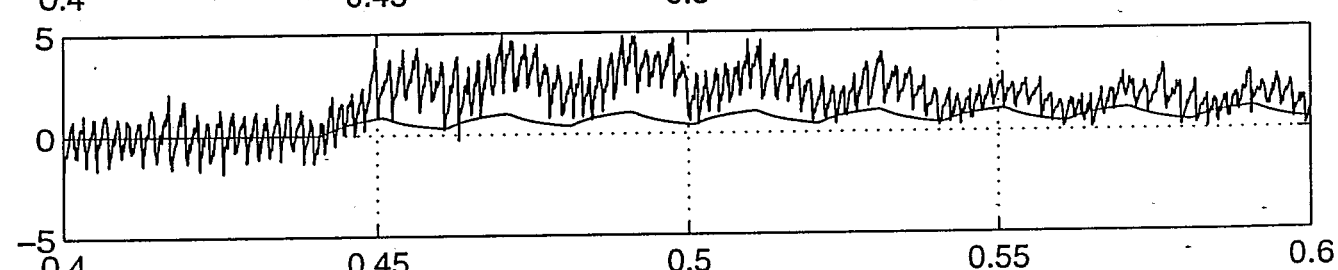
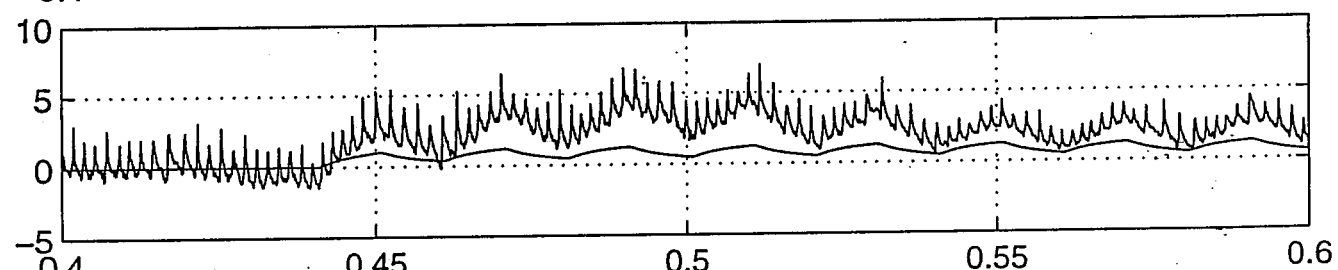
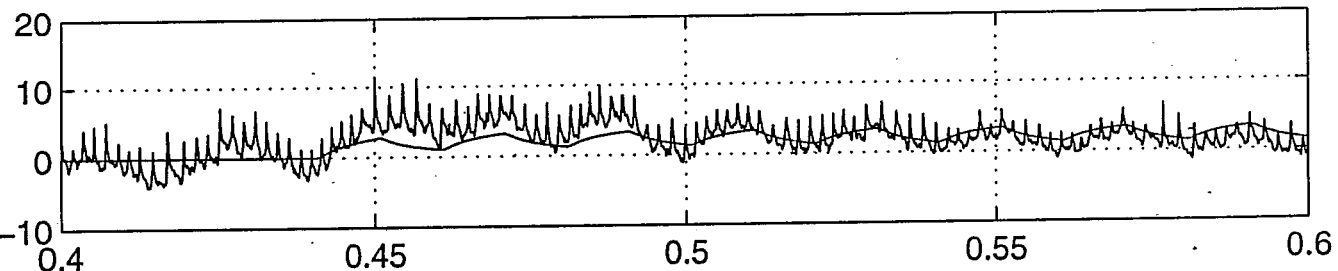
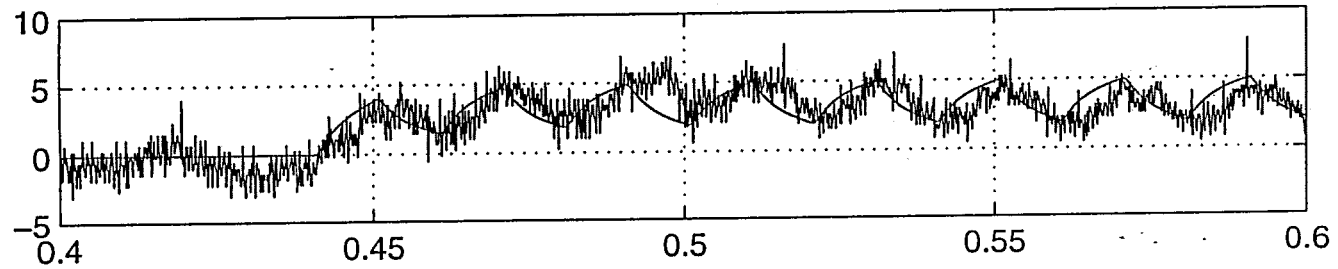
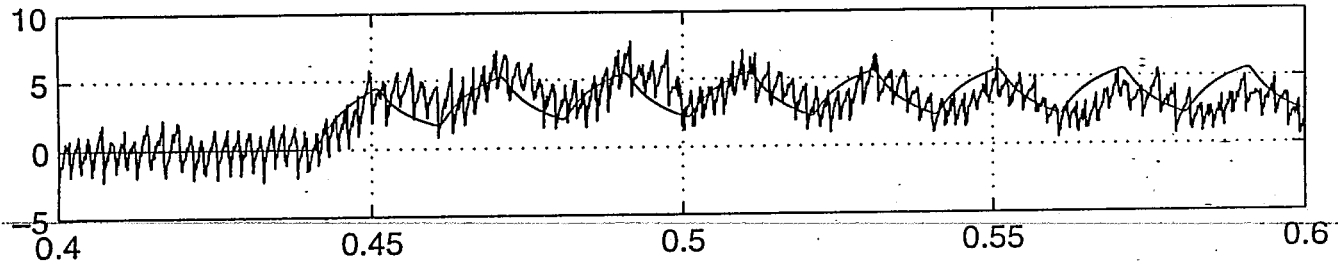
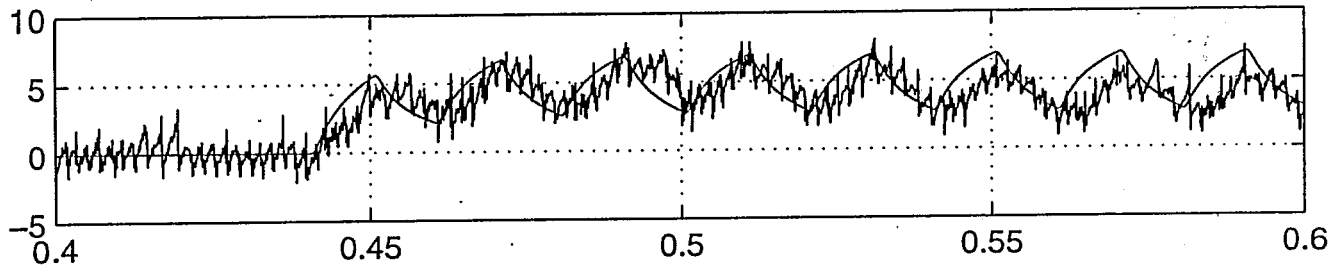
Experimental vs reconstructed T evolutions for different radii



Experimental vs reconstructed T evolutions for different radii



Experimental vs reconstructed T evolutions for different radii



Time [s]



V/réf.

N/réf. JMM/eg

Lausanne, le 1^{er} avril 1997

Travail pratique de diplôme de physicien EPFZ

Session: Mai 1997

Candidat : Adriano MANINI (EPFZ)

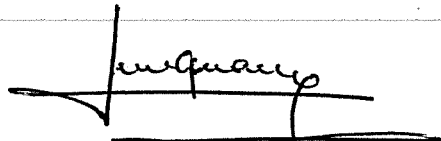
**Localisation du dépôt de puissance ECH par la réponse
dynamique du plasma de TCV**

La détermination expérimentale du profil de dépôt de puissance ECH (Electron Cyclotron Heating) constitue un ingrédient essentiel à la fois pour l'étude et la modélisation de la propagation et l'absorption des ondes cyclotrons électroniques et pour l'étude des propriétés du plasma chauffé. La réponse dynamique de paramètres du plasma tels que sa température ou son contenu en énergie thermique a déjà été utilisée dans d'autres installations. Cette approche présente l'avantage de pouvoir séparer dans une certaine mesure les mécanismes de chauffage mêmes de la réaction du plasma. Une vaste palette de formalismes ainsi que les outils numériques correspondant existent déjà, chacun avec ses points forts et ses faiblesses.

Le candidat appliquera ces diverses approches aux plasmas chauffés de TCV pour lesquelles une certaine quantité de données expérimentales a déjà été accumulée lors de la dernière campagne, en se basant essentiellement sur les instruments de mesure avec une résolution spatiale ou temporelle adéquate (émissivité des rayons X-mous, interférométrie, diamagnétisme). Le candidat attachera une importance particulière aux limites de chacune de ces méthodes afin de bien

quantifier la qualité des résultats qu'elles amènent. Dans le même esprit, il pourra proposer des scénarios d'expérience mieux adaptés pour répondre à certains points spécifiques.

Le candidat soumettra un rapport dactylographié en 5 exemplaires.



Prof. M.Q. Tran

Le travail sera suivi par le Dr. J.-M. Moret